OPTIMIZING THE SYNTHESIS OF VANADIUM OXIDE NANO-STRUCTURES BY PLASMA PLUME DYNAMICS

By

Bathusile Nelisiwe Masina

A thesis submitted in fulfilment of the academic requirements

for the PhD degree of Science in the School of Physics,

University of KwaZulu-Natal, Durban.

Supervisor:

Prof. Andrew Forbes

and

Co-Supervisor:

Dr. Bonex W. Mwakikunga

June 2016

Abstract

Thin films of monoclinic nanostructured vanadium dioxide (VO_2) (M1) are notoriously difficult to produce in a selective manner, whereas, beta-pentoxide (β-V_2O_5) and gamma-pentoxide (γ-V_2O_5) nanostructured phases are difficult to synthesize due to their demanding preparation conditions. To date, post-deposition annealing after pulsed laser deposition (PLD) has been used to revert the crystal phase of VO_2 or to remove impurities, and non-glass substrates have been employed, thus reducing the efficacy of the transparency switching between the phases. In this thesis, we overcome these limitations in PLD by optimizing a laser-ablation and deposition process through optical imaging of the laser-induced plasma. We report on high quality monoclinic rutile-type VO_2 (M1) nano-particles without requiring post-deposition annealing, and were grown on a Corning glass substrate. Our samples demonstrate a reversible metal-to-insulator (MIT) at ~43°C, without any doping, thus paving the way to switchable transparency in optical materials at room temperature. Nano-rods of β-V_2O_5 thin films were grown on Corning glass by PLD without post-deposition annealing. We demonstrate a proof of concept, that VO_2 (M1) and V_2O_5 film growth proceeds only under particular conditions and we were able to precisely control the structure as revealed by comprehensive structural and optical characterization of the film grown together with the study of plasma plume dynamics. This improved knowledge of the plume characteristic demonstrates that the conditions of growth of any complex materials can be optimized.

Masina,

Lutsala,

Mngomakati,

Jojololikati,

Mavutsela ekhatsi,

Wena logata ngemlende munye,

Wangesandla sesincele,

Mancele!

Masina!

Declaration 1

The work described by this thesis was carried out at the Council for Scientific and Industrial Research, National Laser Centre, while registered with the School of Physics, University of KwaZulu-Natal, Durban, Westville, from **Jan 2013** until **June 2016**, under the supervision of **Prof. Andrew Forbes** and co-supervisor **Dr. Bonex Mwakikunga**.

This thesis is entirely, unless specifically contradicted in the text, the work of the candidate, **Bathusile Nelisiwe Masina**, and has not been previously submitted, in whole or in part, to any other tertiary institution. Where use has been made of the work of others, it is duly acknowledged in the text.

Signed: ______________________________Name:__________________________________(Candidate)

Date: ______________________________

As the candidate's supervisor and co-supervisor respectively we have/have not approved this thesis/dissertation for submission.

Signed: ______________________________Name: ______________________________(Supervisor)

Date: ______________________________

Signed: ______________________________Name: ______________________________(Co-supervisor)

Date: ______________________________

Declaration 2 – Plagiarism

I, ____declare that

1. The research reported in this thesis, except where otherwise indicated, is my original research.

2. This thesis has not been submitted for any degree or examination at any other university.

3. This thesis does not contain other persons' data, pictures, graphs or other information, unless specifically acknowledged as being sourced from other persons.

4. This thesis does not contain other persons' writing, unless specifically acknowledged as being sourced from other researchers. Where other written sources have been quoted, then:

    a. Their words have been rewritten but the general information attributed to them has been referenced.

    b. Where their exact words have been used, then their writing has been placed in italics and inside quotation marks, and referenced.

5. This thesis does not contain text, graphics or tables copied and pasted from the internet, unless specifically acknowledged, and the source being detailed in the thesis and in the Reference sections.

Signed:_________________________________

Declaration 3 – Publications

Peer reviewed journal papers included in this thesis:

1. **BN Masina**, S Lafane, L Wu, AA Akande, B Mwakikunga, S Abdelli-Messaci, T Kerdja, A Forbes, "Phase-selective vanadiume dioxide (VO_2) nanostructured thin films by pulsed laser deposition", Journal of Applied Physics **118**, 165308 (**2015**).
2. **BN Masina**, S Lafane, L Wu, S Adbelli-Messaci, T Kedja, A Forbes, "Optimizing the synthesis of vanadium-oxygen nanostructures by plasma plume dynamics using optical imaging", Optical Engineering **54** (3), 037106 (**2015**).

Peer reviewed journal paper not included in this thesis:

1. **BN Masina**, B Mwakikunga, A Forbes, "Thermally induced damage studies with shaped light", Optical Engineering **52** (4), 044301 (**2013**).

International conference proceedings paper included in this thesis:

1. **BN Masina**, S Lafane, L Wu, S Adbelli-Messaci, T Kedja, A Forbes, "Optimisation study of the synthesis of vanadium oxide nano-structures using pulsed laser deposition", Proc. SPIE **8996**, 899615 (**2014**).

International conference proceedings paper not included in this thesis:

1. D Glaser, C Polese, R Bedekar, J Plaisier, S Pityana, **B Masina**, T Mathebula, E Troiani, "Laser shock peening on a 6056-T4 Aluminium alloy for airframe applications", Advanced Materials Research **891-892**, 974 (**2014**).

International conference presentations included in this thesis:

1. **BN Masina**, S Lafane, L Wu, S Adbelli-Messaci, T Kedja, A Forbes, "Optimisation study of the synthesis of vanadium oxide nano-structures using pulsed laser deposition", SPIE Photonics West 1-6 February **2014**, San Francisco.
2. **BN Masina**, S Lafane, L Wu, S Adbelli-Messaci, T Kedja, A Forbes, "The influence of plasma dynamics on the properties of the vanadium oxide thin films deposited by KrF laser ablation of VO_2 pellet", META conference 20-23 May **2014**, Singapore.
3. **BN Masina**, A Forbes, "Structured light for enhanced light-matter interactions", LAPAMS conference 15 – 17 January **2015**, India – **Invited talk**.

Peer reviewed journal paper included in this thesis which is in progress:

1. **BN Masina**, BW Mwakikunga, AA Akande, A Forbes, "Effect of laser wavelengths in pulsed laser deposition technique on the structural, optical properties of the V_xO_y thin films" – **In progress**.

Signed:____________________________________

Contents

Abstract i

Declaration 1 iii

Declaration 2 – Plagiarism iv

Declaration 3 – Publications v

List of Figures x

List of Tables xix

Acknowledgements xx

Chapter 1 1

Introduction 1

1.1 Objectives 2

1.2 Contents of this Thesis 2

References 4

Chapter 2 5

Vanadium Dioxide (VO_2) 5

2.1 Vanadium Oxides (V_xO_y) 5

2.2 Vanadium Dioxide (VO_2) 6

2.3 Crystal Structure 8

2.4 Energy Band Structure 9

2.5 Peierls or Mott-Hubbard Transition Mechanism 12

2.6 Other Phase of VO_2 15

2.7 Applications of VO_2 17

2.8 VO_2 Synthesis 18

2.9 VO_2 switching properties 18

2.10 Summary 20

References 20

Chapter 3 26

Pulsed Laser Induced Plasma 26

3.1 Pulsed Laser Deposition (PLD) 26

3.2 Laser Induced Plasma (LIP) 28

3.3 Laser-Target Interaction 29

3.4 Laser-Plasma Interaction 33

3.5 Plasma Plume Expansion 34

3.6 Point-blast-wave Model ... 37
3.7 Classical Drag Model ... 40
3.8 Plume-Substrate Interaction ... 40
3.9 Thin Film Growth ... 41
3.10 PLD for VO_2 Thin Films ... 42
3.11 Summary ... 44
References ... 45
Chapter 4 ... 53
Investigation of Vanadium Dioxide (VO_2) Plasma Plume Dynamics ... 53
4.1 Experimental Set-up ... 54
4.2 Results and Discussion ... 56
A. Influence of Ambient Gas on Plasma Plume Dynamics ... 56
B. Classical Drag Model ... 61
C. Point-Blast-Wave Model ... 66
4.3 Conclusions ... 68
References ... 69
Chapter 5 ... 72
Investigation of Vanadium-Oxygen Plasma Species Emission in Oxygen Ambient ... 72
5.1 Experimental Set-up ... 73
5.2 Results and Discussion ... 74
A. Influence of Ambient Gas on Plasma Plume Species Emission ... 74
B. Intensity of the Plasma Plume Species of Ablated VO_2 and V Targets ... 75
C. Spatio-Temporal Evolution of Plasma Plume Species of VO_2 and V Targets ... 83
5.3 Conclusions ... 95
References ... 95
Chapter 6 ... 98
Optimizing the Synthesis of Vanadium-Oxygen Nano-structures by Plasma Plume Dynamics ... 98
6.1 Experimental Set-up ... 99
6.2 Results and Discussion ... 99
A. Structural Properties ... 99
B. Optical Switching Properties ... 105
6.3 Conclusions ... 111
References ... 112
Chapter 7 ... 115

Phase-Selective Vanadium Dioxide (VO_2) Nano-structured Thin Films by Pulsed Laser Deposition .. 115
7.1 Experimental Set-up 116
7.2 Results and Discussion 116
A. Plume Dynamics Results 116
B. Structural Analysis 117
C. Electrical and Optical Properties 124
7.3 Conclusions 130
References 130
Chapter 8 136
Pulsed Laser Deposition of β-V_2O_5 nano-rods thin films 136
8.1 Experimental Set-up 137
8.2 Results and Discussion 138
A. Plume Dynamics Results 138
B. Structural Analysis 139
8.3 Conclusions 148
References 148
Chapter 9 152
Effect of Laser Wavelengths in PLD Technique on the Structural, Optical Properties of the VO_2 Thin Films 152
9.1 Experimental Set-up 154
9.2 Results and Discussion 155
A. Structural Analysis 155
B. Optical Switching Properties 160
9.3 Conclusions 164
References 164
Chapter 10 168
Conclusions and Future Work 168
10.1 Conclusions 168
10.2 Future Work 172
References 174

List of Figures

Figure 2.1: Vanadium oxygen (V-O) system [2.2]……………………………………………………..6

Figure 2.2: A typical case of temperature dependence of the (a) electrical resistance and (b) optical reflectance for VO_2 thin film [2.3]……………………………………………………...7

Figure 2.3: (a) VO_2 (M1) monoclinic $P2_1/c$ (insulator) below transition temperature and (b) VO_2 tetragonal rutile $P4_2/mnm$ (metal) above the transition temperature [2.5]………..7

Figure 2.4: Schematic diagram of d-electron band splitting by crystal fields and their orbitals [2.11, 2.13]……………………………………………………………………………………………..11

Figure 2.5: Schematic diagram of VO_2 energy-level [2.11, 2.13]……………………………...12

Figure 3.1: A typical schematic illustration for the PLD experimental set-up……..………………………………………………………………………………………………………..28

Figure 3.2: The schematic diagram indicates the interaction of high laser pulse energy with matter in any state of aggregation [3.13]…………………………………………………...29

Figure 3.3: Schematic diagram indicating the main laser plasma mechanisms [3.13]………34

Figure 4.1: Schematic diagram of the experimental set-up which was used to establish the VO_2 plume dynamics in this study [4.6]…………………………………………………………..57

Figure 4.2 (a): The temporal evolution of the visible spectra range of the plasma at various oxygen pressures after laser to VO_2 target interaction…………………………………59

Figure 4.2 (b): The temporal evolution of the visible spectral range of the plasma plume at various oxygen pressures after the laser-to-VO_2 target interaction (expanded time-scale)……………………………………………………………………………………………………60

Figure 4.3: Propagation of plasma plume front position for different oxygen pressure. The inserted graph shows the linear early expansion region…………………………………....62

Figure 4.4: Propagation of plasma plume front position for different oxygen pressure fitting with the classic drag model which is indicated by black line…………………………..64

Figure 4.5: Plasma plume stopping distance for different oxygen pressure as indicated in Table 4.1……………………………………………………………………………………………....65

Figure 4.6: Plasma plume initial velocity for different oxygen pressure as indicated in Table 4.1…………………………………………………………………………………………………..67

Figure 4.7: Propagation of plasma plume front position for different oxygen gas pressure fitting with the point-blast-wave which is indicating a free-expansion (black), plane-wave front (magenta), cylindrical-wave front (red) and spherical-wave front (blue)………………………………………………………………………………………………………69

Figure 5.1: Typical example of the emission intensity spectrum……………………………..77

Figure 5.2 (a): The maximum emission intensity of the species V I (of VO_2 target) as a function of the distance from the target surface for different oxygen pressure……………78

Figure 5.2 (b): The maximum emission intensity of the species V II (of VO_2 target) as a function of the distance from the target surface for different oxygen pressure……………78

Figure 5.2 (c): The maximum emission intensity of the species VO (of VO_2 target) as a function of the distance from the target surface for different oxygen pressure……………79

Figure 5.3 (a): The maximum emission intensity of the species V I (of V target) as a function of the distance from the target surface for different oxygen pressure……………82

Figure 5.3 (b): The maximum emission intensity of the species V II (of V target) as a function of the distance from the target surface for different oxygen pressure……………82

Figure 5.3 (c): The maximum emission intensity of the species VO (of V target) as a function of the distance from the target surface for different oxygen pressure……………83

Figure 5.4 (a): Propagation of V I plume species (of VO_2 target) for different oxygen gas pressures fitted with the classical drag model (red) and a free-expansion (black)………85

Figure 5.4 (b): Propagation of V II plume species (of VO_2 target) for different oxygen gas pressured fitted with the classical drag model (red) and a free-expansion (black)……………………………………………………………………………………………………86

Figure 5.4 (c): Propagation of VO plume species (of VO_2 target) for different oxygen gas pressures fitted with the classical drag model (red)……………………………………………...86

Figure 5.5 (a): Plasma plume stopping distance for different oxygen pressure (of VO_2 target)……………………………………………………………………………………………………...88

Figure 5.5 (b): Plasma plume initial velocity for different oxygen pressure (of VO_2 target)……………………………………………………………………………………………………...89

Figure 5.6 (a): Propagation of V I plume species of (of V target) for different oxygen gas pressures fitted with the classical drag model (red) and a free-expansion (black)………90

Figure 5.6 (b): Propagation of V II plume species (of V target) for different oxygen gas pressures fitted with the classical drag model (red) and a free-expansion (black)………91

Figure 5.6 (c): Propagation of VO plume species (of V target) for different oxygen gas pressures fitted with the classical drag model (red)……………………………………………...91

Figure 5.7 (a): Propagation of V I plume species (of VO_2 target) for different oxygen gas pressures fitted with the shock-wave model which is indicating plane-wave front (blue) and spherical-wave front (red)……………………………………………………………………………93

Figure 5.7 (b): Propagation of V II plume species (of VO_2 target) for different oxygen gas pressures fitted with the shock-wave model which is indicating plane-wave front (blue colour), cylindrical-wave front (pink) and spherical-wave front (red)………………..94

Figure 5.7 (c): Propagation of VO plume species (of VO_2 target) for different oxygen gas pressures fitted with the shock-wave model which is indicating plane-wave front (blue), cylindrical-wave front (pink) and spherical-wave front (red)…………………………………..94

Figure 5.8 (a): Propagation of V I plume species (of V target) for different oxygen gas pressures fitted with the shock-wave model which is indicating spherical-wave front (red)………...95

Figure 5.8 (b): Propagation of V II plume species (of V target) for different oxygen gas pressures fitted with shock-wave model which is indicating cylindrical-wave front (pink)………...96

Figure 5.8 (c): Propagation of VO plume species (of V target) for different oxygen gas pressures fitted with the shock-wave model which is indicating cylindrical-wave front (pink) and spherical-wave front (red)…………………………………………………………………96

Figure 6.1: SEM micrographs of thin films prepared at various oxygen pressures for target-substrate distance of 40 mm. Scale for all the micrographs is 2 μm………………..102

Figure 6.2: AFM images of thin films prepared at various oxygen pressures for target-substrate distance of 40 mm……………………………………………………………………...102

Figure 6.3: XRD spectra of thin films prepared at various oxygen pressures for target-substrate distance of 40 mm……………………………………………………………………...103

Figure 6.4: SEM micrographs of thin films prepared under 0.05 mbar oxygen pressure for target-substrate distance of 40 and 50 mm. Scale for all the micrographs is 2 μm……………………………………………………………………………………………………...108

Figure 6.5: AFM images of thin films prepared under 0.05 mbar oxygen pressure for target-substrate distance of 40 and 50 mm………………………………………………………...108

Figure 6.6: XRD spectra of thin films prepared under 0.05 mbar oxygen pressure for target-substrate distance of 40 and 50 mm………………………………………………………...109

Figure 6.7: Change of transmittance at different wavelengths for 26.5 °C and 70.3 °C for a thin film prepared at 0.05 mbar for target-substrate distances of 40 and 50 mm……111

Figure 6.8: Change of transmittance under temperatures at 2.5 μm for a thin film prepared at 0.05 mbar for target-substrate distances of 40 and 50 mm……………………112

Figure 7.1: Propagation of plasma plume front position for different oxygen gas pressure fitted with the point-blast-wave which is indicating a free-expansion (black), plane-wave front (magenta), cylindrical-wave front (red) and spherical-wave front (blue) propagation……………………………………………………………………………………………119

Figure 7.2: XRD spectra of VO_2 (M1) thin films deposited under low oxygen gas pressure (0.05 and 0.01 mbar) and target-substrate distance for 30 and 36 mm and substrate temperature of 500 °C……………………………………………………………………...120

Figure 7.3: SEM micrographs of VO_2 (M1) thin films deposited under low oxygen gas pressure (0.05 and 0.01 mbar) and target-substrate distance for 30 and 36 mm and substrate temperature of 500 °C……………………………………………………………………..122

Figure 7.4: AFM images of VO_2 (M1) thin films deposited under low oxygen gas pressure (0.05 and 0.01 mbar) and target-substrate distance for 30 mm and 36 mm and substrate temperature of 500 °C……………………………………………………………………..122

Figure 7.5: XRD spectra of V_xO_y thin films deposited under low oxygen gas pressure (0.05 and 0.01 mbar) and target-substrate distance for 35 mm and 38 mm and substrate temperature of 500 °C……………………………………………………………………………………123

Figure 7.6: SEM micrographs of V_xO_y thin films deposited under low oxygen gas pressure (0.05 and 0.01 mbar) and target-substrate distance for 35 mm and 38 mm and substrate temperature of 500 °C……………………………………………………………………..124

Figure 7.7: AFM images of V_xO_y thin films deposited under low oxygen gas pressure (0.05 and 0.01 mbar) and target-substrate distance for 35 mm and 38 mm and substrate temperature of 500 °C……………………………………………………………………………………125

Figure 7.8: Change of the resistance and transmittance of a thin film under temperature cycling prepared at 0.01 mbar oxygen pressure for target-substrate distance of 36 mm………..127

Figure 7.9: Change of the resistance and transmittance of a thin film under temperature cycling prepared at 0.01 mbar oxygen pressure for target-substrate distance of 38 mm………..127

Figure 7.10: Change of the resistance and transmittance of a thin film under temperature cycling prepared at 0.05 mbar oxygen pressure for target-substrate distance of 30 mm……………………………………………………………………………………….127

Figure 8.1: Propagation of plasma plume front position for different oxygen gas pressure fitted with the point-blast-wave which is indicating a free-expansion (black), plane-wave front (magenta) and spherical-wave front (blue) propagation……………….141

Figure 8.2: XRD spectra of V_xO_y thin films deposited under high oxygen gas pressure (0.2 and 0.1 mbar) and target-substrate distance for 23 and 27 mm. These parameters were determined from points A and B in the plasma propagation graph as given in Figure 8.1………………………………………………………………………………………………………142

Figure 8.3: Raman spectra of V_2O_5 thin films deposited under 0.2 and 0.1 mbar oxygen pressure and target-substrate distance for 23 and 37 mm. These parameters were determined from points A and B in the plasma propagation graph as given in Figure 8.1……143

Figure 8.4: SEM micrographs of V_xO_y thin films deposited under high oxygen gas pressure (0.2 and 0.1 mbar) and target-substrate distance for 23 and 27 mm. These parameters were determined from points A and B in the plasma propagation graph as shown in Figure 8.1……………………………………………………………………………………...143

Figure 8.5: AFM images of V_xO_y thin films deposited under high oxygen gas pressure (0.2 and 0.1 mbar) and target-substrate distance for 23 and 27 mm. These parameters were determined from points A and B in the plasma propagation graph as given in Figure 8.1………………………………………………………………………………………………………144

Figure 8.6: XRD spectra of V_2O_5 thin films deposited under 0.2 and 0.1 mbar oxygen pressure and target-substrate distance for 29 and 34 mm. These parameters were determined from points C and D in the plasma propagation graph as given in Figure 8.1........145

Figure 8.7: Raman spectra of V_2O_5 thin films deposited under 0.2 and 0.1 mbar oxygen pressure and target-substrate distance for 29 and 34 mm. These parameters were determined from points C and D in the plasma propagation graph as given in Figure 8.1........146

Figure 8.8: SEM micrographs of V_2O_5 thin films deposited under 0.2 and 0.1 mbar oxygen pressure and target-substrate distance for 29 and 34 mm. These parameters were determined from points C and D in the plasma propagation graph as given in Figure 8.1........146

Figure 8.9: AFM images of V_2O_5 thin films deposited under 0.2 and 0.1 mbar oxygen pressure and target-substrate distance for 29 and 34 mm. These parameters were determined from points C and D in the plasma propagation graph as given in Figure 8.1........147

Figure 8.10: XRD spectra of V_2O_5 thin films deposited under 0.2 mbar oxygen pressure and target-substrate distance for 23, 29 and 37 mm........149

Figure 8.11: AFM images of V_2O_5 thin films deposited under 0.2 mbar oxygen pressure and target-substrate distance for 23, 29 and 37 mm........149

Figure 9.1: XRD spectra of VO_2 (M1) thin films deposited using several laser wavelengths (1064, 532, 355 and 266 nm) under 0.05 mbar oxygen pressure and target-substrate distance for 49 mm on 450 °C Corning glass........157

Figure 9.2: SEM micrographs of VO_2 (M1) thin films deposited using several laser wavelengths (1064, 532, 355 and 266 nm) under 0.05 mbar oxygen pressure and target-substrate distance for 49 mm on 450 °C Corning glass…………………………………..160

Figure 9.3: AFM images of VO_2 (M1) thin films deposited using several laser wavelengths (1064, 532, 355 and 266 nm) under 0.05 mbar oxygen pressure and target-substrate distance for 49 mm on 450 °C Corning glass…………………………………..161

Figure 9.4: Change of the transmittance of a thin film under temperature cycling prepared at 266 nm laser wavelength under 0.05 mbar oxygen pressure and target-substrate distance for 49 mm on 450 °C Corning glass…………………………………………..162

Figure 9.5: Change of the transmittance of a thin film under temperature cycling prepared at 355 nm laser wavelength under 0.05 mbar oxygen pressure and target-substrate distance for 49 mm on 450 °C Corning glass…………………………………………..163

Figure 9.6: Change of the transmittance of a thin film under temperature cycling prepared at 532 nm laser wavelength under 0.05 mbar oxygen pressure and target-substrate distance for 49 mm on 450 °C Corning glass…………………………………………..163

Figure 9.7: Change of the resistance and transmittance of a thin film under temperature cycling prepared at 1064 nm laser wavelength under 0.05 mbar oxygen pressure and target-substrate distance for 49 mm on 450 °C Corning glass…………………………………..164

List of Tables

Table 2.1: This table indicates atomic position of V and O atoms……………………………..9

Table 2.2: This table indicates lattice parameters for VO_2 (M1) and (R), respectively…9

Table 2.3: Density of VO_2 polymorphs [2.27]……………………………………………………....16

Table 2.4: Size effects [2.43]……………………………………………………………………………20

Table 4.1: Drag model parameter values for the plasma plume at different oxygen pressures……………………………………………………………………………………………………....65

Table 5.1: Optical emission lines with corresponding electron transitions in V atoms (V I), singly charged V^+ ions (V II) and VO…………………………………………………………....76

Table 5.2: Analysis of the species ratio of VO_2 target……………………………………………80

Table 5.3: Analysis of the species ratio of V target…………………………………………………..84

Table 5.4: Drag model parameter values for the plasma plume of VO_2 target at different oxygen pressures……………………………………………………………………………………………...87

Table 5.5: Drag model parameter values for the plume species of V target at different oxygen pressures……………………………………………………………………………………………...92

Table 7.1: Electrical and optical switching properties parameter…………………………128

Table 9.1: Switching and structural parameters…………………………………………………..164

Acknowledgements

First and foremost, praise and thanks go to the Almighty God, for His Love and Blessings all the time.

I am extremely thankful to the following people:

- Prof. A. Forbes and Dr. B.W. Mwakikunga for supervising this work.
- My collaborator, Mr S. Lafane for the warm welcome at the CDTA in Algeria for his guidance and allowing me to use his laboratory.
- Dr. L. Wu for her guidance.
- Mr A. Akande for his help with the analysis.
- Mr A. Sharma and Dr. T. Roberts for their technical aspects of this work.
- Dr. M. Tlotleng, Dr. J. Wesley-Smith and Mr N. Arthur for proofreading the thesis.

I would like to extend my deep appreciation to CSIR-NLC for granting me the opportunity to work in such a conducive environment, in particular the User Facility.

My studies were funded by National Research Foundation (NRF) Thuthuka and NRF South Africa-Algeria bilateral joint call.

To the staff at CSIR-NLC (especially Ms T. Mhlanga, Dr. S. Ngcobo and Ms M. Budzwa) who made it possible for me to feel at home.

To my friend, Ms V. Nekhwalivha for her support, encouragement and believing that I could achieve this.

To my family, Ms N. Lukhele and Mr N. Sokhulu, thank you for being patient with me and understanding at all the times.

Chapter 1

Introduction

Vanadium oxide (V_xO_y) materials have been produced and reported because of their several structural and compositional variants, as well as their use in a number of applications, for example gas-sensors device, actuators and e.t.c.[1.1]. One of the most popular V_xO_y that have been produced and reported is vanadium dioxide (VO_2) because it has interesting thermochromic properties as a consequence of its reversible structural information and associated metal-to-insulator transition (MIT) transformation near 68 °C [1.2] in the bulk crystal. VO_2 has been investigated in recent years for their scientific and technological applications ranging from femtosecond optical switching to thermal management coatings [1.3]. However, VO_2 is not immediately applicable to several technological applications, because VO_2 is difficult to produce due to the narrow temperature-pressure window in phase space, as a result of the multiple valence states of vanadium [1.1] and several non-hydrate polymorphs of VO_2 [1.4]. Hence, the challenges involved in VO_2 synthesis should be investigated. Furthermore, one needs to investigate how to modify the phase transition to suit specific technological applications. Another ongoing controversy of VO_2 is the driving mechanism of the transition. The issue is whether the given phase transition is an electron Mott transition [1.5] accompanied with structural changes or a Peierls-type transition [1.6] in which structural changes dominate, and the rearrangement of the electron subsystem is an auxiliary process, which remains unanswered.

1.1 Objectives

In this thesis, the challenges involved in VO_2 synthesis are addressed by synthesizing V_xO_y nano-particles using the pulsed laser deposition (PLD) method, which allows the particle size, composition and properties of the nano-materials to be controlled. This is achieved by investigating the plasma plume dynamics and plasma plume emissions of vanadium oxygen (V-O) species during the PLD process. This was done because the source of the thin film is the laser generated plasma plume composes of neutral and ionised atoms and molecules.

1.2 Contents of this Thesis

The outline of this thesis is described as follows:

- Chapter 2 discusses the properties of VO_2 and its oxidation states, including the phase transition mechanisms and VO_2 thin film synthesis.
- Chapter 3 discusses in detail the importance of laser induced plasma in PLD, V_xO_y nano-particles and growth.
- Chapter 4 investigates the plasma formation and expansion mechanisms during the PLD process of V_xO_y films deposition by the laser ablated VO_2 target. The experimental findings reveal several interesting features which are of general character and interest, with the temporal dynamics found to be dependent on the oxygen pressure. The classical drag and shock-wave models were used to understand the plasma plume expansion and plume species propagation.
- Chapter 5 investigates the plume species expansion and propagation during the PLD process of V_xO_y film deposition by vaporized VO_2 and V targets. The

stopping distance, initial velocity, slowing coefficient and the shock conditions were determined using classical drag and point-blast-wave models.

- Chapter 6 investigates the relationship between the plasma plume dynamics and deposited V_xO_y compound thin films which were deposited at the same conditions of the oxygen pressure and laser fluencies used for the plasma plume and plume species study in Chapters 4 and 5, respectively. The thin films were deposited on Corning glass by ablating the VO_2 target. This chapter showed a proof of concept that VO_2 (M1) film grows only under particular conditions. The conditions were precisely controlled as revealed by comprehensive structural and optical characterisation of the film grown, and through the study of plume dynamics, which behave as in other studies of other materials.
- Chapter 7 shows that it is possible to improve the VO_2 composition by understanding the link between the V-O plume and the VO_2 stoichiometry in a PLD process without the need of post-deposition annealing. This chapter reports high quality VO_2 (M1) nano-particle by optimizing the deposition parameters, without post-annealing, and on a Corning glass substrate. This sample demonstrates a reversible MIT at ~43 °C, without any doping, paving the way to switchable transparency in optical materials at room temperature.
- Chapter 8 shows that it is possible to synthesize and improve the β-V_2O_5 composition by understanding the link between the V-O plume and the V_2O_5 stoichiometry in PLD without the need of post-annealing. This chapter reports high quality β-V_2O_5 nano-rods by optimizing the deposition parameters, without post-deposition annealing, and on a Corning glass substrate.
- Chapter 9 reports the influence of the laser wavelengths in the PLD technique on the structural and optical properties of the optimized VO_2 thin films. By varying

laser wavelength, a-axis oriented VO_2 (M1) thin film is obtained on a Corning glass substrate without post-deposition annealing and doping.

- Chapter 10 presents conclusion and future work.

References

1.1 U. Schwingenschlögl, V. Eyert, "The vanadium Magnéli phases V_nO_{2n-1}", Ann. Phys. (Leipzig) **13** (9), 475 (**2004**).

1.2 F.J. Morin, "Oxides which show a metal-to-insulation at the Neel temperature" Phys. Rev. Lett. **3** (1), 34 (**1959**).

1.3 H. Jerominek, F. Picard, D. Vincent, "Vanadium oxide films for optical switching and detection", Opt. Eng. **32**, 2092 (**1993**).

1.4 S.R. Popuri, A. Artemenko, C. Labrugere, M. Miclau, A. Villesuzanne, M Polleti, "VO_2 (A): Reinvestigation of crystal structure, phase transition and crystal growth mechanisms", J. Solid State Chem. **213**, 79 (**2014**).

1.5 R.M. Wentzcovitch, W.W. Schulz, P.B. Allen, "VO_2: Peierls or Mott-Hubbard? A view from band theory", Physical Rev. Lett. **72** (21), 3389 (**1994**).

1.6 D. Paquet, P. Leroux-Hugon, "Electron correlations and electron-lattice interactions in the metal-insulator, ferroelastic transition in VO_2: A thermodynamixal study" Physical Rev. B **22** (11), 5284 (**1980**).

Chapter 2

Vanadium Dioxide (VO_2)

This chapter introduces vanadium oxides (V_xO_y's) and their oxidation states with vanadium dioxide (VO_2) being of primary focus. We therefore discuss VO_2 and its phase transition, including the phase transition mechanisms. We also review the synthesis of VO_2 thin films and nano-particles.

2.1 Vanadium Oxides (V_xO_y)

Vanadium exhibits several oxidation states [2.1], normally from V^{2+} - V^{5+}, and reacts with oxygen to form vanadium monoxide (VO), VO_2, vanadium trioxide (V_2O_3) and vanadium pentoxide (V_2O_5). There are also assorted valence oxides containing two oxidation states found in the vanadium-oxygen (V-O) phase diagram as shown in Figure 2.1 [2.2]. The two oxidation states are V_6O_{13} accompanied by V^{5+} and V^{4+}; and there is a sequence of oxides between VO_2 and V_2O_3 (for instance V_8O_{15}, V_2O_{13}, V_6O_{11}, etc.) which have V^{4+} and V^{3+} oxidation states. Introducing oxygen vacancy defects to vanadium oxide results in the formation of the assorted valence oxides. Normally, the vacancies move to correlate and establish crystallographic shear planes and afterward are removed by restructuration of V-O coordination units, provided the oxygen number of vacancies is greater than a certain value. This leads in a sequence of associated stoichiometric oxides such as V_nO_{2n-1} and $V_{2n}O_{5n-2}$ which are known to be Magneli and Wadsley phases respectively [2.1].

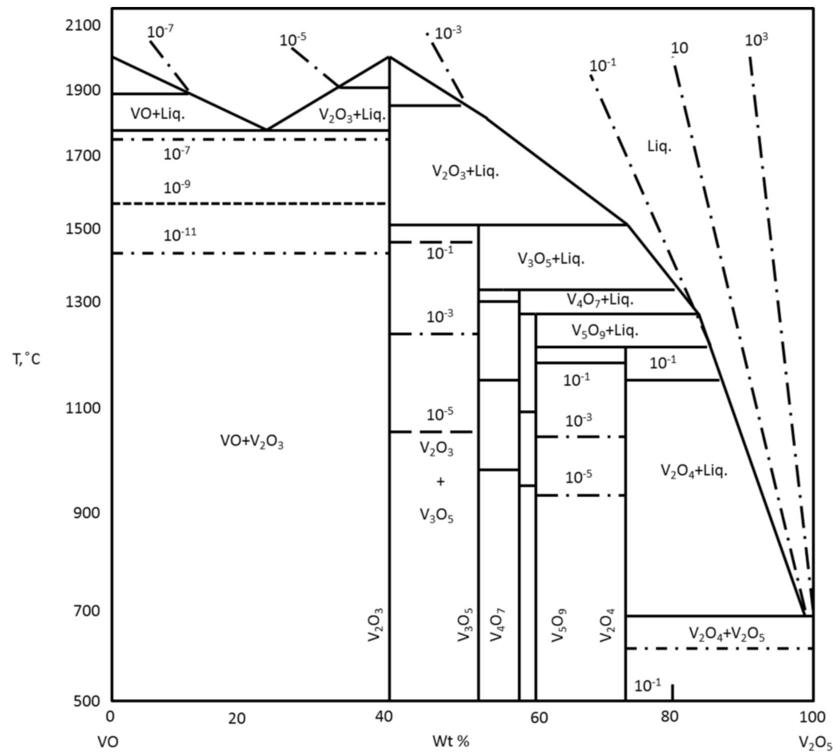

Figure 2.1: Vanadium oxygen (V-O) system [2.2].

2.2 Vanadium Dioxide (VO_2)

VO_2 (M1) monoclinic is the most stable with rutile phase and undergoes a semiconductor-metal transition (SMT) or metal-insulator transition (MIT) near 68 °C in the bulk crystal [2.3 – 2.4]. Figure 2.2 indicates a typical case of such drastic changes in electrical resistance and optical reflectance properties around 68 °C through the VO_2 (M1) MIT in conjunction with hysteresis loops. At low temperatures below 68 °C during transition phase, VO_2 is a monoclinic structure (M1), an insulator and infrared (IR) transparent material. At high temperatures above 68 °C during transition phase, VO_2 changes to a tetragonal rutile structure (R), metallic phase and highly IR reflecting material. Figure 2.3 shows the two crystallographic structures. These structures indicate the complex interaction between electronic and structural degrees of freedom

among the following proposed mechanisms: (1) electron-electron repulsion which results from carrier localization and is called a Mott-Hubbard correlation and (2) lattice instability emanating from unit-cell-doubling known as Peierls distortion [2.5].

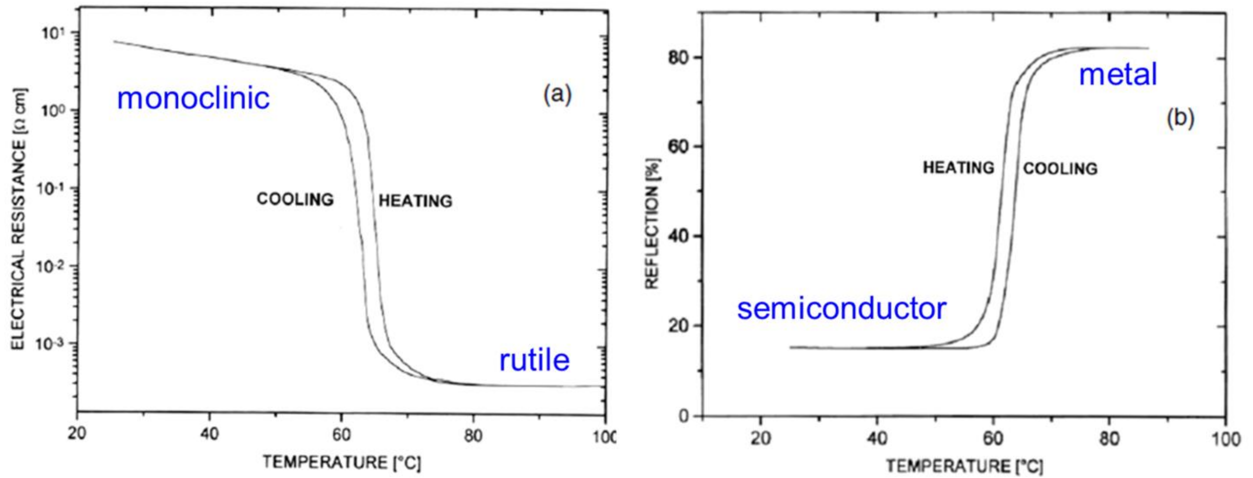

Figure 2.2: A typical case of temperature dependence of the (a) electrical resistance and (b) optical reflectance for VO_2 thin film [2.3].

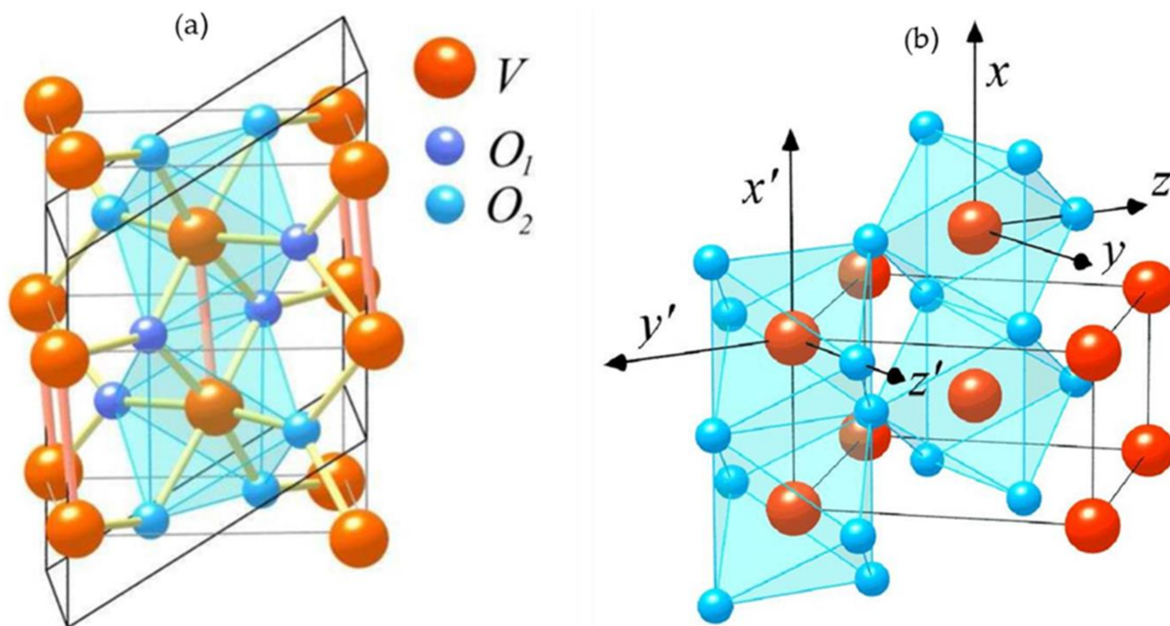

Figure 2.3: (a) VO_2 (M1) monoclinic $P2_1/c$ (insulator) below transition temperature and (b) VO_2 tetragonal rutile $P4_2/mnm$ (metal) above the transition temperature [2.5].

2.3 Crystal Structure

At high temperatures (above 68 °C), VO_2 metallic phase has a tetragonal rutile (R) structure as indicated in Figure 2.3(b). VO_2 exhibits the monoclinic structure (M1) in the insulator phase at low temperature, 25 °C as shown in Figure 2.3(a). The atomic position of V and O atoms are shown in Table 2.1, and every V atom is located by its own O octahedron. The lattice constants parameters of VO_2 (M1) and VO_2 (R) are shown in Table 2.2, respectively. The spaces group of tetragonal rutile (R) and the monoclinic (M1) structure are $P4_2/mnm$ and $P2_1/c$ as given in Table 2.2, respectively. In monoclinic lattice, the V atoms are pairing and bending in accordance with the rutile c-axis during the deformation of the high temperature tetragonal rutile structure. The obtained monoclinic unit cell is double the size of tetragonal rutile unit cell as shown in Table 2.2. M1 is the name of this VO_2 phase because there is another monoclinic lattice named M2. This M2 VO_2 phase can be observed by introducing light doping in VO_2 [2.8], applying a small uniaxial pressure [2.9], and using a peculiar synthesis condition [2.10]. It has been believed that structural changes take place at the same temperature as the MIT but now it has been discovered that MIT and structural collapse happens at different temperatures about 9 °C apart [2.12].

Table 2.1: This table indicates atomic position of V and O atoms.

Atomic position [2.6 - 2.12]	
Atom	Position
V	(0, 0, 0) and (½ , ½, ½)
O	+/-(u, u, 0) and +/-(½+u, ½-u, ½)
	Please note that at 360 °C u = 0.3001

Table 2.2: This table indicates lattice parameters for VO_2 (M1) and (R), respectively.

Lattice parameters [2.6 - 2.12]	
VO_2 (M1)	VO_2 (R)
Room temperature (25 °C)	>70 °C
a_M = 5.7517 Å	a_R = 4.5546 Å
b_M = 4.5378 Å,	-
c_M = 5.3825 Å, β = 122.646	C_R = 2.8514 Å
$P2_1/c$	$P4_2/mnm$

2.4 Energy Band Structure

The VO_2 (M1) electronic and structural details of both phases was first proposed by Goodenough [2.11] and summarized by Cavalleri *et al.* [2.12] as shown in Figures 2.4

and 2.5. The VO_2 structural transition coincides with changes in the electronic band structure near the Fermi level (E_F). The hybridization of O 2p and V 3d orbitals is the outcome of the band structure and also reveals the symmetries of the atomic arrangement in the crystal lattice. This can be explained by making use of the Goodenough model which is based on mean crystal-field theory [2.11]. The model is the consequence of the octahedral environment and the associated hybridization of the O 2p orbitals accompanied by V 3d orbitals (p-d hybridization) which are required in chemical bonding. An edge-sharing chain beside the c-axis is formed in the rutile structure ($P4_2/mnm$) by the V atoms enclosed with O octahedral. Figure 2.5 indicates a combination of low t_{2g} and high e^a_g energy states, where the symmetry of the V-O bonds (σ) is broken into two in the 3d electronic levels of the V ions. The t_{2g} orbitals is further separated into a single a_{1g} orbital and a doubly degenerate e^{π}_g combination with π-type V-O bonds because of the small orthorhombic crystal field component related to the different equatorial and apical V-O distances. The hybridization of e^{π}_g and the e^{σ}_g orbitals with O 2p orbitals results in the formation of a low energy bonding combination with predominantly O 2p character, and high energy bonding combination with predominantly V 3d character. The a_{1g} orbitals are controlled near the rutile c-axis and are relatively non-bonding with respect to O 2p.

Figure 2.5 indicates the metallic monoclinic phases ($P2_1/c$), the density of states at E_F is established from a combination of the $d_{//}$ orbitals that are directed along c_R and the more isotropic and anti-bonding e^{π}_g orbitals (π^*). The dimerizing and titling of the V-V pairs across the SMT/MIT results in a splitting into a bonding and an antibonding combination of highly directional $d_{//}$ orbitals that mediate V-V bonds. Additionally, the

3d-π bands proceed to higher energies because of the increased p-d overlap which occurs due to the anti-ferroelectric displacement perpendicular to c_R and parallel to the crystallographic [110] directions. As a result at the insulating state, there are orbitals polarization with bonding $d_{//}$ orbitals being entirely filled and the anti-bonding $d_{//}$ ($d_{//*}$) and π* not being filled as shown in Figure 2.5.

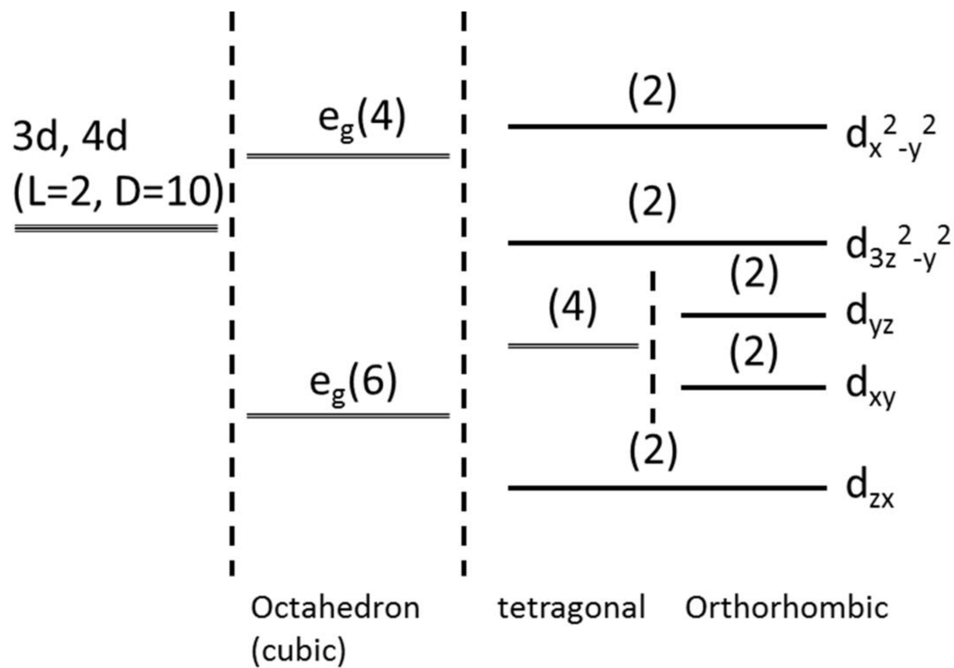

Figure 2.4: Schematic diagram of d-electron band splitting by crystal fields and their orbitals [2.11, 2.13].

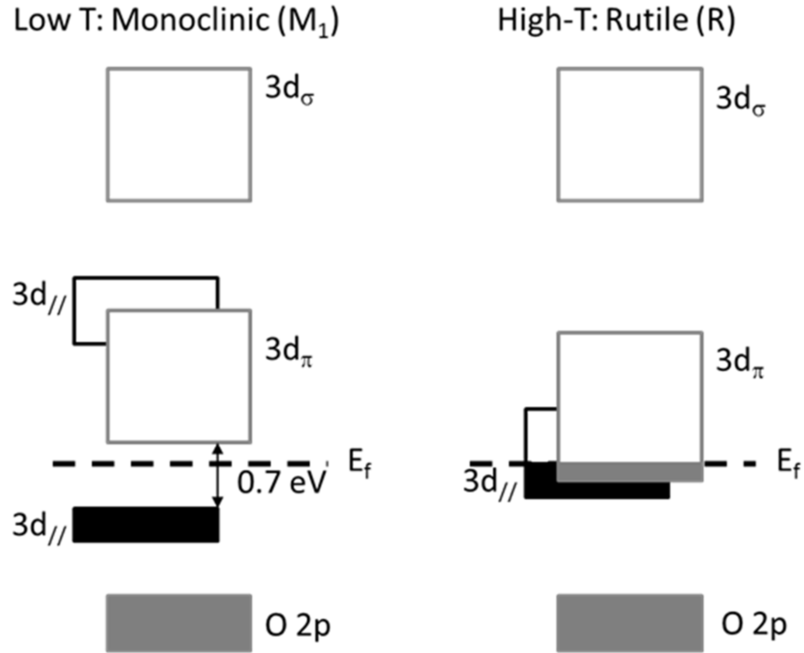

Figure 2.5: Schematic diagram of VO_2 energy-level [2.11, 2.13].

2.5 Peierls or Mott-Hubbard Transition Mechanism

The description of the VO_2 driving principle of the phase transition has been a matter of ongoing dilemma for decades [2.13]. Several studies have focused on resolving the driving force of the combined electronic-structural transition [2.11, 2.12, 2.14]. The issue is whether the given phase transition is an electron Mott transition [2.11, 2.13] accompanied with structural changes or a Peierls-type transition [2.5, 2.15, 2.16] in which structural changes dominate, and the rearrangement of the electron subsystem is an auxiliary process. This dilemma remains unanswered. Usually, in the Peierls model (above 68 °C) at the structural phase transition, the lattice transformation with the band structure changes which lead in the opening of the bandgap and hence the SMT/MIT [2.13]. The material in this case is called a band insulator. In the Mott transition model case, it is only the electron correlations responsible for the transition of the insulating state, while the secondary importance of the SMT/MIT are the ion

arrangements and lattice-to-electron interactions [2.11, 2.12]. In this case, the material is called a Mott or Mott-Hubbard insulator. The primary mechanism responsible for the insulating state of VO_2 is considered to be electron-to-electron correlations. However, recent models generally go further than the standard Mott-Hubbard model i.e. the electron-lattice interactions.

In the metallic phase (high temperature), it is a rutile structure with two molecules per cell is observed, whereas in the insulating phase (low temperature), it is a monoclinic (M1) structure with zigzag-type pairing of V-atoms is observed. This zigzag pairing is observed along the c-axis, which is twice the cell size and brings the number of structural degrees of freedom to 13. Both the VO_2 phases are nonmagnetic. The conduction band of the metallic VO_2 electronic structure is made of crystal-field-split vanadium d orbitals which, depending on their symmetry, are differently hybridized with oxygen p orbitals. There are two degenerate bands that the Fermi levels fall within. The first degenerate band, is a narrow $d_{//}$ band, one essentially made of d orbitals overlapping along the c-axis and accommodating two electrons per vanadium atom. The second degenerate band, is a wider anti-bonding π^* band, made up of d orbitals pointing towards oxygen atoms and hybridized with their p orbitals and accommodating four electrons per vanadium atom. The V^{4+} ion of the $d_{/}$ configuration allows a single electron to be shared by both degenerate bands. The $d_{//}$ band is highly anisotropic while the orbital π^* is more spherical due to their different widths and anisotropies. These bands are expected to respond either to electron-electron interaction, specific to the narrow $d_{//}$ band only, or to a lattice distortion. According to the theory proposed by Goodenough [2.11], and which is confirmed by cluster

calculation, the anti-bonding π^* band rises above the Fermi level because of the lattice distortion and the $d_{//}$ band becomes half-filled. Additionally, the $d_{//}$ band splitting may originate from either vanadium pairing along the c-axis, Peierls mechanism or from the opening of a correlation gap, by the Hubbard mechanism.

Cavalleri *et al.* [2.12] studied the VO_2 MIT/SMT mechanism by making use of time-resolved spectroscopy in the ultrafast timescale. The transmission and reflection measurements of the film were carried out on several wavelengths as a function of 1.5 ps to 15 fs, pulse duration. They found that the VO_2 rutile high transition temperature structure is important for the evolution of the VO_2 monoclinic low transition temperature structure. Additionally, this finding is indicative of a notable bandlike character of the monoclinic phase which is Peierls-like. Biermann *et al.* [2.17] theoretically investigated the VO_2 structural changes by making use of a cluster extension of dynamical mean-field theory (C-DMFT) in conjunction with density approximation (DFT-LDA) within the local density approximation (DFT-LDA). They believed that in order to understand the VO_2 transition mechanism theoretically, an equal footing in structural and correlations aspects by picking V-V pairs as the basic calculation unit is required. The result shows the importance of the V-V dynamical singlet pairs to activate the opening of a Peierls gap. They concluded that VO_2 (M1) is not a Mott-insulator as believed. Haverkort *et al.* [2.18] investigated the magnetic correlations role as well as the orbital structure of the component part of VO_2 transition phase by making use of the soft-x-ray absorption spectroscopy measurement and simulation were carried out at the V $L_{2/3}$ (2p – 3d) edges of the VO_2 single crystals. Their measurement results showed a higher sizeable switching of the orbital occupation

through the VO_2 transition phase than V_2O_3. This result shows the importance of the orbitals and lattice's role in the correlated motion of the electrons. They conclude that the VO_2 phase transition mechanism can be regarded as an orbital-assisted collaborative Mott-Peierls transition. Qazilbash *et al.* [2.19] investigated electronic characteristics of the correlated VO_2 phase transition at 20 nm length scales by making use of infrared spectroscopy and nano-imaging technique in a narrow temperature range. Their system managed to measure the divergent quasi-particle mass in the nano-scale metallic puddles by imaging the appearance and temperature evolution at the beginning of the VO_2 phase transition. Their reported results indicated a strongly correlated conducting condition showing that nano-scale metallic bundles exists inside the VO_2 phase transition and have unique characteristics of the MIT/SMT VO_2 phase. They concluded that the VO_2 (M1) phase can be referred to as a Mott insulator because of the competing effects of charge ordering that is mostly generated by electron-phonon interactions.

2.6 Other Phase of VO_2

Generally, VO_2 is a dual compound with different polymorphs. There are several forms of VO_2 phases that include VO_2 (M1) [2.1], VO_2 (R) [2.20], VO_2 (B) [2.21], VO_2 (A) [2.22], VO_2 (C) [2.23], VO_2 (D) [2.24], VO_2 (BCC) [2.25] and VO_2 (C) [2.26] which have recently been reported. The recently discovered polymorphs (D, BCC and N) studies are still at a synthesis stage.

The VO_2 structure of these polymorphs VO_2 (M1), VO_2 (R), VO_2 (B) and VO_2 (A) are generally founded on bcc lattices of O with V in the octahedral sites, the O octahedral being more or less regular [2.27]. The O octahedral in the case of the VO_2 (R) and in deformed VO_2 (M1) can be placed either along two perpendicular directions; or O octahedral can be mostly arranged along one direction as similar in VO_2 (B) and VO_2 (A). Although these VO_2 polymorphs have similar stoichiometry, their structures are very unique and correspond to two different values for the density as given in Table 2.1.

Table 2.3: Density of VO_2 polymorphs [2.27].

VO_2 polymorphs	Density (g/cm^3)	MIT temperature
VO_2 (R)	4.67	68 °C [2.1]
VO_2 (M1)	4.67	68 °C [2.1]
VO_2 (B)	4.03	-
VO_2 (A)	4.04	-

The two other VO_2 polymorphs have bigger cells than the tetragonal rutile phase with octahedral mostly packed along one crystallographic direction. Theobald *et al.* [2.21] was the first to report a VO_2 (B) monoclinic phase as a new polymorph by reduction of V_2O_5 in several gases and vapour. The monoclinic cell parameters for VO_2 (B) are a_B = 120.3 Å, b_B = 3.693 Å, c_B = 6.42 Å and β = 106.6 ^{o}, z = 8 and the space group is c_2/m. The VO_2 (B) structure can be considered as made by two similar layers of atoms along b. The second octahedral layer is moved with reference to the first one by (½, ½, 0); in the VO_2 (B), (010) plane. Two octahedral types are formed in the VO_2 (B) structure because the

O octahedral are deformed and the V atoms being no longer in the centre. VO_2 (B) forms platelets like V_6O_{13} and the size of platelets depends on the synthesis method. These platelets are preferentially oriented and grow in (a, b) planes because this one forms a network of corner sharing octahedra in the plane. The difference between the VO_2 (B) and V_6O_{13} is in the way the octahedra are linked in the (a, b) plane. They exhibit a similar [001] X-ray diffraction (XRD) pattern. Theobald *et al.* [2.22] were the first to report on VO_2 (A) metastable phase as an intermediate phase in the conversion of VO_2 (B) to VO_2 (R). Oka *et al.* [2.28] and Yao *et al.* [2.29] fully characterized the VO_2 (A) phase. The VO_2 (A) has a tetragonal structure with the following cell parameters a = b = 8.44 Å, c = 7.68 Å, z = 16 [2.28]. The VO_2 (A) space group is $P4_2/nmc$ [2.28]. The fourfold axes of the O octahedra are arranged along a solo direction like in VO_2 (B), in this case the c-axis of the tetragonal structure. The c parameter is approximately twice the b-axis of VO_2 (B), the O octahedra are less deformed than in VO_2 (B) when there is only one type of octahedra.

2.7 Applications of VO_2

During the VO_2 phase transition, the VO_2 also shows a reversible abrupt change of optical transmittance or reflectance especially in the infrared (IR) region [2.1]. VO_2 (M1) thin films and nano-particles tend to survive the stress generated during repeated cycles of phase transition better than the bulk crystals, and their transition temperature can also be reduced to the ambient temperature by element doping such as tungsten [2.30]. These properties make VO_2 (M1) an attractive material for technological applications, such as “smart windows” for energy saving and comfort [2.31], sensors, as

well as actuators [2.32], electrochromic and photochromic memory optical devices [2.33], high-speed solid-state optical displays [2.34] and e.t.c.

2.8 VO_2 Synthesis

There are several methods established to produce VO_2 thin films. The techniques consist of chemical vapour deposition [2.13], reactive evaporation [2.35], reactive sputtering in O_2 background of a V target [2.36], PLD and numerous post-deposition annealing methods where either over-oxidized phases such as V_2O_5 are reduced to VO_2 by annealing [2.37] or pure V thin films are annealed in O_2 to obtain the VO_2 stoichiometry [2.38]. Several studies have been done on the thin film microstructure effect and synthesis conditions on VO_2 properties [2.39]. In order to obtain a sharp and strong transition in VO_2, a substrate temperature around 500 °C were used in the synthesis [2.37]. VO_2 thin film deposited at higher temperatures are likely to deposit films with larger grain sizes, while those deposited at lower temperatures have smoother surfaces and smaller grain sizes [2.37]. Additionally, there are few reports on VO_2 materials reporting on SMT/MIT deposited at low temperatures.

2.9 VO_2 switching properties

The switching properties of VO_2 is characterise by the temperature of MIT, the thermal hysteresis loops shape, sharpness, width and switching ratio. Normally, UV-Vis-NIR spectrophotometer and four-point-probes are the techniques used to study the optical and electrical switching properties of VO_2 from the room temperature monoclinic

structure to above 68 °C tetragonal rutile structures [2.3]. Basically, the wavelength dependent transmittance/reflectance is measured in the range of 300 – 2500 nm temperature cycling from room temperature to 100 °C corresponding to VO_2 MIT. There are several techniques used in the literature to determine the MIT temperature such as midpoint hysteresis loop [2.40], derivative of the heating and cooling profiles of the resistance/transmittance allows the estimation of average value of the MIT temperature [2.41] and the minimum of the derivative of the temperature dependence of transmittance/resistance [2.42] among others.

There are several factors that determined the switching properties of VO_2 thin films that are size effects [2.43], distribution, orientation [2.44], crystallinity, stoichiometry and impurities [2.2, 2.45] as well as interface energy [2.46 – 2.47]. Table 2.4 indicates the size effects on MIT. The results indicate that as the grain size decreases the MIT decreases. Normally, higher crystallinity can produce bigger switching ratio results in higher thermal hysteresis loops. Xinhong et al. [2.48] obtained higher and lower crystallinity VO_2 thin films. The higher crystallinity thin film indicated 28% height of thermal hysteresis loop with particle size of 90 nm. Whereas the lower crystallinity thin film obtained 15% height of thermal hysteresis loop with particle size of 70 nm. Additionally, their obtained higher purity VO_2 thin film resulted also to a higher thermal hysteresis loop. For example, this thin film contained VO_2 (M1) as a main phase and it obtained 34% height of thermal hysteresis loop than the thin film has $Zn_2V_2O_7$ as the main phase which got 8% height thermal hysteresis loop.

Table 2.4: Size effects [2.43]

MIT	Grain size
65	3 μm
58	2 μm
52	1 μm
42	0.5 μm

2.10 Summary

In this chapter, the structural, optical transmission/reflective and electrical resistivity properties of VO_2 (M1), as well as the principle of the VO_2 (M1) transition were discussed. We briefly discussed the other phases of VO_2, VO_2 (M1) applications and VO_2 synthesis techniques.

References

2.1 U. Schwingenschlögl, V. Eyert, “The vanadium Magnéli phases V_nO_{2n-1}”, Ann. Phys. (Leipzig) **13** (9), 475 (**2004**).

2.2 C.H. Griffith, H.K. Eastwook, “Influence of stoichiometry on metal-semiconductor transition in vanadium dioxide”, J. Appl. Phys. **45**, 2201 (**1974**).

2.3 F.J. Morin, “Oxides which show a metal-to-insulation at the Neel temperature” Phys. Rev. Lett. **3** (1), 34 (**1959**).

2.4 F. Dumas-Bouchiat, C. Champeaux, A. Catherinot, “rf-microwave switches based on reversible semiconductor-metal transition of VO_2 thin films synthesised by pulsed-laser deposition”, Appl. Phys. Lett. **91**, 223505 (**2007**).

2.5 A. Zylbersztejn, N.F. Mott, “Metal-insulator transition in vanadium dioxide”, Phys. Rev. B **11** (11), 4383 (**1975**).

2.6 A.D. Burton, P.A. Cox, "A model for electroic structure of VO_2", Philos. Mag. B **51** (2), 255 (**1985**).

2.7 G. Andreson, "Studies on vanadium oxides. II the crystal structure of vanadium dioxide", Acta. Chem. Scand. **10**, 623 (**1956**).

2.8 C.N. Berglund, H.J. Guggenheim, "Electronic properties of VO_2 near the semiconductor-metal transition", Physical Rev.**185** (3), 1022 (**1969**).

2.9 J.C. Rakotoniaina, R. Mokrani-Tamellin, J.R. Gavarri, G. Vacquier, A. Casalot, G. Calvarin, "The thermochromic vanadium dioxide: I. Role of stresses and substitution on switching properties", J Solid State Chem. **103** (1), 81 (**1993**).

2.10 J.M. Longo, P. Kierkegaard, "A refinement of the structure of VO_2", Acta Chem. Scand. **24**, 420 (**1970**).

2.11 J.B. Goodenough, "The two components of the crystallographic transition in VO_2", J. Solid state Chem. **3**, 490 (**1971**).

2.12 A. Cavalleri, T. Dekorsy, H.H.W. Chong, J.C. Keiffer, R.W. Schoenlein, "Evidence for a structurally-driven insulator-to-metal transition in VO_2: A view from the ultrafast timescale", Physical Rev. B **70**, 161102 (**2004**).

2.13 R.M. Wentzcovitch, W.W. Schulz, P.B. Allen, "VO_2: Peierls or Mott-Hubbard? A view from band theory", Physical Rev. Lett. **72** (21), 3389 (**1994**).

2.14 V. Eyert, "The metal-insulator transitions of VO_2: A band theoretical approach", Ann. Phys. (Leipzig) **11** (9), 1-61 (**2002**).

2.15 D. Paquet, P. Leroux-Hugon, "Electron correlations and electron-lattice interactions in the metal-insulator, ferroelastic transition in VO_2: A thermodynamixal study" Physical Rev. B **22** (11), 5284 (**1980**).

2.16 H. Kim, Y.W. Lee, B. Kim, B. Chae, S.J. Yun, K. Kang, K. han, K. Yee, Y. Lim. “Monoclinic and correlated metal phase in VO_2 as evidence of the mott transition: coherenct phonon analysis”, Physical Rev. Lett. **97**, 266401 (**2006**).

2.17 S. Biermann, A. Poteryaev, A.I. Lichtenstein, A. Georges, “Dynamical singlets and correlation-assisted peierls transition in VO_2”, Phys. Rev. Lett. **94**, 026404 (**2005**).

2.18 M.W. Haverkort, Z. Hu, A. Tanaka, W. Reichelt, S.V. Streltsov, M.A. Korotin, V.I. Anisimov, H.H. Hsieh, H.-J. Lin, C.T. Chen, D.I. Khomskii, L.H. Tjeng, “Orbital-assisted metal-insulator transition in VO_2”, Phys. Rev. Lett. **95**, 196404 (**2005**).

2.19 M.M. Qazilbash, M. Brehm, Byung-Gyu Chae, P.-C. Ho, G.O. Andreev, Bong-Jun Kim, S.J. Yun, A.V. Balatsky, M.B. Maple, F. Keilmann, Hyun-Tak Kim, D.N. Basov, “Mott transition in VO_2 revealed by infrared spectroscopy and nano-imaging”, Science **318** (5857), 1750 (**2007**).

2.20 S. Westman, “Note on a Phase transition in VO_2” Acta Chem. Scand. **15**, 217 (**1961**).

2.21 F. Théobald, R. Cabala, J. Bernard, “Essai sur la structure de VO_2(B)” J. Solid State Chem. **17** (4), 431 (**1976**).

2.22 F. Theobald, “Ètude hydrothermale du systéme VO_2-$VO_{2,5}$-H_2O” J. Less Common Met. **53** (1), 55 (**1977**).

2.23 D. Hagrman, J. Zubieta, C.J. Warren, L.M. Meyer, M.M.J. Treacy, R.C. haushalter, “A new polymorph of VO_2 prepared by soft chemical methods” J. Solid state Chem. **138**, 178 (**2012**).

2.24 B.Y. Qu, L. Liu, Y. Xie, B.C. Pan, “Theoretical study of the new compound VO_2 (D)”, Phys. Lett. A **375** (39), 3474 (**2011**).

2.25 J. Xie, C. Wu, S. Hu, J. Dai, N. Zhang, J. Feng, J. Yang, Y. Xie, “Ambient rutile VO_2(R) hollow hierarchitectures with rich grain boundaries from new-state nsutite-type

VO_2, displaying enhanced hydrogen adsorption behavior" Phys. Chem. Chem. Phys. **14**, 4810 (**2012**).

2.26 S.R. Popuri, M. Miclau, A. Artemenko, C. Labrugere, A. Villesuzanne, M. Pollet, "Rapid hydrothermal synthesis of VO_2(B) and its conversion to thermochromic VO_2(M1)" Inorg. Chem. **52** (9), 4780 (**2013**).

2.27 Ch. Leroux, G. Nihoul, G. Van Tendeloo, "From VO_2(B) to VO_2(R): Theoretical structures of VO_2 polymorphs and in situ electron microscopy", Physical Rev. B **57** (9), 5111 (**1998**).

2.28 Y. Oka, T. Ohtani, N. Yamamoto, T. Takada, "Phase transition and electrical properties of VO_2(A)"J. Ceram. Soc. Jpn. **97**(1130), 1134 (**1989**).

2.29 T. Yao, Y. Oka, N. Yamamoto, "A structural study of the high-temperature phase of VO_2(A)" J. Solid State Chem. **112**, 196 (**1994**).

2.30 T.D. Manning, I.P. Parkin, "Atmospheric pressure chemical deposition of tungsten doped vanadium (IV) oxide from $VOCl_3$, water and WCl_6", J. Mater. Chem. **14**, 2554 (**2004a**).

2.31 Z.P. Wu, A. Miyashita, S. Yamamoto, Z.J. Zhang, K. Narumi, H. Naramoto, "Optical properties of vanadium dioxide thin film as a windows thermochromic coating", Mater. Construct. **50**, 5 (**2000**).

2.32 R.T.R. Kumar, B. Karunagaran, D. Mangalaraj, S.K. Narayandass, P Manoravi, M Joseph, V Gopal, "Pulsed laser deposited vanadium oxide thin films for uncooled infrared detectors sensors actuators A **107**, 62 (**2003**).

2.33 H. Jerominek, F. Picard, D. Vincent, "Vanadium oxide films for optical switching and detection", Opt. Eng. **32**, 2092 (**1993**).

2.34 M. Gurvitch, M. Halioua, A. Kastalsky, S. Naar, S. Skhokhor, High speed solid state optical display ed U S P Office (USA: Copytele), (**1999**).

2.35 P.J. Hood, J.F. Denatale, "Millimeter-wave dielectric properties of epitaxial vanadium dioxide thin-films", J. Appl. Phys. **70** (1), 376 (**1991**).

2.36 P. Jin, K. Yoshimura, S. Tanemura, "Dependence of microstructure and thermochromism on substrate temperature for sputter-deposited VO_2 epitaxial films", J. Vac. Sci. Technol. A **15**, 1113 (**1997**).

2.37 W.J. Kitchen, G.R. Proto, "Properties of vanadium dioxide thermal filaments", J. Appl. Phys. **42** (5), 2140 (**1971**).

2.38 F.C. Case, "Simple resistance model fit to the oxidation of a vanadium film into VO_2", J. Vac. Sci. Technol. A **6** (1), 123 (**1988**).

2.39 J. Narayan, V.M. Bhosle, "Phase transition and critical issues in structure-property correlations of vanadium oxide", J. Appl. Phys. **100** (10), 103524 (**2006**).

2.40 L. Kang, Y. Gao, H. Luo, "A novel solution process for the synthesis of VO_2 thin films with excellent thermochromics properties", Appl. Mater. And Inter. **1** (10), 2211 (**2009**).

2.41 L. Mathevula, B.D. Ngom, L. Kotsedi, P. Sechogela, T.B. Doyle, "Thermochromic VO_2 on Zinnwaldite Mica by pulsed laser deposition", Appl. Sur. Sci. **314**, 476 (**2014**).

2.42 A.R. Begishev, G.B. Galiev, A.S. Ignat'ev, V.G. Mokerov, V.G. Poshin, "Influence of deviations from the crystal lattice periodicity on the semiconductor-metal phase transition in vanadium dioxide", Sov. Phys. Solid State **20** (6), 951 (**1978**).

2.43 L. Hongwei, L. Junpeng, Z. Minrui, T.S. Hai, S.C. Haur, Z Xinhai, K. Lin, "Size effects on metal-insulator phase transition in individual vanadium dioxide nanowires", Opt. Express **22** (25), 307055 (**2014**).

2.44 D. Brassard, S. Fourmax, M. Jean-Jacques, J.C. Kieffer, M.A.E. Khakani, "Grain size effect on the semiconductor-metal phase transition characteristics of magnetron-sputtered VO_2 thin films", Appl. Phys. Lett. **87**, 051910 (**2005**).

2.45 J.Y. Suh, R. Lopez, L.C. Feldman, R.F. Haglund Jr, "Semiconductor to metal phase transition in the nucleation and growth of VO_2 nanoparticles and thin films", J. Appl. Phys. **96** (2), 1209 (**2004**).

2.46 R. Lopez, T.E. Haynes, L.A. Boatner, "Size effects in the structural phase transition of VO_2 nanoparticles", Phys. Rev. B **65**, 224 (**2002**).

2.47 R. Lopez, L.A. Boatner, T.E. Haynes, R.F. Haglund Jr., LC Feldman, "Optical nonlinearities in VO_2 nano-particles and thin films", Appl. Phys. Lett. **85**, 5191 (**2004**).

2.48 C. Xinhong, T. Haizheng, W. Meinan, W. Shuo, N. Zhiyong, X. Na, Z. Xiujian, "Effect of annealing duration and substrates on structure and property of vanadium dioxide films", Wuhan University. Techn. Mater. Sci. Ed. **29** (6), 1117 (**2014**).

Chapter 3

Pulsed Laser Induced Plasma

In this chapter, the importance of laser induced plasma (LIP) in PLD for the growth of vanadium oxide (V_xO_y) nano-particles was discussed. The physics and theory of the laser-solid-plasma interactions together with the plasma expansion, resulting in thin film deposition will be discussed.

3.1 Pulsed Laser Deposition (PLD)

PLD was successfully demonstrated in-situ by depositing $YBaCu_3O_7$ (YBCO) thin films during late 1987 and early 1988 [3.1] and has now widely been used to synthesize epitaxial thin films of most oxide material. PLD is a physical vapour deposition technique and a derivative of laser ablation (LA), which is the standard procedure of laser-induced removal of material, for the growing of thin films from elements or compounds [3.2]. PLD makes use of a focused high energy laser beam which is pulsed on a target surface of interest to the experiment which undergoes absorption and vaporization of a thin surface region onto a substrate; a typically example, onto a Corning glass facing the target. The deposition process can take place in vacuum of about 10^{-5} mbar as well as in the presence of a reactant gas at slightly higher than 10^{-5} mbar, for example oxygen (O_2), argon (Ar) or nitrogen (N_2). The PLD schematic diagram is shown in Figure 3.1. The typical schematic diagram for a PLD experimental set-up is simpler than other synthesis techniques, but the phenomenon of the laser-to-target

interaction and subsequent growth of the layer on the substrate is complicated and can mainly be divided as follows:

- Evaporation regime which govern the heating of the target atoms by the laser beam and subsequent evaporation of the target atoms.
- Isothermal regime: this regime comprises the balance between the heating effect from laser beam which raises temperature and the expansion of the plasma which tends to reduce the heating. The two opposing mechanisms lead to constant temperature or an isothermal condition.
- Laser-induced plasma regime: this time there is no heat gain or loss but the plume continues to expand and it temperature begins to rise. The fact that there is no heat gain or loss, the process is referred as being adiabatic. However there is transfer of energy between the plume species which transforms into kinetic energy of the species which in turn propels the species to the substrate, and
- Growth of a layer regime which is defined as deposition process of the plasma species to the surface substrate, typically Corning glass.

The description of the PLD phenomenon is possible only in approximation because of the correlation between the above physical mechanisms involvement in the process. Moreover, this is the reason why they are several theoretical models [3.2, 3.3, 3.4, 3.5] which describe each of the PLD mechanisms in isolation rather than explaining all the PLD processes.

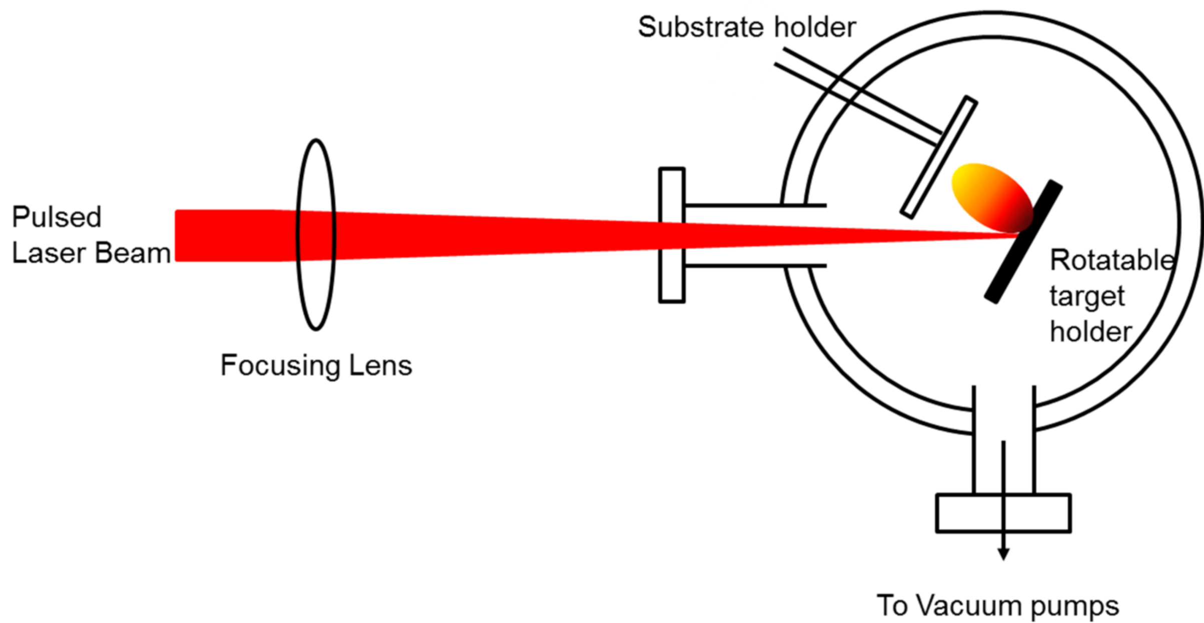

Figure 3.1: A typical schematic illustration for the PLD experimental set-up.

3.2 Laser Induced Plasma (LIP)

Figure 3.2 [3.6] indicates the interaction of high laser pulse energy and an object in any state of aggregation, the plasma is then formed and this process is called laser induced plasma (LIP). This happens when the pulse duration, τ_p, exceeds 100 picoseconds; the uptake of the entire laser pulse energy by the target results in the formation of a plasma as shown in Figure 3.2. LIP is characterised by strong emission of radiation due to the high temperature of excitation and density of electrons. Moreover, the plasma parameters and composition can be determined from the LIP investigation/study. There are several key parameters that LIP characteristics are strongly dependent upon, such as pulse duration, laser intensity, target material and geometry, wavelength, the nature and pressure of surrounding gases [3.6]. The measurement of the light emission spectrum of the vaporized material at the time of the PLD process is important in the field of material science because it allows the observation of the process as well as the

quality estimation of the results and establishing a relationship between the laser ablation mechanism and the so-made material [3.7, 3.8]. Optical plasma plume emission study can provide detailed evidence on the progression of short-lived species excited atoms, ions or molecules in space and in time. Optical emission spectroscopy (OES) [3.9], mass spectrometry, laser absorption spectroscopy (LAS), beam deflectometry, interferometry, [3.10, 3.11], time resolved imaging using intensified charge coupled device (ICCD) [3.12] are among the problem-solving tools that can be used for determining the plume parameters.

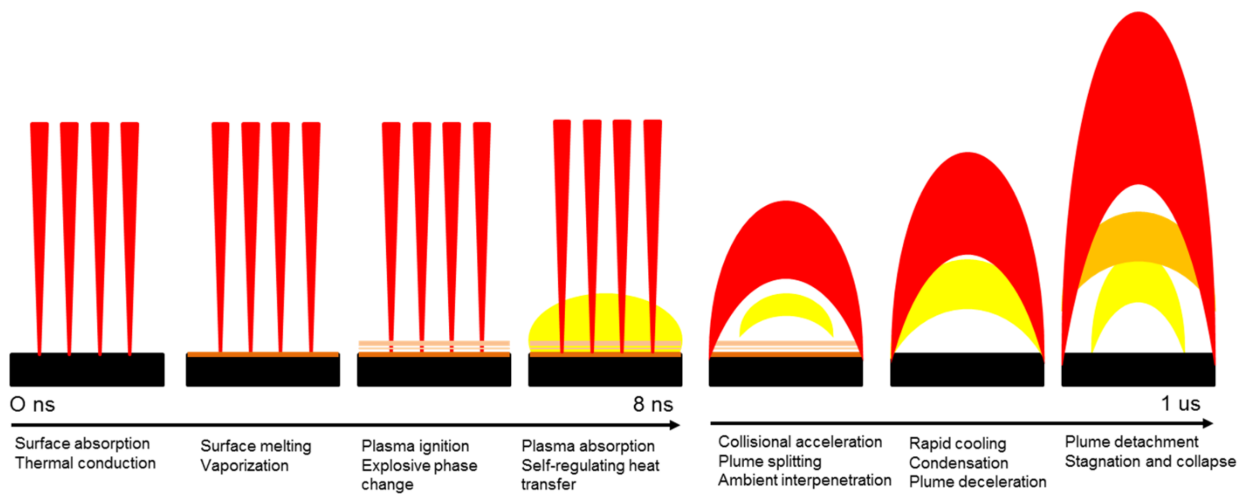

Figure 3.2: The schematic diagram indicates the interaction of high laser pulse energy with matter in any state of aggregation [3.13].

3.3 Laser-Target Interaction

When high-energy pulse of the laser light is focused on a metal target material, the electromagnetic energy is conveyed to the electrons of the surface atoms and causes these electrons to vibrate. The radiation from the laser throb needs to be high enough, at the least 0.9 x 10^9 W/cm^{-2} (in the case of nano-second (ns) pulses), to interact with

the metals in air. The ablation process can occur only when the electrons gain enough kinetic energy as shown in Figure 3.2 [3.13]. The electromagnetic energy is completely and immediately transferred to the electrons and, during the full pulse duration, the electrons continue to gain energy and transfer it to the matrix of the target atoms around them. One of the main mechanisms of the material removed induced by ns laser pulses is ablation which happens owing to melting which leads to boiling, evaporation and ionization into the plasma state. Due to expansion, the cooling effect balance the heating from the laser beam and the heat spreads uniformly in thermal equilibrium (spallation) [3.14].

Generally, much more energy is needed by the target material to vaporize than to melt. This takes place when the target temperature increases due to the laser beam's thermal energy overcoming the vaporization temperature of such a material. The radiation of the target material by pulsed-laser energy is influenced by the laser parameters, namely duration of the pulse τ, density of the pulse energy E, shape and wavelength λ of the pulse; and the temperature dependent thermal properties and optical of the material [3.6].

The laser beam energy deposited on the target is equal to three main forms of energy losses, viz.: (1) the energy absorbed by the target through conduction (2) the energy required to vaporize the surface atoms, (3) the absorption energy losses which leads to the plasma state [3.11]. This leads to some threshold energy, E_{th} which is defined as the minimum energy above which initial evaporation is observed. Each material has its own

laser threshold energy. All the losses in this process depend on pulsed energy density and energy threshold E_{th}. Duration of the pulse, wavelength of the laser beam, and the thermal properties of the material are the parameters that influence the energy threshold [3.6].

Wood *et al.* [3.15] and Singh *et al.* [3.16] are among authors who have executed a full study of the laser-and-solid-target interaction in the nano-second regime. A one-dimensional formula of the heat flow equation is often used to describe the vaporization process and is given as [3.17]

$$\rho c \frac{\partial T}{\partial t} = \frac{\partial T}{\partial z}\left(k \frac{\partial T}{\partial z}\right) + \alpha A I_0 e^{-\alpha z} \tag{3.1}$$

where temperature is T, density is ρ, specific heat is c, thermal conduction is k, absorption coefficient is $\propto$, absorbance of the target surface is A, the incident pulse intensity is I_0 and the coordinate at right angles to the target surface is z. The exact solutions of equation (3.1) is complex because of non-linear boundary conditions for vaporization and solid-liquid interface are not in the same position relative to the incoming laser photons resulting in numerical approaches which are always considered. The region of interest on the surface of the target by the process of laser ablation has the laser spot dimension of x, y on the target surface, multiplied by the heat penetration depth L_{TH}, on the z direction at right angles to the target. The heat penetration depth L_{TH} depends on the coefficient of thermal diffusion, $D = \frac{k}{\rho c}$ of the sample material and on the duration of the pulse, τ_L as given in equation (3.2) [3.18]:

$$L_{TH} \approx \sqrt{2D\tau_L} \tag{3.2}$$

This equation means that the laser-affected-zone is influenced by the duration of the pulse, for instance when the pulse is long then the laser impacted zone becomes the wider and deeper than before. In a nano-second laser pulse there exists sufficient time for the heat wave advancement into the target and the energy is kept absorbed in a layer with a thickness of the order of L_{TH}.

The evaporation process takes place when the absorbed energy in a specific volume is higher than the latent heat of vaporization in the same volume as given the equation below: [3.19, 3.20]

$$\Delta z_v \approx \frac{A(F_L - F_{TH})}{\rho L_v} \qquad (3.3)$$

The laser pulse fluence is given as $F_L = I_0 \tau_P$. The evaporation process takes place from liquid metals in this case and F_{TH} is written in terms of surface layer of the order of L_{TH} as

$$F_{TH} \approx \frac{\rho c \Delta T_m L_{TH}}{A} \qquad (3.4)$$

where T_m is the melting temperature, T_0 is the room temperature and $\Delta T_m = T_m - T_0$. The fluence threshold grows as $\tau_P^{1/2}$. When temperature is low the increase in ablation depth as a function of the laser fluence is linear. But this situation changes when temperature increases. In this latter case, the ablation depth as a function of laser fluence is non-linear [3.21, 3.22]. The situation when the laser pulse energy is above the threshold energy of the target in illustrated in Figure 3.3.

When the radiation of the laser surpasses a certain material energy threshold, the "breakdown" of matter and the resulting of the plasma generation take place. Ionization/recombination and excitation/de-excitation as given in Figure 3.3 by electron impact are the key mechanisms supporting the plasma and the shape of the plasma in the case of ns pulse is semi-spherical three-dimensional symmetries.

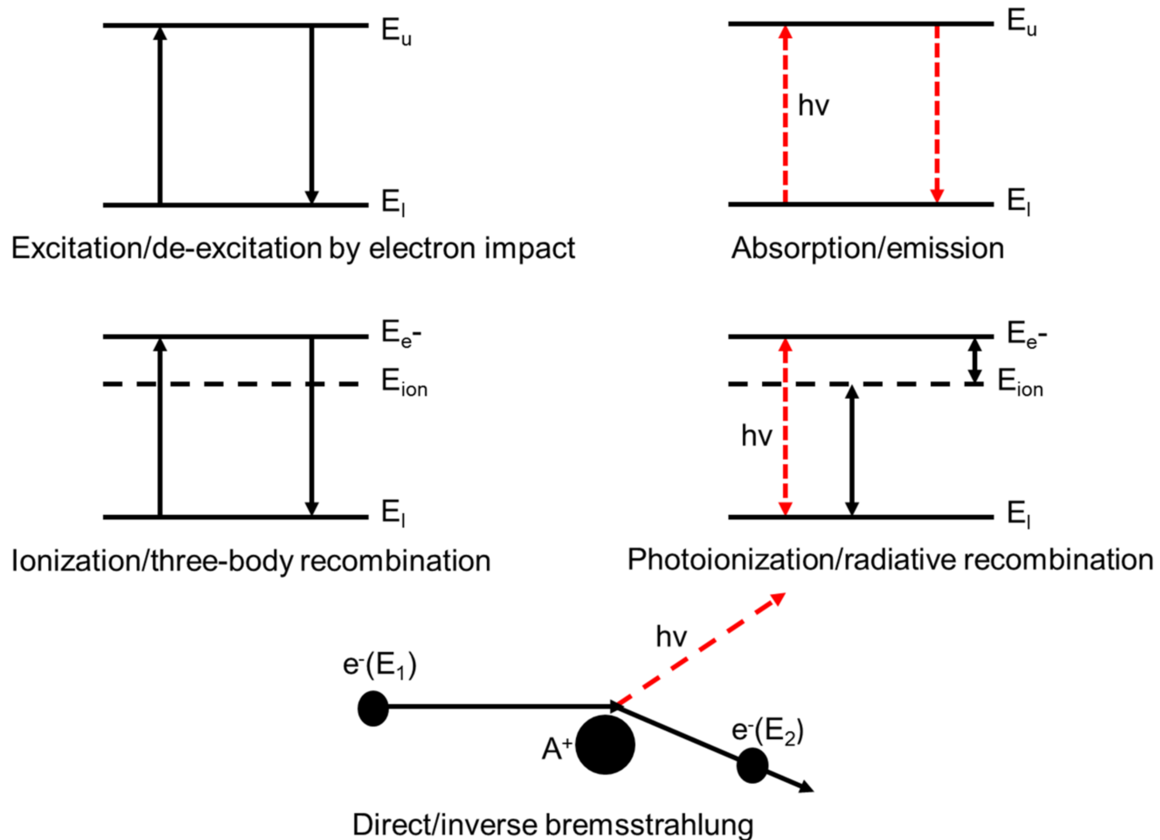

Figure 3.3: Schematic diagram indicating the main laser plasma mechanisms [3.13].

3.4 Laser-Plasma Interaction

As already outlined the preceding sections, when laser heat energy is greater than the target materials threshold energy, melting, boiling and evaporation of surface atoms

happen which leads to ionization or the separation of positive ions and negative electrons (a plasma condition). An isothermally expanding plasma regime is formed when the interaction between the beam and the evaporating materials happens, and this continues until the laser pulse is terminated [3.16, 3.23]. A dynamic equilibrium occurs, during the isothermal expansion regime between the plasma's coefficient of absorption and rapid transformation of thermal energy into kinetic energy. This is controlling the isothermal plasma temperature. The temperature of the evaporated material increases because of the interaction taking place between the laser photons and the growing plasma. This results in a fast rise in temperature to very high values while there is a further acceleration in electrons. A bright plasma plume is obtained because of the photons released from the excited particles. In ns pulse, the laser pulse duration plays an important role because of the developing plasma interacts with the rear end of the laser beam. The electron-ion collision i.e. resistance to induced currents, is the primary absorption mechanism [3.24] and the absorption of the photons primarily occurs by an inverse bremsstrahlung process [3.17, 3.25, 3.26], which involves the absorption of a photon by a free electron as given in Figure 3.3.

3.5 Plasma Plume Expansion

Since the plasma is generated because of the laser pulse, it will start to develop until it comes to the end of its expansion. The expansion will be sustained by collisions, between ions and electrons, as well as radiative processes and in dependence on the following: density of plasma, plasma temperature and environment where the plasma is formed [3.16]. While it has all this time been believed that the plume advanced at right

angles to the target especially at initial stages, this thesis will show this fact in the forthcoming chapters.

A progressive expansion of the plume takes place when there is a further high-pressure kinetic energy region due to the strong laser-plasma interaction. As soon as the laser pulse terminate, the ejection of particles stops. The external environment in which the plasma expands strongly influences the plasma dynamics viz.: (1) extent of aggregation (2) composition of elements and (3) ambient pressure [3.13]. In the event that the plasma expands into some background gas at some specific pressure, the presence of such a gas will influence the processes of expansion of the plasma [3.27]. This expansion ends up generating internal plume structures such as splitting, sharpening, confinement and others. Among the many variables that influence plasma expansion, atomic mass of the ionic species and that of the surrounding gas are equally important [3.28]. It is well known that there are three different regimes of the plume expansion in the background gas pressure case [3.29, 3.30]:

- Free-plume regime or adiabatic regime (at low pressure),
- Collisional regime (at intermediate pressure), and
- Thermalization regime (at high pressure).

The adiabatic expansion regime is formed when the plume expands freely and at constant rate. This is due to the fact that the distance between the atoms in the background gas is much larger than that between the plume species [3.31]. This situation allows for complete absorption of laser energy by the plume and conversion of the same into kinetic energy leading to large plume velocities of expansion.

The species propagate at extremely high velocity during further expansion. Several models have been proposed [3.32], typically the hydrodynamics model [3.33], Monte Carlo simulations [3.34], gas-dynamics and energy conservation equations have been used to describe the plume expansion in the vacuum and low background pressure case [3.35]. Most of these models only managed to simulate the late phases of plasma plume propagation, by making use of the assumption of certain inputs from the parameters of the ablated material either at the end of the laser pulse or before the plume's three-dimensional expansion begins. Moreover, most of these models include certain kinds of surrounding gases and targets. Their effectiveness is fairly limited since these models do not cover a wider range of gases and targets [3.36].

In the case of a plasma plume expanding into high background gas pressure, strong penetration of the laser plasma and surrounding gas are the characteristics of the plume propagation [3.37]. In this situation, the effects of collision begin to influence. When the original removed mass and laser energy forming the plasma are not sufficiently high, the plume can be so weak that no hydrodynamic effects can be observed. The ablated materials diffuse into the background gas. Additionally, during the plume growth the existence of the background gas can furthermore result to reactive scattering, thermalization of the plume and improved condensation which in turn leads to cluster and nano-particles forming [3.38, 3.39].

As the surrounding gas pressure increases, a stronger interaction between the plasma and the background gas happens. This results in the ablated materials beginning to

successfully shift the surrounding gas atoms across to the accumulation of collisions. This results in a compression of the adjacent surrounding gas leading to a hydrodynamics regime of the expanding plume. The plume acts as a piston on the surrounding background gas which counteracts and halts the expansion of the plume. This leads in the confinement of the plume that also impacts the plume cores.

The plume confinement results in the release of several photons from the inner sections of the plume because of the creation of high density peaks of the plume [3.40, 3.41]. Moreover this is likely to increase excitation/ionization at the plume front as a consequence of the heating of the plume; which originates from the collisions. The plume is retarded mostly alongside the normal of the target surface.

3.6 Point-blast-wave Model

Here we will briefly discuss the point-blast-wave [3.42] and classical drag [3.43] models among the plasma plume expansion models in ambient gas. In order to investigate the existence of a shock wave during the expansion of the PLD plume in the presence of surrounding gases, position-time plots as the plume end advances are employed. The laws of conservation of mass, momentum and energy have been applied to determine the velocity of the growing plasma/plume front, the density, pressure and temperature in the shock region. The velocity (V_{sh}), temperature (T_{sh}) and density (ρ_{sh}) of the shocked region are given by [3.44]

$$V_{sh} \approx \left(\frac{\gamma+1}{2}\right) V \qquad (3.5)$$

$$T_{sh} \approx \frac{2\gamma}{\gamma+1}\left[\frac{(\gamma-1)}{(\gamma+1)}M^2+1\right]T_0 \tag{3.6}$$

$$\rho_{sh} = \rho_0\left(\frac{\gamma+1}{\gamma-1}\right) \tag{3.7}$$

where V is the velocity of the growing plume front which is determined by using the position-time plot, M is called the Mach number which is determined as follow: $M = \frac{V}{a}$, a is the sound speed, T_0 is the temperature of the background gas and ρ_0 is the gas density at standard temperature and pressure. The plasma plume parameters (P_1, V_1, ρ_1) can be calculated using conservation of mass, energy and momentum laws together with unperturbed gas known parameters [3.45].

$$P_1 = \frac{2\rho_0 V^2}{(1+\gamma_1)} \tag{3.8}$$

$$T_1 = \frac{P_1}{(R\rho_1)} \tag{3.9}$$

The plume growth into a buffer gas has been described using point-blast-wave equations [3.42]. The relationship between the position of the shock front, R, and the time t is exhibited as [3.46], according to the point-blast-wave:

$$R(t) = \left(\frac{\alpha E}{\rho_g}\right)^{\frac{1}{(n+2)}} t^{\frac{2}{(n+2)}}, \tag{3.10}$$

where E is the freed energy from the explosion and ρ_g is the buffer gas density, while $n = 1,2,3$ and $\alpha = 1.845, 1.015 \,\&1.175$ for plane-wave, cylindrical- and spherical-propagation, respectively.

Originally, the shock-wave creation energy through collision with the buffer gas is supplied by the ablated particles, which eventually result in plume thermalization. The shock-wave propagation rise to almost hemispherical behaviour when the distribution of the particle energy develops more isotropic as observed in number of PLD experiments [3.46]. The above equation can be written in terms of the emancipated energy, E, of the blast-wave from the explosion in the event of hemispherical expansion where E can be taken to be equivalent to the double hemispherically growing plume energy E_P, and the buffer gas pressures P_g [3.42, 3.46], as

$$R(t) = \xi \left(\frac{E_P}{P_g}\right)^{\frac{1}{2}} \left(c_g t\right)^{\frac{2}{5}} \tag{3.11}$$

where ξ is a dimensionless constant, which for $\gamma = \frac{5}{3}$ assumes a value of ≈ 1 , and c_g is the speed of sound in the undisturbed buffer gas. This model is restricted between the two extremes given by [3.46]

$$\left(\frac{3M_0}{2\pi\rho_0}\right)^{\frac{1}{3}} \ll R \gg \left(\frac{E}{\rho_0}\right)^{\frac{1}{3}} \tag{3.12}$$

where M_0 is initial explosion mass. Equation (3.12) can be expressed as

$$R = at^n \tag{3.13}$$

where a is a constant, n is an exponent and has a typical value of 0.4 which is applicable for an ideal shock condition and assumes a value of 1 for a free-expansion of the plasma plume.

3.7 Classical Drag Model

The experiments conducted on the plasma plume propagation concluded that the propagation will end at a finite distance. And these distances and the corresponding stopping times can be described by employing the so called “classical drag force model” [3.47]. The released pulse of ablation products in a classical drag model is considered as an assemblage that encounters a viscous force which is proportional to its velocity through the surrounding gas. The plasma plume progressively slows down in a drag model and ultimately comes to the end because of the drag force. The plume length or stopping distance is defined as the distance in mm from the target at which the plume spread ends [3.48]. The buffer gas pressure is equal to the plasma plume pressure at this said “plume length”. The plasma plume front expansion is derived as follows: The motion equation is $a = -\beta v$, giving

$$v = v_0 e^{-\beta t} = v_0 - \beta x \quad (3.14)$$

$$x = x_f \left[1 - e^{-\beta t}\right] \quad (3.15)$$

where the slowing coefficient is β and $x_f = \frac{v_0}{\beta}$ is the plume stopping distance.

3.8 Plume-Substrate Interaction

In PLD, the attachment of the plume species onto the substrate for film growth happens instantaneously. This is because the atomistic processes happen at much smaller time scale than the plume pulse duration [3.48]. A relatively long time interval occurs after each instantaneous deposition where no deposition takes place. After deposition, which happens instantaneously, there is a second process, called nucleation, which takes place

on the substrate. Nucleation is random and is observed to happen after the plume pulse duration. The instantaneous deposition rate is controlled using these parameters; laser energy density at the target, the target-substrate distance and surrounding gas pressure [3.49].

3.9 Thin Film Growth

PLD has been successfully used to grow several materials including transparent dielectrics, semiconductors, metals, and superconductors [3.50]. PLD is favoured when compared to other synthesis methods. This is because of the nature of the pulsed laser (as one can count and choose the exact number of pulses), the probability of carrying out surface reactions when the surface is not in thermal equilibrium and in chosen suitable conditions or parameter, the capability to replicate thin layers with repeatable elemental ratios. Willmott *et al.* [3.51] stated that although there is a variety of kinetic energies of the hitting species for which surface mobility and reactivity are improved, the bulk of the substrate remains unchanged. Generally this lies at about 50 eV and this calculation is based on the bond strengths. The kinetic energies of neutral species in ablation plume are lower than the bulk damage threshold energies. Furthermore, if required, it is possible to tune the energy of the ion to fit a particular purpose/experiment by biasing the substrate potential.

It is possible to modify the film growth and chemistry in PLD by being deposited in the buffer gas. The purpose of the buffer gas in PLD is either to make plasma species hotter than vacuum condition through various collisions or to make ablation amounts

congruent at the target [3.52]. H_2, CH_4, N_2 and O_2 are typical gases used in PLD to develop reactions mostly with metal elements, to synthesize either oxides, nitrides, carbides or hydrides [3.53]. In PLD, compound targets are often obtainable, mostly in the deposition of ceramic and dielectric films and including multi-elemental nitrides, carbides and oxides. This is one of the PLD advantages over other synthesis approaches, and has been often used in ceramic superconductors thin film growth. The purity of the target material is hardly better than 1 in 10 000. [3.54].

The combination of the deposition process is considered to be diffusion and an ad-atom adsorption on the surface [3.55, 3.56]. Adsorption of plume species on the substrate happen at very low energies of the order fractions of eV without bonding whereas chemisorption takes place when the species make chemical bonds with surface. The chemisorption energies range from 3 to 5 eV [3.57]. Diffusion can be due to either concentration or thermal gradients. In the case of high energy PLD, thermal diffusion is most prevalent. Factors as the activation of the substrate, temperature, the presence of other competing species, the nature of the adsorbate, surface roughness, and defect concentration affect the adsorption and diffusion processes [3.58].

3.10 PLD for VO_2 Thin Films

Borek *et al.* [3.59] was the first to use PLD to deposit VO_2. They annealed the so-deposited thin layer for 1 hour in the same temperature and pressure that was used for deposition to obtain VO_2 (M1) films which have the MIT property. Shortly after that, several studies were done to synthesized VO_2 and V_xO_y using PLD [3.60]. However often

the so-obtained VO_x and V_xO_y thin layers were later annealed in various gas environments such as air, O_2, Ar or N in order to alter or improve the VO_2 phase. VO_2 has been deposited on various substrates (including glass, silicon, quartz and sapphire) by using various targets including V, VO_2, V_2O_3 and V_2O_5. A variety of nano-structures of VO_2 have been produced including nano-particles [3.61], nano-belts [3.62], and nano-rods [3.63] among others.

The majority of reports on VO_2 (M1) nano-particle deposition using PLD could only be synthesized after post-annealing [3.64]. The first report of room-temperature growth of VO_2 by PLD without post-annealing is Maaza *et al.* [3.65] and the deposited films showed rather sharp phase transitions at around 70 °C, even though it has not been reproduced by any other group yet. Kim *et al.* [3.66] have also reported the deposition of high quality VO_2 films on sapphire by PLD at high temperatures without post-annealing. Suh *et al.* [3.67] discussed the influence of nucleation, and growth of VO_2 nano-particles that were grown by PLD. They found that at higher temperatures, there was a significant proportion of V_2O_5 and VO_2 obtained by post-deposition annealing at 550 °C.

It is now well-known that the VO_2 transition temperature can also be decreased by doping with tungsten or other elements, such as Nb, Mo, F and Ta in the proper amount [3.68]. Ye *et al.* [3.69] synthesized a thermochromic tungsten-doped VO_2 powders by thermal reduction using V_2O_5 as a vanadium precursor. They successfully reduced the transition temperature from an initial 69.5 °C to 37.8 °C, proposing that tungsten-doped VO_2 possesses prominent optical switching and thermochromic properties characters. Hanlon *et al.* [3.70] deposited molybdenum-doped VO_2 coating on a glass

substrate by the aqueous sol-gel method. Doping the VO_2 layers with molybdenum lowered the transition temperature to 24 °C.

A study of the literature shows that, there are no studies that have been shown to reduce the VO_2 transition temperature without doping. Muraoka and Hiroi [3.71, 3.72] have grown VO_2 on TiO_2 (001) and (110) substrates by PLD. They measured a large decrement in the MIT temperature: decreasing from 341 K for a single crystal to 300 K for the film on TiO_2 (001) orientated substrate. In this case the decrease in the MIT could be attributed to the compression of the c-axis length in the TiO_2 (001) oriented substrate. For TiO_2 substrate oriented in (110) plane the MIT increases to 369 K due to expansion of the c-axis length**.** This suggested that the shortened c-axis length results in the lower transition temperature.

On the other hand Case *et al.* [3.73] and Jin *et al.* [3.74] successfully reduced the VO_2 transition temperature to 318 K by growing on Al_2O_3 (0001) substrates by reactively sputtering. Li *et al.* [3.75] deposited VO_2 on fused silica and silicon substrates by employing reactive ion sputtering in addition to post-deposition annealing. They measured the transition temperature to be near 35 °C. This is 33 °C downshift from the bulk VO_2 MIT of 68 °C.

3.11 Summary

In this chapter the principles of the pulsed laser induced plasma, the role the plasma plume dynamics play in PLD and the quality of thin films have been discussed.

References

3.1 D. Dijkkamp, T. Ventatesan, X.D. Wu, S.A. Shaheen, N. Jisrawi, Y.H. Minlee, W.L. McLean, M. Croft, "Preparation of Y-Ba-Cu oxide superconductor thin films using pulsed laser evaporation from high Tc bulk material", Appl. Phys. Lett. **51**, 619 (**1987**).

3.2 J. Nag, R.F. Haglund Jr, "Synthesis of vanadium dioxide thin films and nanoparticles", J. Phys.: Condens. Matter **20**, 264016 (**2008**).

3.3 J.R. Ho, C.P. Grigoropoulos, J.A.C. Humphrey, "Gas dynamics and radiation heat transfer in the vapour plume produced by pulsed laser irradiation of aluminium", J. Appl. Phys. **79** (9), 7205 (**1996**).

3.4 F. Hamadi, E.H. Amara, T. Kerdja, D. Mezaoui, "Numerical modelling of aluminium vapour produced by nanosecond UV laser beam ablation", Phys. Stat. sol. (c) **5** (10), 3314 (**2008**).

3.5 H.C. Le, D.E. Zeitioun, J.D. Parisse, M. Sentis, W. Marine, "Modeling of gas dynamics for a laser-generated plasma: Propagation into low-pressure gas", Phys. Rev. E **62** (3), 4152 (**2000**).

3.6 L.J. Radziemski, D.A. Cremers (Eds), "Laser-induced plasma and applications", Marcel Dekker, New York (**1989**).

3.7 P.R. Wilmott, J.R. Huber, "Pulsed laser vaporization and deposition", Rev. Mod. Phys. **72**, 315 (**2000**).

3.8 A. De Giacomo, V.A. Shakhatov, G.S. Senesi, F. Prudenzano, "Plasma assisted pulsed laser deposition for the improvement of thin film growth", Appl. Surf. Sci. **186**, 533 (**2002**).

3.9 R.S. Adrain, J. Waston, "Laser microscpectral analysis: a review of principles and applications", J. Phys. D: Appl. Phys. **17**, 1915 (**1984**).

3.10 D.B. Geohegan, "in Pulsed laser deposition of thin films", Edited by DB Chrisey and GK Hubler, Wiley, New York, **115** (**1994**).

3.11 S. Amoruso, R. Bruzzese, N. Spinelle, R. Velotta, "Chacterization of laser-ablation plasmas", J. Phys. B: At. Mol. Opt. Phys. **32**, R 131 (**1999**).

3.12 D.B. Geohegan, A.A. Puretzky, "Dynamics of laser ablation plume penetration through low pressure background gases", Appl. Phys. Lett. **67**, 197 (**1995**).

3.13 A. De Giacomo, M. Dell'Aglio, R. Gaudiuso, S. Amoruso, O. De Pascale. "Effects of the background environment on formation, evolution and emission spectra of laser-induced plasmas", Spectrochimica Acta Part B **78**, 1 (**2012**).

3.14 A. Miotello, R. Kelly, "Laser-induced phase explosion: new physical problems when a condensed phase approaches the thermodynamics critical temperature", Appl. Phys. A **69**, S67 (Suppl) (**1999**).

3.15 R.F. Wood, G.E. Giles, "Macroscopic theory of pulsed-laser annealing. I. Thermal transport and melting", Phys. Rev. B **23** (6), 2923 (**1981**).

3.16 R.K. Singh, J. Narayan, "A novel method for simulating laser-solid interactions in semiconductors and layers structures", Mater. Sci. Eng. B **3** (3), 217 (**1989**).

3.17 J.F. Ready, "Effects of high-power laser radiation", New York:Academic, (**1971**).

3.18 B.N. Chichcov, C. Momma, S. Nolte, F. von Alvensleben, A Tunnermann, "Femtosecond, picosecond and nanosecond laser ablation of solids", Appl. Phys. A **63**, 109 (**1996**).

3.19 S. Fahler, H.U. Krebs, "Calculations and experiments of material removal and kinetic-energy during pulsed-laser ablation of metals", Appl. Surf. Sci. **96-8**, 61 (**1996**).

3.20 R. Timm, P.R. Willmott, J.R. Huber, "Ablation and blow-off characteristics at 248 nm of Al, Sn and Ti targets used for thin film pulsed laser deposition", J. Appl. Phys. **80** (3), 1794 (**1996**).

3.21 S. Amoruso, V. Berardi, R. Buzzese, N. Spinelli, X. Wang, "Kinetic energy distribution of ions in the laser ablation of copper targets", Appl. Surf. Sci **127-129**, 953 (**1998**).

3.22 R.M. Gilgenbach, P.L.G. Ventzeck, "Dynamics of excimer laser-ablated aluminium neutral atom plume measured by dye laser resonance absorption photography", Appl. Phys. Lett. **58** (15), 1597 (**1991**).

3.23 S.S. Hiralal, G.V. Mioshevsky, P.K. Diwakar, N.L. LaHaye, A. Hassanein, "Experimental and computational study of complex shockwave dynamics in laser ablation plumes in argon atmosphere", Phys. Plasmas **19**, 083504 (**2012**).

3.24 J.N. Leboeuf, K.R. Chen, J.M. Donato, D.B. Geohegan, C.L. Liu, A.A. Puretzky, "Modeling of dynamical processes in laser ablation", Appl. Sur. Sci. **96-98**, 14 (**1996**).

3.25 R.W. Dreyfus, "Interpreting laser ablation using cross sections", Surf. Sci. **283**, 177 (**1993**).

3.26 T.P. Hughes, "Plasma and Laser Light", Wiley, New York, (**1795**).

3.27 S.S. Harilal, B. O'Shay, Y. Tao, M.S. Tillack, "Ambient gas effects on the dynamics of laser-produced tin plume expansion", J. Appl. Phys. **99** (8), 083303 (**2006**).

3.28 K.F. Al-Shboul, S.S. Harilal, A. Hassanein, "Gas dynamics effects on formation of carbon dimers in laser-produced plasmas", Appl. Phys. Lett. **99** (13), 131506 (**2011**).

3.29 S.S. Harilal, "Influence of spot size on propagation dynamics of laser-produced tin plasma", J. Appl. Phys. **102**, 123306 (**2007**).

3.30 S. Amoruso, B. Toftmann, J. Schou, R. Velotta, X. Wang, "Diagnostics of laser ablated plasma plumes", Thin Solid Films **453-454**, 562 (**2004**).

3.31 A. De Giacomo, R. Gaudiuso, M. Dell'Aglio, A. Santagata, "The role of continuum radiation in laser induced plasma spectroscopy", Spectrochim. Acta Part B **65**, 385 (**2010**).

3.32 N. Arnold, J. Gruber, J. Heirtz, "Spherical expansion of the vapour plume into ambient gas: an analytical model", Appl. Phys. A **69** (1), S87 (**1999**).

3.33 S. Wen, X. Mao, R. Grief, R.E. Russo, "Laser ablation induced vapour plume expansion into a background gas. II. Experimental analysis", J. Appl. Phys. **101**, 023115 (**2007**).

3.34 A. Bogaerts, Z. Chen, "Effect of laser parameters on laser ablation and laser-induced plasma formation: a numerical modelling investigation", Spectrochim. Acta Part B **60**, 1280 (**2005**).

3.35 R. Kelly, A. Miotello, "Comments on explosive mechanisms of laser sputtering", Appl. Surf. Sci. **96-98**, 205 (**1996**).

3.36 D. Sibold, H.M. Urbassek, "Kinetic study of pulsed desorption flows into vacuum", Phys. Rev. A **43** (12), 6722 (**1991**).

3.37 S.S. Harilal, "Expansion dynamics of laser ablated carbon plasma plume in helium ambient", Appl. Surf. Sci. **172**, 103 (**2001).**

3.38 S.S. Harilal, C.V. Bindhu, V.P.N. Nampoori, C.P.G. Vallabhan, "Influence of ambient gas on the temperature and density of laser produced carbon plasma", Appl. Phys. Lett. **72** (2), 167 (**1998**).

3.39 S. Amuroso, C. Aruta, R. Bruzzese, D. Maccariello, L. Maritato, F. Miletto Granozio, P. Orgiani, U. Scotti di Uccio, X. Wang, "Optimization of La0.7Ba0.3MnO3-δ complex

oxide laser ablation conditions by plume imaging and optical emission spectroscopy", J. Appl. Phys. **108**, 043302 (**2010**).

3.40 T.E. Itina, J. Hermann, P. Delaporte, M. Sentis, "Laser-generated plasma plume expansion: combined continuous-microscopic modelling", Phys. Rev. E Stat. Nonlin. Soft Matter Phys. **66** (6 pt 2), 066406 (**2002**).

3.41 K.R. Chen, J.N. Leboeuf, R.F. Wood, D.B. Geohegan, J.M. Donato, C.L. Liu, A.A. Puretzky, "Laser-Solid interaction and dynamics of laser-ablated materials", Appl. Surf. Sci. 96-98, 45 (**1996**).

3.42 Ya. B. Zel'dovich, Yu. P. Raizer, "in Physics of schock waves and high temperature hydrodynamic phenomena", Academic Press, New York **1**, 94 (**1966**).

3.43 D.B. Geohegan, in E. Fogarassy and S. Lazare (eds), "Laser ablation of electronic materials: Basic mechanisms and applications", Elsevier, Amsterdam, 73 (**1992**).

3.44 A. Misra, A. Mitra, R.K. Thareja, "Diagnostics of laser ablated plasmas using fast photography", Appl. Phys. Lett. **74** (1), 929 (**1999**).

3.45 M. Ohkoshi, T. Yoshitake, K. Tsushima, "Dynamics of laser-ablated iron in nitrogen atmosphere", Appl. Phys. Lett. **64** (24), 3340 (**1994**).

3.46 D.B. Geohegan, "Physics and diagnostic of laser ablation plume propagation for high-Tc superconductor film growth", Thin Solid Film **220**, 138 (**1992**).

3.47 V. Berardi, S. Amoruso, N. Spinelli, M. Armenante, R. Velottaa, F. Fuso, M. Allegrini, E. Arimonodo, "Diagnostics of $YBa_2CuO_{7-\sigma}$ lase rplume by time-of-flight mass spectrometry". J. Appl. Phys. **76** (12), 8077 (**1994**).

3.48 A.J.H.M. Rijnders, "The initial growth of complex oxides: study and manipulation", PhD Thesis, Univerisity of Twente, The Netherlands (**2001**).

3.49 M. Huijben, "Tuning electronics properties by atomically controlled growth", PhD Thesis, Univerisity of Twenter, The Netherlands (**2006**).

3.50 K.L. Saenger, "in Pulsed Laser Deposition of Thin films", edited by D.B. Chrisey and G.K. Hubler (Wiley, New York), 581 (**1994**).

3.51 P.R. Willmott, R. Timm, P. Felder, J.R. Huber, "Growth of CUO films by pulsed-laser deposition in conjuction with a pulsed oxidation source",J. Appl. Phys. **76** (5), 2657 (**1994**).

3.52 A. Gupta, B.W. Hussey, "Laser deposition of $YBa_2Cu_3O_{7-\delta}$ films using a pulsed oxygen source", Appl. Phys. Lett. **58**, 1211 (**1991**).

3.53 R.F. Xiao, H.B. Liao, N. Cue, X.W. Sun, H.S. Kwok, "Growth of c-axis oriented gallium nitride thin films on an armorphous substrate by the liquid-target pulsed laser deposition technique", J. Appl. Phys. **80**, 4226 (**1996**).

3.54 P. Verardi, M. Dinescu, F. Cracium, A. Perrone, "In situ growth of ferroelectric lead zirconate-titanate thin films on Si substrates by pulsed Nd: YAG laser deposition", Appl. Surf. Sci. **127-129**, 457 (**1998**).

3.55 M. Tyunina, J. Levoska, S. Leppävuori, "Sorption in pulsed laser deposition of multicomponent materials: experiment versus modelling", J. Appl. Phys. **86** (5), 2901 (**1999**).

3.56 D. Srivastava, B.J. Garrison, "Adsorption and diffusion dynamics of a Ge adatom on the Si{100} (2x1) surface", Phys. Rev. B **46**, 1472 (**1992**).

3.57 F.O. Goodman, H.Y. Wachman, "Dynamics of gas-surface scattering", Academic, New York, **1976**.

3.58 "Kinetic of ordering and growth at surfaces", edited by M.G. Lagally, Nato ASI Ser., Ser. B **939**, Plenum, New York (**1990**).

3.59 M. Borek, F. Qian, V. Nagabushnam, R.K. Singh, "Pulsed laser deposition of oriented VO_2 thin films on R-cut sapphire substrate", Appl. Phys. Lett. **63**, 3288 (**1993**).

3.60 J. Nag, R.F. Haglund Jr, "Synthesis of vanadium dioxide thin films and nanoparticles", J. Phys.: Condens Matter **20**, 264016 (**2008**).

3.61 D. Fu, K. Liu, T. Tao, K. Lo, C. Cheng, B. Liu, R. Zhang, H.A. Bechtel, H. Wu, "Comprehensive study of the metal-insulator transition in pulsed laser deposited epitaxial VO_2 thin films", J. Appl. Phys. **113**, 043707 (**2013**).

3.62 Y. Zhang, J. Zhang, X. Zhang, S. Mo, W. Wu, F. Niu, Y. Zhong, X. Liu, C. Huang, X. Liu, "Direct preparation and formation mechanism of belt-like doped VO2 (M) with rectangular cross sections by one-step hydrothermal route and their phase transition and optical switching properties" J. Alloys and Compounds **570**, 104 (**2013**).

3.63 S. Ji, Y. Zhao, F. Zhang, P. Jin, "Direct formation of single crystal VO_2 (R) nano-rods by one-step hydrothermal treatment", J. Crystal Growth **312**, 282 (**2010**).

3.64 R. Lopez, L.A. Boatner, T.E. Haynes, R.F. Haglund Jr., L.C. Feldman, "Optical nonlinearities in VO_2 nano-particles and thin films", Appl. Phys. Lett. **85**, 5191 (**2004**).

3.65 M. Maaza, K. Bouziane, J. Maritz, D.S. McLachlan, R. Swanepool, J.M. Frigerio, M. Every, "Direct production of thermochromic VO_2 thin film coatings by pulsed laser ablation" Opt. Mater. **15**, 41 (**2000).**

3.66 D.H. Kim, H.S. Kwok, "Pulsed laser deposition of VO_2 thin films", Appl. Phys. Lett. **65**, 3188 (**1994**).

3.67 J.Y. Suh, R. Lopez, L.C. Feldman, R.F. Haglund Jr, "Semiconductor to metal phase transition in the nucleation and growth of VO_2 nanoparticles and thin films", J. Appl. Phys. **96** (2), 1209 (**2004**).

3.68 S. Lu, L. Hou, F. Gan, "Surface analysis and phase transition of gel-derived VO_2 thin films", Thin Solid Films **353**, 40 (**1999**).

3.69 J. Ye, L. Zhou, F. Liu, J. Qi, W. Gong, Y. Lin, G. Ning, “Preparation, characterization and properties of thermochormic tungsten-doped vanadium dioxide by thermal reduction and annealing”, J. Alloys and Compounds **504**, 503 (**2010**).

3.70 T.J. Hanlon, J.A. Coath, M.A. Richardson, “Molybdenum-doped vanadium dioxide coatings on glass produced by the aqueous sol-gel method”, Thin Solid Films **436**, 269 (**2003**).

3.71 Y. Muraoka, Z. Hiroi, “Metal-insulator transition of VO_2 thin films grown on TiO_2 (001) and (110) substrates”, Appl. Phys. Lett. **80** (40), 583 (**2002**).

3.72 Y. Muraoka, Y. Ueda, Z. Hiroi, “Large modification of the metal-insulator transition temperature in strained VO_2 films grown on TiO_2 substrates”, J. Phys. Chem. Of Solids **63**, 965 (**2002**).

3.73 F.C. Case, “The influence of substrate temperature on the optical properties on ion-assisted reactively evaporated vanadium oxide thin films”, J. Vac. Sci. Technol. A **6**, 2010 (**1988**).

3.74 P. Jin, K. Yoshimura, S. Tamura, “Dependence of microstructure and thermochromism on substrate temperature for sputter-deposited VO_2 epitaxial films”, J. Vac. Sci. Technol. A **15**, 1113 (**1997**).

3.75 Y. Li, X. Yi, T. Zhang, “Nanostructure and thermal-optical properties of vanadium dioxide thin films”, Chinese Opt. Lett. **3** (12), 719 (**2005**).

Chapter 4

Investigation of Vanadium Dioxide (VO_2) Plasma Plume Dynamics

In the pulsed laser deposition (PLD) process, it is important to control the plume dynamics in order to obtain good quality and correct stoichiometric thin films or nano-structures. An energetic laser pulse is used to heat and vaporize the material of interest under vacuum or in background gas at low and controlled gas partial pressures. In this process, the plasma formed by the leading edge of the laser pulse will be heated efficiently by the rest of the laser pulse. In the nano-second-long pulse laser ablation, the plasma expands isothermally during the laser pulse followed by adiabatic expansion after the laser pulse termination [4.1, 4.2]. During the isothermal regime, initially, the laser interacts with the target and a low temperature plasma plume is formed; collisional ionization and excitation coupled with the remainder of the laser pulse energy then rapidly heats and ionizes the plasma. A gaseous atmosphere is always used as a moderator to the energetic particles in the PLD process [4.3]. The presence of the gas influences the entire processes of plasma generation as well as expansion, and leads to the formation of internal plume structures, plume splitting, sharpening, confinement, and, in contrast, to free expanding plume experienced in a vacuum.

In this chapter, we investigate the plasma formation and expansion mechanisms during the PLD process of vanadium oxide film deposition, since the source of the films is a laser generated plasma composed of neutral and ionized atoms, molecules, and other species. Several studies [4.1, 4.3, 4.4] have shown that plasma plume dynamics strongly influence the properties of thin films deposited by PLD. They also show that the plasma plume expansion process depends on laser intensity, pulse duration, wavelength of the

laser, target material and geometry, as well as the nature and pressure of the background gas. The plasma plume characteristics also vary with distance from the target surface as well as with time following the onset of plume formation.

Despite all the research already published, there have been few reports on the plasma plume dynamics of vaporized VO_2 target. Lafane *et al.* [4.5] studied the correlation of plume dynamics and oxygen pressure with VO_2 stoichiometry during PLD by ablating a vanadium pentoxide (V_2O_5) target. They highlighted the effect of the plume dynamics on the properties of the obtained vanadium oxide thin films and found that the splitting into two components of the plume and a slowdown of the plume appear, coinciding with the appearance of the pure VO_2 phase in the deposited films at a pressure of 4×10^{-3} mbar. Here we show that the plasma plume initially expands at the same rate regardless of the oxygen pressure and then later deviates from this trend as it slows down. The point of transition from one expansion regime to the next varies depending on the oxygen pressure.

4.1 Experimental Set-up

Figure 4.1 depicts the experimental setup which was used in this study to carry out the study of the plume expansion dynamics of ablation of VO_2 [4.6]. During the experiments, the vacuum chamber was initially evacuated to a base pressure of 10^{-5} mbar before oxygen was introduced. The overall emission of the bright expanding plasma was recorded by means of fast intensified charge coupled device (ICCD) camera, from the start of the target-laser ablation event, up to the arrival of the ablated species onto the substrate. Two cylindrical lenses are used to focus the KrF (λ = 248 nm, τ = 25 ns) laser

beam on the rotating target with an incident angle of 45°. The target was a VO_2 pellet of diameter 25 mm and thickness of 10 mm purchased from Sigma-Aldrich Company (manufacturer). A set of spherical, plane mirrors and a Zeiss lens (76 mm focal length, spectral range: 350 – 800 nm) were used to image the two-dimensional luminous plasma on the ICCD camera (Princeton Instruments PI-MAX as given in Figure 4.1, 1024 x 256 pixel size = 26 x 26 μm) with a magnification of 1/3. The temporal resolution of the ICCD camera is 5 ns and its spectral response is within the range of 190 – 850 nm. The plasma plume study was carried out at vacuum and at a range of oxygen gas pressures (0.001-0.20 mbar). The pulsed energy was fixed at 120 mJ which gives a laser fluence of 2 J.cm^{-2}. The number of accumulation, ICCD gain and gate were adjusted for each image to compensate for the reduction of the plume intensity during the expansion.

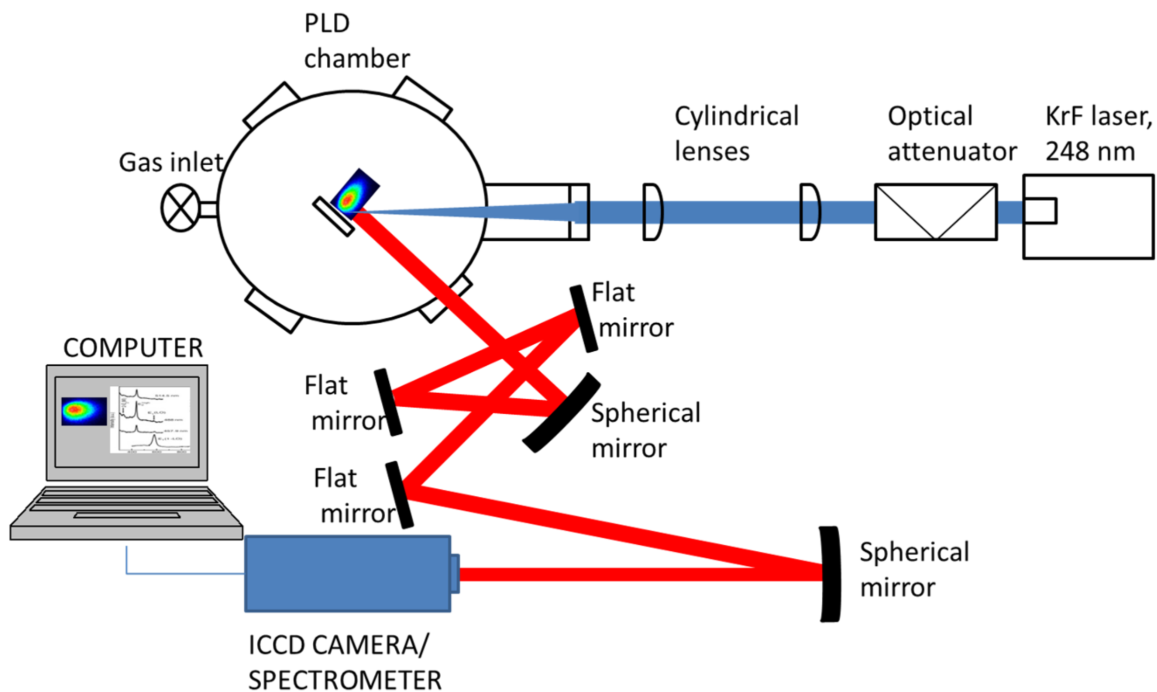

Figure 4.1: Schematic diagram of the experimental set-up which was used to establish the VO_2 plume dynamics in this study [4.6].

4.2 Results and Discussion

A. Influence of Ambient Gas on Plasma Plume Dynamics

In order to better understand the role that the pressure of the background gas plays on the structural and morphological properties of the deposited thin films, we have studied the plasma plume dynamics of V-O produced by laser ablation. 2D images of visible V-O plasma plume emission under various oxygen pressures were captured by an ICCD camera at regular time intervals starting from the beginning of the laser-target interaction as given in Figures 4.2 (a) and 4.2 (b). Each 2D image represents the spectrally-integrated emission in the range of 400 – 800 nm that is due to emission from the excited states of various species and they are not representative of the total flux of particles due to that part of the plasma plume, which is nonluminous. At vacuum and low pressures $<10^{-2}$ mbar, the plasma plume expands freely without any external viscous force. The images show that in the earlier time the expansion is mono-dimensional in the normal direction to the target and after a few hundred of nano-seconds the pressure gradients equilibrate and the plasma plume extends in the directions to the substrate.

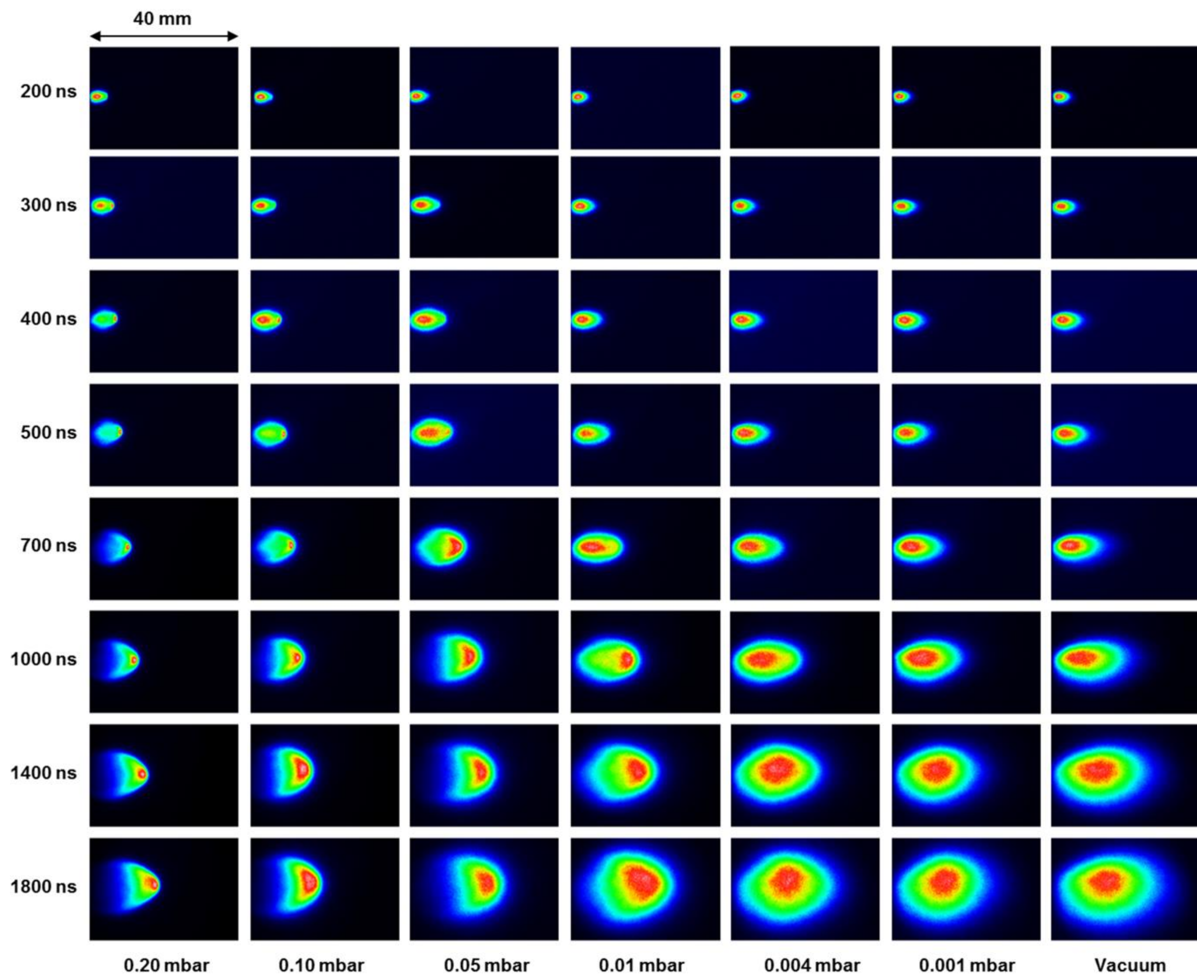

Figure 4.2 (a): The temporal evolution of the visible spectra range of the plasma at various oxygen pressures after laser to VO_2 target interaction.

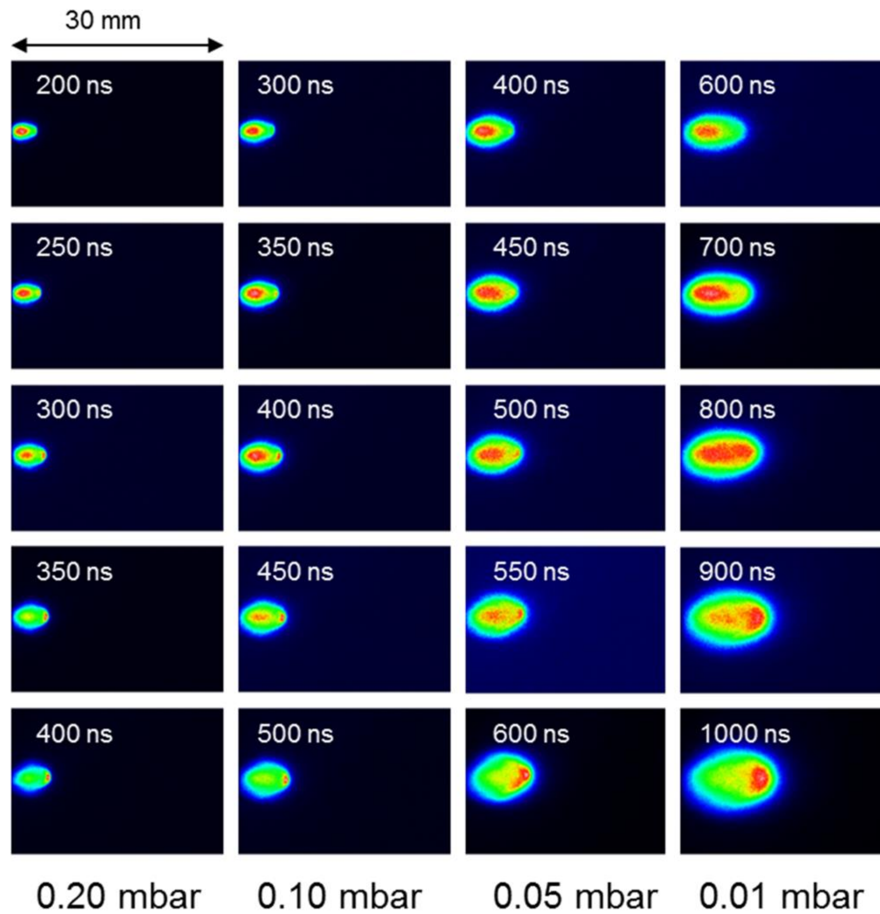

Figure 4.2 (b): The temporal evolution of the visible spectral range of the plasma plume at various oxygen pressures after the laser-to-VO_2 target interaction (expanded time-scale).

The effect of background gas on the expansion dynamics becomes noticeable at 0.01 mbar pressure, resulting in the observation of plume splitting and enhancement of emission intensity. For oxygen pressures ≤0.004 mbar the plume appears to experienced free expansion. There is no plume-to-oxygen gas boundary, as is evident in Figure 4.2 (a). However, in the oxygen pressure ranges of 0.01 mbar to 0.20 mbar, the plume is confined and splits into two components. The confinement and splitting of the plume varies, depending on the time delays and the oxygen pressure as shown in Figure 4.2 (b).

Several authors [4.6, 4.7, 4.8, 4.9] have observed the plume splitting and have different opinions on its origins. Wood *et al.* [4.9] discussed this phenomenon based on the combination of multiple elastic scattering and hydrodynamic formulations. The splitting of the plasma plume into two components indicates the interaction between the plume species which are scattered in a backward direction after collisions with background gas molecules and the incoming particles [4.10]. The results of this interaction are the formation of a shock front and enhancement of the plume luminosity at the plume-to-oxygen edge. Highly reactive atomic oxygen is produced in the shocked layer and oxygen enrichment in the deposited films is expected. A shock wave may develop if the mass of the ablated material is lower than the mass of the surrounding background gas the plasma plume had set in motion, and if the pressure driving the moving front of the plasma plume is greater than the pressure of the background gas at rest [4.11]. The development of the shock wave is indicated by the appearance of a visible edge at the contact front between the plasma and the surrounding gas. As the plasma propagates, we observed a visible edge of the plume as shown in Figure 4.2 (b). Several authors reported on this visible plasma edge and they suggested that the visible plume edge implies that high kinetic energy particles are emitted closer to the target surface normal [4.11, 4.12]. And also, it was attributed to the deceleration of a part of the plasma plume due to the interaction with background gas or due to the formation of molecular species as reported by Kushwaha *et al.* [4.13].

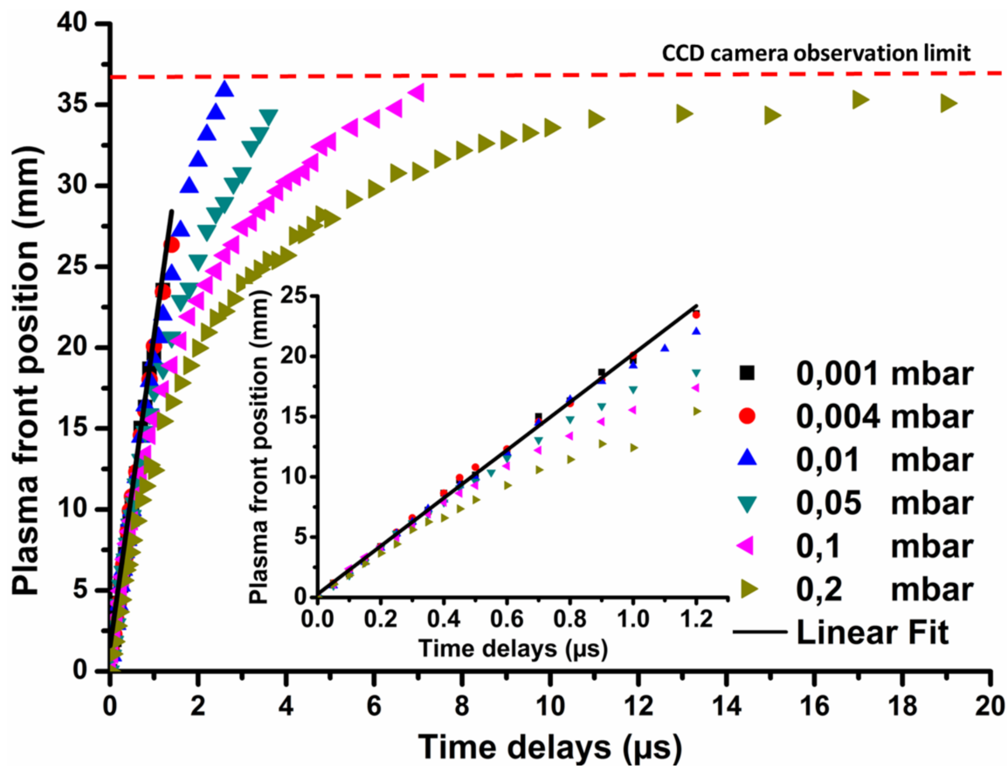

Figure 4.3: Propagation of plasma plume front position for different oxygen pressure. The inserted graph shows the linear early expansion region.

The propagation of the plasma front position as function of time and oxygen pressure is shown in Figure 4.3. We observed that the plasma plume expands at the same initial rate at various oxygen pressures (see insert graph in Figure 4.3). At oxygen pressures <0.2 mbar, the expansion initially remains linear (free-plume emission expansion) and then becomes non-linear by expanding at a decreasing rate as time increases until the expansion remains nearly constant. With the non-linear regime, one can speculate that the ejected species collide with the oxygen gas molecules and lose their kinetic energy and later the plume expansion stops completely. The ejected species diffuse into the surrounding oxygen environment until they reach a distance where they lose their kinetic energy. At 0.1 and 0.2 mbar oxygen pressure, the plasma plume expansion

dynamics passes from free-like to shock-like and finally reaches a stopping time and distance as indicated in Figure 4.3. We observed deviations from linear expansion for oxygen pressures <0.004 mbar. The point of transition from one expansion regime to the next varies depending on the ambient gas pressure.

B. Classical Drag Model

The classical drag model predicts that the plume progressively slows down and eventually comes to rest due to the resistance from collisions with the background gas. In a classical drag force model (as discussed in Chapter 3, section 3.5), the ejected pulse of ablation products is regarded as an ensemble which experiences a viscous force proportional to its velocity through the background gas. If, $x_f = \frac{v_0}{\beta}$ is the distance from the target at which the propagation ceases (so-called stopping distance) [4.11, 4.14], then the position of the plume front is given by

$$x = x_f\left[1 - e^{-\beta t}\right] \tag{4.1}$$

where β is the slowing coefficient and $v_0$is initially velocity. By differentiating equation (4.1) with respect to time, one can find the instantaneous velocity of the plume front which can be given as

$$\frac{dx}{dt} = v(t) = v_0 e^{-\beta t} \tag{4.2}$$

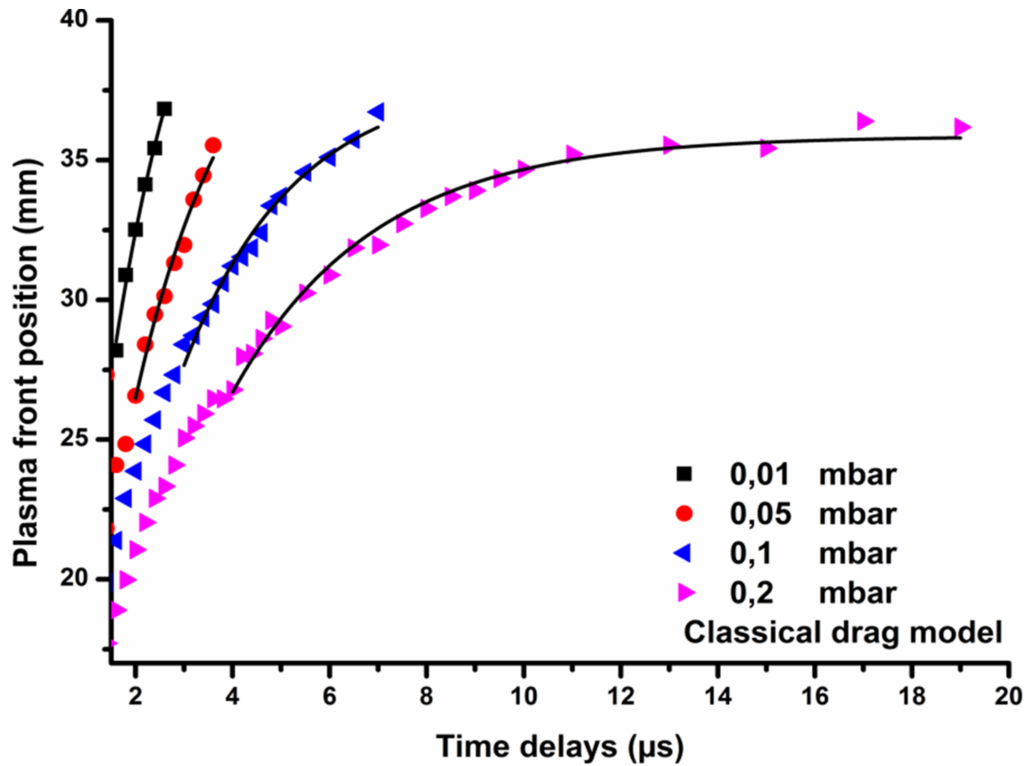

Figure 4.4: Propagation of plasma plume front position for different oxygen pressure fitting with the classic drag model which is indicated by black line.

We fitted the experimental data using the classical drag model equation given in equation (4.1) and then, by deriving the predicted plume emission species trajectory, the velocity and target-substrate distance were deduced. Figure 4.4 indicates the fit of the classical drag model equation to the experimentally data for different oxygen pressures. The classical drag model fit given in Figure 4.4 agrees well at later stages of the plume propagation data obtained from ICCD images. The classical drag model parameters values are shown in Table 4.1.

Table 4.1: Drag model parameter values for the plasma plume at different oxygen pressures.

Pressure (mbar)	Classical drag model		
	x_f (cm)	β (μs^{-1})	v_0(10^6cm/s)
0.2	3.6	2.93	10.5
0.1	3.8	2.31	8.8
0.05	4.2	2.03	8.6
0.01	4.8	1.76	8.4

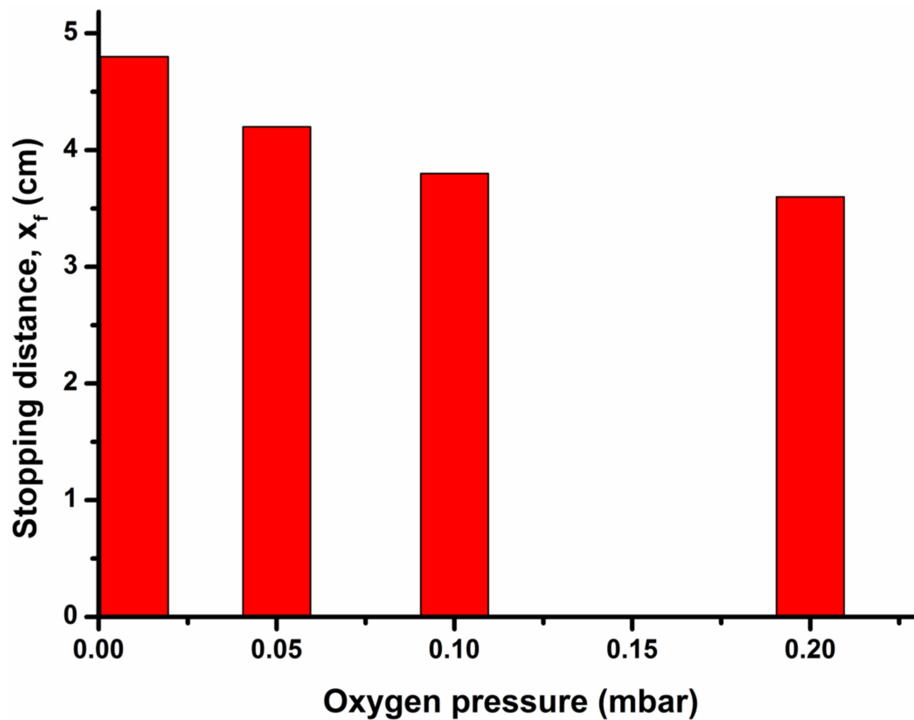

Figure 4.5: Plasma plume stopping distance for different oxygen pressure as indicated in Table 4.1.

One observes that the classical drag model predicts that the stopping distance decreases as the oxygen gas pressures increases as given in Table 4.1 and Figure 4.5. This is expected and could be due to the collisions between the plume species with the oxygen

gas molecules a phenomenon which further results in the increases in viscous force. Additionally, the decreasing of the stopping distance is attributed to a loss of kinetic energy of the ejected species due to collisions with the oxygen gas, until finally the process is driven by diffusion of the ejected species into the surrounding oxygen environment.

Ngom *et al.* [4.15] found that the initial velocity (v_0) is in the same order from vacuum (1.820 x 10^4 m/s) to 0.2 mbar (1.783 x 10^4 m/s). As they increased the pressure, the v_0 decreases from 0.3 mbar (1.65 x 10^4 m/s) to 0.8 mbar (1.39 x 10^4 m/s). They determined the v_0 by making use of the linear fit fitted to the plasma dynamics graph at early time and propagation. In this study by making use of the same approach, the v_0 was determined to be in the same order (2 x 10^6 cm/s) for pressures between 0.01 – 0.2 mbar which corresponds very well with the Ngom *et al.* [4.15] finding. Moreover, this also corresponds well with the linear expansion of the plasma plume observed at initial time and propagation regardless of oxygen pressures, as shown in Figure 4.3, which means that the ejected species are not affected by the oxygen pressure in the initial stage only.

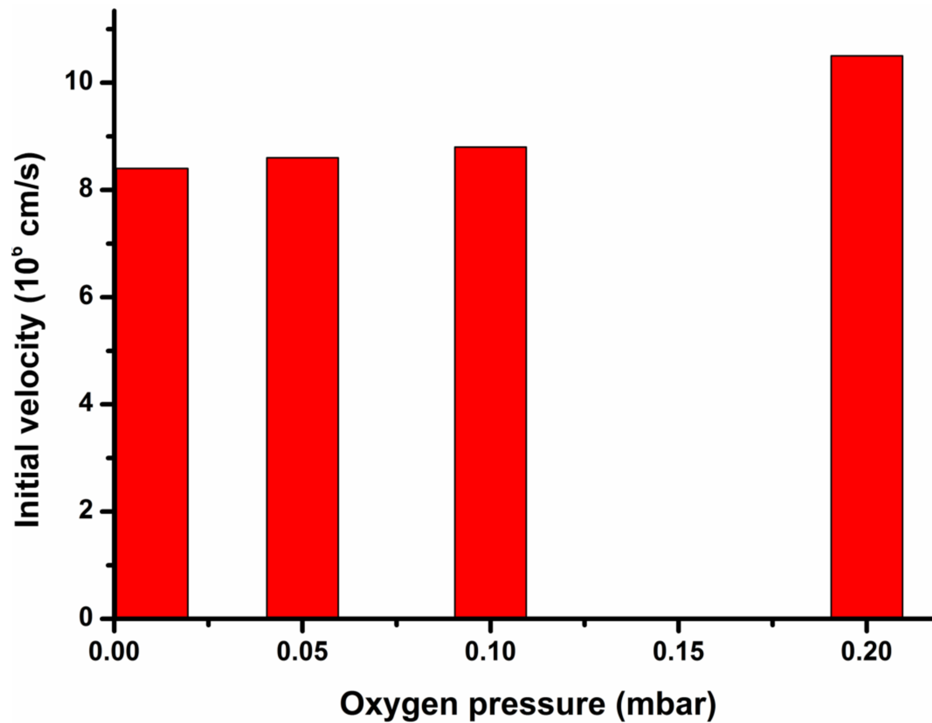

Figure 4.6: Plasma plume initial velocity for different oxygen pressure as indicated in Table 4.1.

The classical drag model predicted that v_0 in this study decreases as the pressure decreases from 0.2 mbar (10.5 x 10^6 cm/s) to 0.01 mbar (8.4 x 10^6 cm/s) as given in Table 4.1 and Figure 4.6. Whereas in Ngom *et al.* [4.15], the classical drag model parameters predicted that the v_0 is increases as the pressures decreases. Harilal *et al.* [4.12] and Ngom *et al.* [4.15] are some of the several authors who used the classical drag model to describe the plasma plume expansion and found that the plume expansion at later stages was well described by the classical drag model, which is in agreement with this work. However Geohegan *et al.* [4.16] fitted the classical drag model to the propagation of the YBCO plasma plume front data and found that the model shows better agreement at low background pressure (0.13 mbar) and initial expansion times.

C. Point-Blast-Wave Model

The point-blast-wave model predicts that the plume will continue to propagate by neglecting viscosity. The point-blast wave model is known to be accurate in the initial shock propagation conditions. The position of the plume front from the target, at time t, can be described as [4.11, 4.17]:

$$x(t) = \xi \left(\frac{E}{\rho}\right)^{\frac{1}{n+2}} t^{\frac{2}{n+2}}, \tag{4.3}$$

where ρ is the background gas density, E is the amount of energy released during the ablation, ξ is a constant which is dependent on the specific heat capacity ratio and n is equal to 3, 2, 1 for spherical-, cylindrical- and plane-wave propagation types respectively. We note that the plume expansion, $x(t)$ follows a simple power law, proportional to $t^{0.4}$,$t^{0.5}$,$t^{0.7}$ for spherical-, cylindrical-, and plane-wave propagation types, respectively. The particle energy distribution becomes more isotropic, giving rise to the approximately hemispherical behaviour of the shock-wave propagation observed in a number of PLD experiments [4.17]. When one needs to find the rate of this expansion, one needs to differentiate equation (4.3) with time and this yield

$$v(t) = \frac{dx}{dt} = \frac{2}{n+2} \xi \left(\frac{E}{\rho}\right)^{\frac{1}{n+2}} \left(t^{\frac{2}{n+2}} t^{-1}\right) \tag{4.4}$$

Comparing the shock wave velocity equation (4.4) to the classical drag velocity equation (4.2) reveals the fact that while the initial velocity v_0 in the classical drag equation must be a constant regardless of the partial pressures of the gases in the chamber, the instantaneous velocity of the plume front from the shock wave equation must decrease with time until the stopping distance.

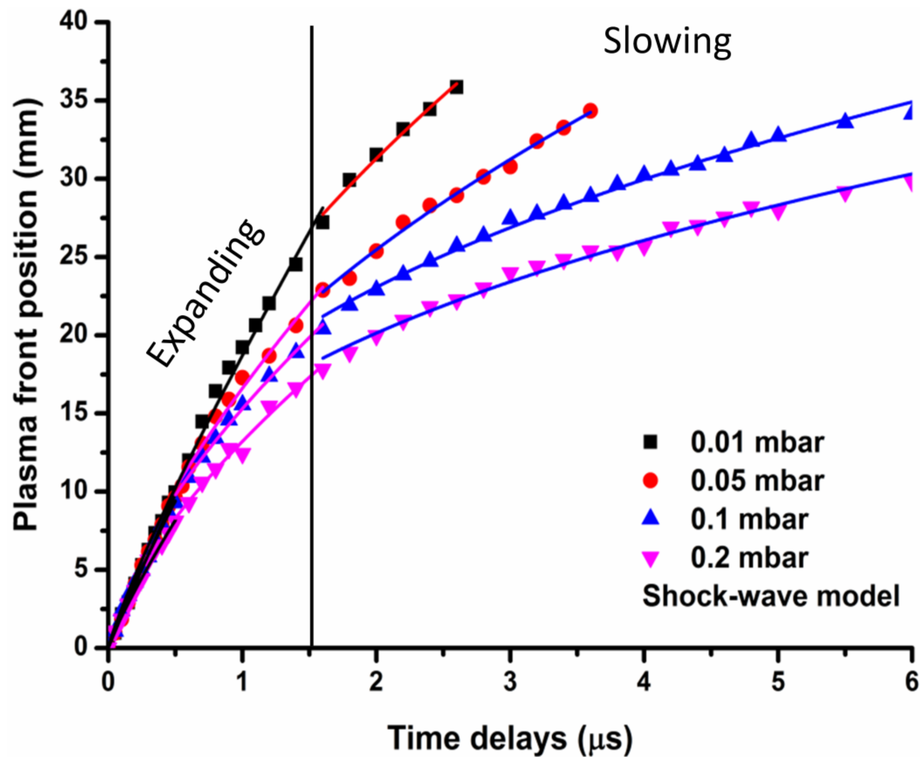

Figure 4.7: Propagation of plasma plume front position for different oxygen gas pressure fitting with the point-blast-wave which is indicating a free-expansion (black), plane-wave front (magenta), cylindrical-wave front (red) and spherical-wave front (blue).

Figure 4.7 indicates the propagation of plasma plume front position for different oxygen gas pressure fitted with the shock-wave model. The shock-wave model fits well at intermediate stages indicating that this is where the shock-wave phenomenon approximately takes place. This was observed by Tillack *et al.* [4.18] as well. The model indicates that the shock-wave front changes from plane-wave to cylindrical for both low oxygen pressures (0.01 and 0.05 mbar) at the certain distance and time, as given in Figure 4.7. At high oxygen pressures (0.2 and 0.1 mbar), the shock-wave front changes from plane-wave front propagation to spherical-wave front (which is an ideal shock condition) for certain distance and time, as shown in Figure 4.7. This is expected as we

observe the plume species interact with the oxygen gas in the captured ICCD images which results in the sharpening of the plume at the edge. This is the time when the shock-wave takes place as given in Figures 4.2 (a) and 4.2 (b). Misra *et al.* [4.19] observed that the plume propagation changes with increasing oxygen gas pressure and they speculated that this is due to the growth of instability at high pressure.

In this chapter, we conjecture that the plume propagation transformations with respect to the increasing oxygen gas pressure is due to the plasma-oxygen interactions which homogenizers the plasma front shape to a hemispherical shape and which in turn leads to ideal hemispherical shock-like expansion. The experimental results fit well with the model at intermediate times and this may be due to the diffusion of ambient particles in the ablated plasma which leads to increase in collision at later times.

4.3 Conclusions

The expansion dynamics of a laser ablation plume produced during KrF excimer laser irradiation of a VO_2 target in oxygen ambient was investigated using a fast ICCD camera. The time evolution of the plume images has enabled observations of the plume propagation behaviour under different background gas pressures, from vacuum to a few mbars. The experimental findings reveal several interesting features which are of general character and interest, with the temporal dynamics found to be dependent on the oxygen pressure. The classical drag and shock-wave models were used to understand the plasma plume expansion and plume species propagation. The stopping distance, initial velocity, slowing coefficient and the shock condition were determined.

The classical drag model fitted well at later stages to the ICCD plume images. The shock-wave model fitted well at intermediate stages of the ICCD plume images. The Ideal shock condition was determined at high oxygen gas pressure. These results were consistent with the ICCD plume images observation of the shock sharpening and shock wave at the ICCD images.

References

4.1 R.K. Singh, J. Narayan, "Pulsed-laser evaporation technique for deposition of thin films: physics and theoretical model," Phys. Rev. B **41**, 8843 (**1990**).

4.2 D.L. Wiggins, C.T. Raynor, J.A. Johnson III, "Evidence of inverse bremsstrahlung in laser enhanced laser-induced plasma," Phys. Plasmas **17**, 103303 (**2010**).

4.3 D.B. Chrisey and G.K. Hubler, Pulsed Laser Deposition of Thin Films, Wiley, New York (**1994**).

4.4 S.I. Anisimov, D. Bauerle, B.S. Lukyanchuk, "Gas dynamics and film properties in pulsed laser deposition of materials," Phys. Rev. B **48**, 12076 (**1993**).

4.5 S. Lafane, T. Kerdja, S. Abdelli-Messaci, Y. Khereddine, M. Kechouane, O. Nemraoui, "Correlation of plume dynamics and oxygen pressure with VO_2 stoichiometry during pulsed laser deposition," Appl. Phys. A **112**, 159 (**2013**).

4.6 S. Lafane, T. Kerdja, S. Abdelli-Messaci, S. Malek, M. Maaza, "Plasma dynamics study by fast imaging and $Sm_{1-x}Nd_xNiO_3$ thin film deposition," Appl. Surf. Sci. **256**, 1377 (**2009**).

4.7 S. Lafane, T. Kerdja, S. Abdelli-Messaci, S. Malek, M. Maaza, "Laser induced plasma study by fast imaging for $Sm1-xNd_xNiO_3$ thin film deposition," Appl. Phys. A **98**, 375 (**2010**).

4.8 S.S. Harilal, C.V. Bindhu, M.S. Tillack, F. Najmabadi, A.C. Gaeris, "Plume splitting and sharpening in laser produced aluminium plasma," J. Phys. D.: Appl. Phys. **35**, 2935 (**2002**).

4.9 R.F. Wood, J.N. Leboeuf, D.B. Geohegan, A.A. Puretzky, K.R. Chen, "Dynamics of plume propagation and splitting during pulsed laser ablation of Si in He and Ar," Phys. Rev. B **58**, 1533 (**1998**).

4.10 S. Amoruso, A. Sambri, M. Vitiello, X. Wang, "Propagation of $LaMnO_3$ laser ablation plume in oxygen gas," Appl. Surf. Sci. **252**, 4712 (**2006**).

4.11 P.E. Dyer, J. Sidhu, "Spectroscopic and fast photographic studies of excimer laser polymer ablation," J. Appl. Phys. **64**, 4657 (**1988**).

4.12 S.S. Harilal, C.V. Bindhu, M.S. Tillack, F. Najmabadi, A.C. Gaeris, "Internal structure and expansion dynamics of laser ablation plumes into ambient gases," J. Appl. Phys. **93** (5), 2380 (**2003**).

4.13 A. Kushwaha, R.K. Thareja, "Dynamics of laser-ablated carbon plasma formation of C_2 and CN," Appl. Opt. **47**, G65 (**2008**).

4.14 V. Berardi, S. Amoruso, N. Spinelli, M. Armenante, R. Velottaa, F. Fuso, M Allegrini, E Arimonodo, "Diagnostics of $YBa_2CuO_{7-\sigma}$ laser plume by time-of-flight mass spectrometry", J. Appl. Phys. **76** (12), 8077 (**1994**).

4.15 B.D. Ngom, S. Lafane, A. Dioum, N. Manyala, S. Abdelli-Messaci, R.T. Kerdja, R. Madjoe, R. Nemutudi, M. Maaza, A.C. Beye, "The influence of plasma dynamics on the growth of $Sm_{0.55}Nd_{0.45}NiO_3$ solid solution during pulsed laser deposition", J. Phys. and Chem. Solids **72**, 1218 (**2011**).

4.16 G.H. Geohegan, "Physics and diagnostics of laser ablation plume propagation for high-T_c superconductor film growth," Thin Solid Film **220**, 138 (**1992**).

4.17 S. Lafane, T. Kerdja, S. Abdelli-Messaci, S. Malek, M. Maaza, "Laser-induced plasma study by fast imaging for $Sm_{1-x}Nd_xNiO_3$ thin film deposition," Appl. Phys. A. **98**, 375 (**2010**).

4.18 M.S. Tillack, D.W. Blair, S.S. Harilal, "The effect of ionization on cluster formation in laser ablation plumes," Nanotechnology **15**, 390 (**2004**).

4.19 A. Misra, R.K. Thareja, "Investigation of laser ablated plumes using fast photography," IEEE Transactions on Plasma Sci. **27** (6), 1553 (**1999**).

Chapter 5

Investigation of Vanadium-Oxygen Plasma Species Emission in Oxygen Ambient

The plasma plume expansion and propagation in various oxygen gas pressure was investigated in Chapter 4. The results indicated that the plasma plume propagation from one expansion regime to the next varies, depending on the oxygen gas pressure. It is important to investigate the chemical species that constitute the sample by making use of the same plasma formed by a focused laser pulse in pulsed laser deposition (PLD) and optical emission spectroscopy (OES) [5.1]. This is suitable for performing the deposition process control [5.2], and this depends on the understanding of the basic physics and chemistry associated with laser-target and particle-particle interaction inside the laser induced plasma plume [5.3]. The physico-chemical characteristics of the obtained thin films depend on irradiation conditions such as laser energy density, laser wavelength, laser pulse duration, the nature of the background gas and the substrate temperature [5.4]. The interaction process of the laser–induced plasma with the background gas is very complex and leads to a deposited thin film with different properties in the presence of the background gas. It is important, then, to have good control of these phenomena and of the ablated target surface, in order to understand the laser ablation process and deposition of thin films [5.4].

Vanadium-oxygen plasma induced by laser in a background gas has allowed depositing a variety of thin films such as vanadium pentoxide (V_2O_5) [5.5], vanadium trioxide (V_2O_3) [5.6], vanadium dioxide (VO_2) [5.7] and a series of oxides [5.8]. Despite all the research already published there have been no reports on the plasma plume species of

vaporized VO_2 and vanadium (V) targets. Beke *et al.* [5.9] studied the elemental composition and temporal and spatial distributions of vanadium atoms and ions in the laser-induced vanadium oxide plasma by ablating V_2O_5 under high vacuum using OES. They measured two dominant species: neutral V atoms and single V ions. In this chapter, the effect of an oxygen atmosphere on the emission species of a vanadium-oxygen plasma generated using 248 nm, 25 ns pulses from an excimer KrF laser have been investigated by using a fast intensified charged coupled device (ICCD) camera and optical emission spectroscopy. The ambient gas effect on plasma plume species propagation will be discussed for both target (VO_2 and V).

5.1 Experimental Set-up

The schematic diagram of the experimental setup used to conduct the study of the emission species of VO_2 and V plasma plume of the laser-ablated targets in this Chapter is discussed in Chapter 4 and is shown in Figure 4.1. It will be only briefly discussed here. The optical emission study of ablation plasma plume of VO_2 and V targets were carried out under vacuum and in a gas pressure range of 0.01-0.20 mbar, making use of a spectrometer, a digital oscilloscope, a photomultiplier and as well an ICCD camera. The entrance slit spectrometer was fixed to width of 100 μm and height of 2 mm. This determines the viewed plasma portion and the spatial resolution (100 μm X 2mm). The plasma emission is translated horizontally with a step of 0.3 mm on the spectrometer entrance slit to provide spatially resolved measurements. A spectrometer containing a 1200 grooves/mm grating leading to a spectral resolution of 0.08 nm is coupled to a fast Hamamatsu R928 photomultiplier with 2.2 ns rise time. The latter is connected to a digital oscilloscope (Tektronix TDS3032) with a 400 MHz band pass. The pulsed energy

was fixed at 120 mJ which gives a laser fluence of 2 Jcm^{-2}. The plume emission species of VO_2 and V experiments were conducted using the same oxygen pressures (0.01 to 0.2 mbar) and pulsed energy conditions as that used for the plasma plume study in Chapter 4, as the viewing optics position from the surface targets varied.

5.2 Results and Discussion

A. Influence of Ambient Gas on Plasma Plume Species Emission

Due to the importance of the plume-oxygen gas interaction on the degree of oxygen incorporation into the deposited films, a characterisation study of VO_2 and V laser ablation in the oxygen environment by optical emission spectroscopy was done. The optical emission spectroscopy was used to diagnose the plasma plume [5.10] and it is suitable for performing the deposition process control. All emission species as a function of the distance from the target surface have been measured. Table 5.1 summarises the main emission lines recorded during VO_2 and V ablation for several oxygen pressures, showing the peak wavelength and excitation energy.

Table 5.1: Optical emission lines with corresponding electron transitions in V atoms (V I), singly charged V^+ ions (V II) and VO.

Atomic species	Wavelength (nm)	Energy (eV)	Transition
V I	437.85	6.746	$1S^4\text{-}^4F_{3/2}$
V II	326.1	14.618	$1S^2\text{-}^5D_0$
VO	608.56	2.037	-

B. Intensity of the Plasma Plume Species of Ablated VO_2 and V Targets

The maximum emission intensity of V I, V II and VO were measured for different oxygen pressure and under vacuum. The maximum emission intensity of all the species was determined from the emission intensity spectrum of the species. The emission intensity spectrum of the species was recorded at each position from the target surface using digital oscilloscope and photomultiplier. The typical example of the emission intensity spectrum of the species is shown in Figure 5.1. The spectrum indicates that the emission intensity rapidly rise to the maximum and decay fast to the minimum. The maximum emission intensity of the species at each position from the target surface then was determined from the emission spectrum.

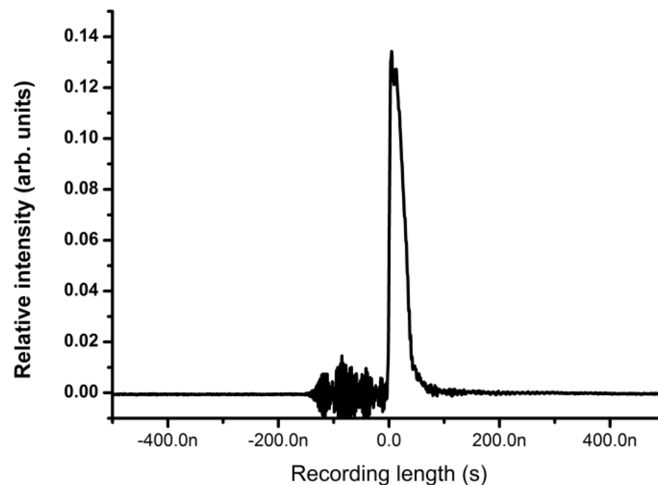

Figure 5.1: Typical example of the emission intensity spectrum.

The maximum emission intensity of V I, V II and VO are plotted versus the corresponding observation distance for different oxygen pressure and under vacuum, as shown in Figure 5.2. We observed a linear increase on the emission intensity close to

the target surface until the emission intensity reaches the maximum for all the species as shown in Figures 5.2 (a), 5.2 (b) and 5.2 (c), respectively.

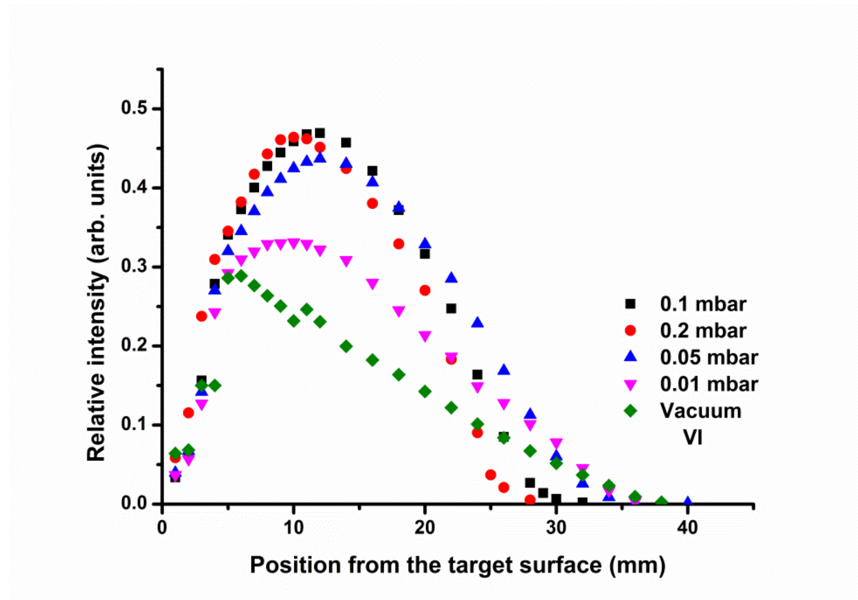

Figure 5.2 (a): The maximum emission intensity of the species V I (of VO_2 target) as a function of the distance from the target surface for different oxygen pressure.

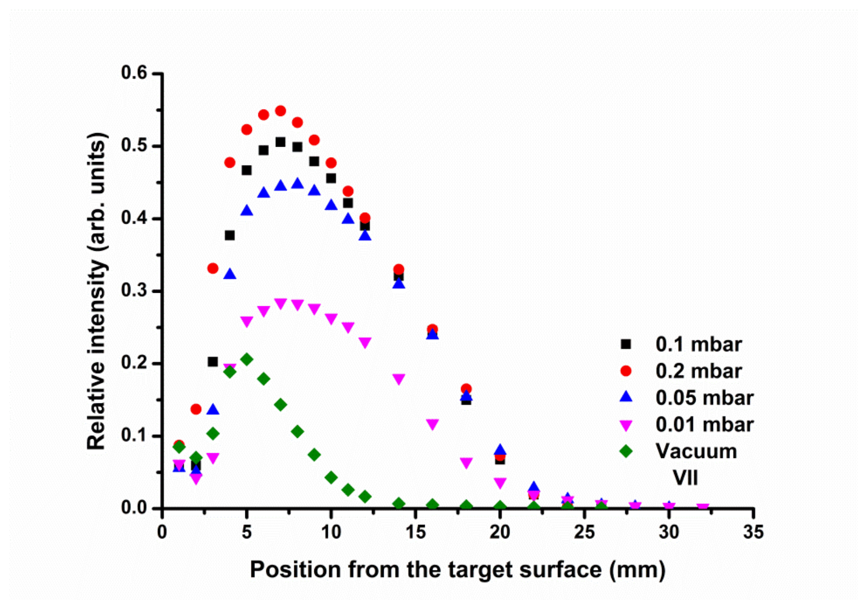

Figure 5.2 (b): The maximum emission intensity of the species V II (of VO_2 target) as a function of the distance from the target surface for different oxygen pressure.

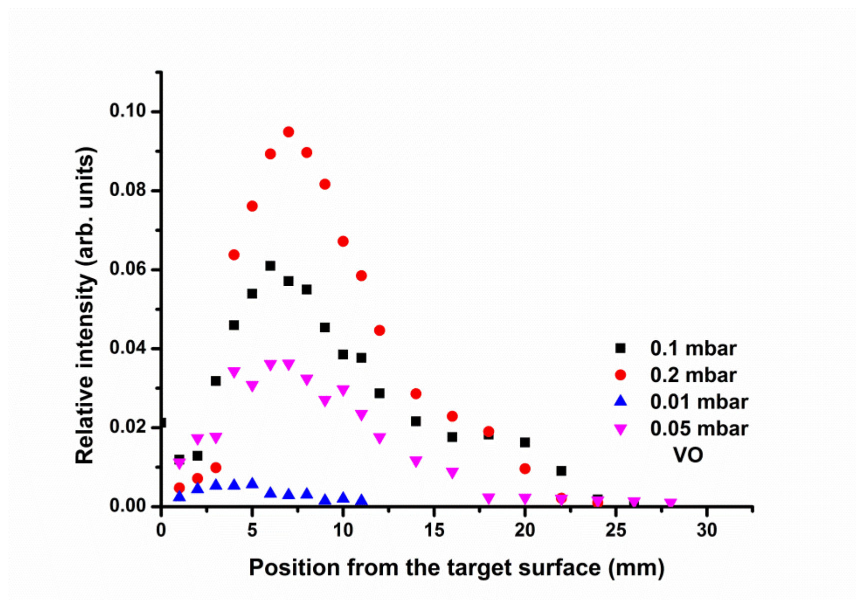

Figure 5.2 (c): The maximum emission intensity of the species VO (of VO_2 target) as a function of the distance from the target surface for different oxygen pressure.

V I emission intensity has a wide profile with a maximum at approximately 10 mm from the target surface and slow decreases with the distance from the target surface, as shown in Figure 5.2 (a). Concerning the emission intensity of V II and VO, they have narrow profiles with maxima at approximately 7.5 and 6 mm, respectively from the target surface and slowly decreasing with the distance from the target surface as shown in Figures 5.2 (b) and 5.2 (c). However, as for the emission intensity of V II in vacuum, one observes a decrease as the distance from the target surface increases. Beyond a distance of 35 mm for V I species and 20 mm for species V II and VO, no emission is observed. We observed relatively higher emission intensity at high oxygen pressures than at lower oxygen pressures. Table 5.2 indicates the analysis of the species ratio. The analysis indicates that the V II species is highest, V I species is medium and VO species is

lowest. As the distance increases, the V II species rapidly increases and decay quickly. While the V I species increases slows. Whereas VO species decreases slows.

Table 5.2: Analysis of the species ratio of VO_2 target.

Position	Relative intensity of the species (arb. units) at 0.1 mbar			Percentage (%)			
(mm)	V I	V II	VO	Total	V I	V II	VO
1	0.03	0.06	0.02	11.41	29.61	51.75	18.63
2	0.06	0.06	0.01	13.42	46.83	44.31	8.87
3	0.16	0.20	0.01	37.18	42.04	54.49	3.47
4	0.28	0.38	0.03	68.75	40.53	54.84	4.63
5	0.34	0.47	0.05	85.36	39.92	54.70	5.38
6	0.37	0.49	0.05	92.13	40.47	53.67	5.85
7	0.40	0.51	0.06	96.37	41.40	52.29	6.31
8	0.43	0.50	0.06	98.34	43.47	50.73	5.81
9	0.44	0.48	0.06	97.88	45.43	48.95	5.62
10	0.46	0.46	0.05	96.00	47.80	47.47	4.73

11	0.47	0.42	0.04	92.81	50.41	45.44	4.15
12	0.47	0.39	0.04	89.76	52.30	43.50	4.20
14	0.46	0.32	0.03	80.71	56.66	39.79	3.55
16	0.42	0.25	0.02	68.84	61.23	35.63	3.14
18	0.37	0.15	0.02	53.94	68.97	27.77	3.26
20	0.32	0.07	0.02	40.25	78.66	16.80	4.54
22	0.25	0.02	0.02	28.31	87.44	6.82	5.74
24	0.16	0.00	0.01	17.63	92.63	1.97	5.13
26	0.09	0.00	0.02	17.63	92.90	1.97	5.13

Emission intensity of all the plasma plume species are shown in Figures 5.3 (a), 5.3 (b) and 5.3 (c), respectively. We observed a maximum intensity close to the target and as the target substrate distance increases the emission intensity decreases for all the plumes species as given in Figures 5.3 (a), 5.3 (b) and 5.3 (c), respectively. Additionally, for V I plume species the emission intensity slowly decreases until approximately 2.5 mm and start to slowly increase again until approximately 7.5 mm as given in Figure 5.3 (a). From 7.5 mm decreases as the target substrate distance increases as given in Figure 5.3 (a). We observed highest emission intensity for 0.2 mbar oxygen pressure followed by 0.1 mbar, 0.05 mbar, 0.01 mbar and vacuum, for all the plume species as given in Figures 5.3 (a), 5.3 (b) and 5.3 (c), respectively.

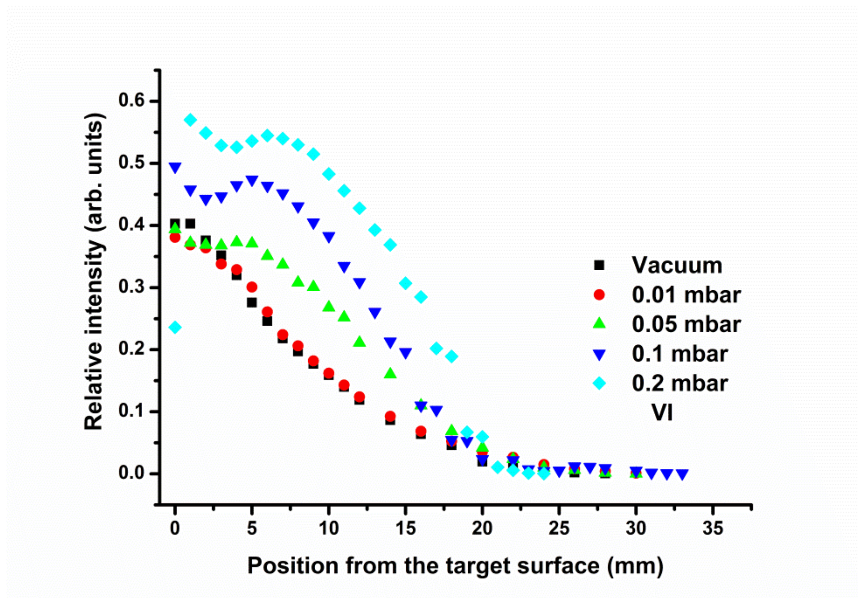

Figure 5.3 (a): The maximum emission intensity of the species V I (of V target) as a function of the distance from the target surface for different oxygen pressure.

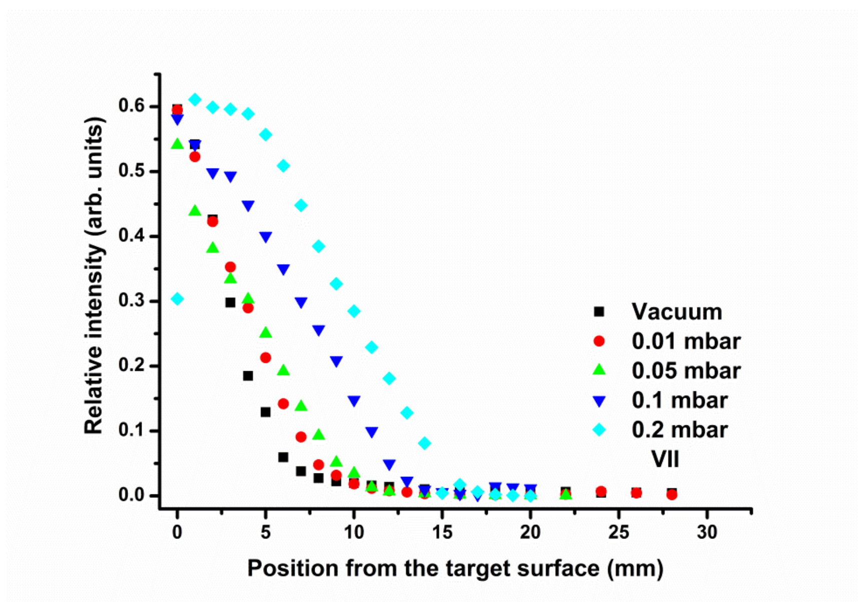

Figure 5.3 (b): The maximum emission intensity of the species V II (of V target) as a function of the distance from the target surface for different oxygen pressure.

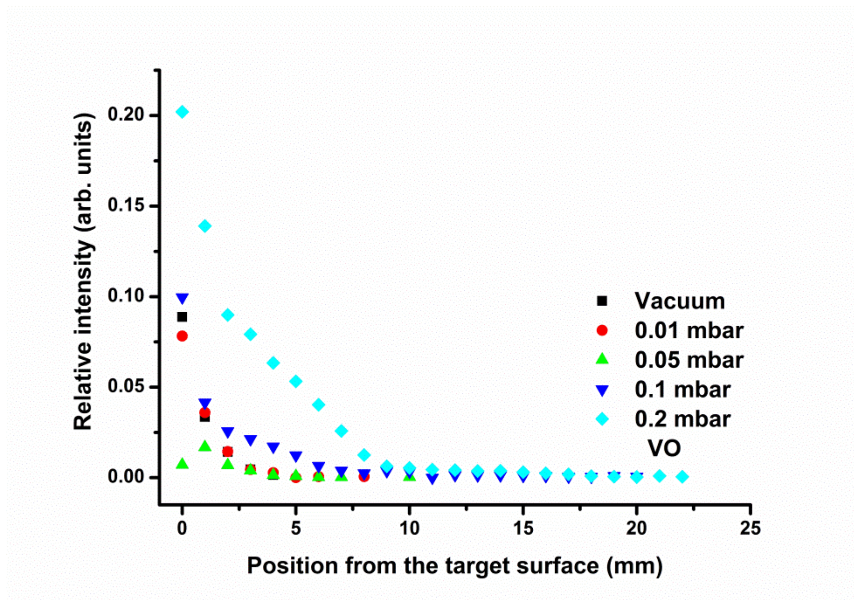

Figure 5.3 (c): The maximum emission intensity of the species VO (of V target) as a function of the distance from the target surface for different oxygen pressure.

Amoruso *et al.* [5.11] and Canualescu *et al.* [5.12] also observed the maximum emission intensity far from the target surface as shown in Figure 5.2. Whereas Abdelli-Messaci *et al.* [5.13] also observed the maximum emission intensity close to the target surface as shown in Figure 5.3. The emission increases could be interpreted as a presence of a high chemical reactivity in this region. It could correspond to the place of species condensation, which is due to the confinement of the plasma front by the gas. At the maximum intensity the kinetic energy of this species is very high. Thin films deposited within maximum intensity give a non-uniform film and a mixed structure due to the high kinetic energy of the species [5.11, 5.12, 5.13]. To deposit an uniform film one need to deposit at low intensity where the kinetic energy of the species is low. No emission was observed for VO at low oxygen gas pressure and vacuum as shown in Figure 5.3 (c). This is understandable since at low oxygen gas pressure, the plume expands freely

without any external viscous force and there is little interaction between the plume and the low density of oxygen atoms present. This is because the species are completely dissociated, due to the strong collisions between the plasma species. Table 5.3 indicates the analysis of the species ratio of V target. The analysis indicates that all species are highest close to the target and decay slows until it disappears.

Table 5.3: Analysis of the species ratio of V target.

Position	Relative intensity of the species (arb. units) at 0.1 mbar			Percentage (%)			
(mm)	V I	V II	VO	Total	V I	V II	VO
2	0.44	0.50	0.03	96.77	45.78	51.57	2.66
3	0.45	0.49	0.02	96.23	46.45	51.34	2.21
4	0.47	0.45	0.02	93.12	49.94	48.22	1.85
5	0.47	0.40	0.01	88.73	53.42	45.19	1.39
6	0.46	0.35	0.01	82.15	56.48	42.73	0.79
7	0.45	0.30	0.00	75.59	59.80	39.69	0.52
8	0.43	0.26	0.00	69.04	62.42	37.22	0.35
9	0.41	0.21	0.00	61.77	65.57	33.84	0.60
10	0.38	0.15	0.00	53.44	71.67	27.70	0.63
11	0.34	0.10	0.00	43.50	77.01	22.99	0.00
12	0.31	005	0.00	36.02	85.78	13.82	0.00
13	0.26	0.02	0.00	28.58	91.31	8.22	0.00

14	0.21	0.01	0.00	22.40	95.09	4.32	0.00
15	0.20	0.01	0.00	20.28	96.65	2.86	0.00
16	0.11	0.00	0.00	11.42	96.30	0.00	0.00

C. Spatio-Temporal Evolution of Plasma Plume Species of VO_2 and V Targets

The classical drag model was used to describe the plasma plume species expansion for both VO_2 and V targets. Figure 5.4 shows the propagation graphs for all the species (V I, V II and VO) of VO_2 target. These graphs indicate the function of the distance from the target surface against the function of the time at various oxygen pressures for 2 J/cm^2 laser fluence fitted with the classical drag model, respectively.

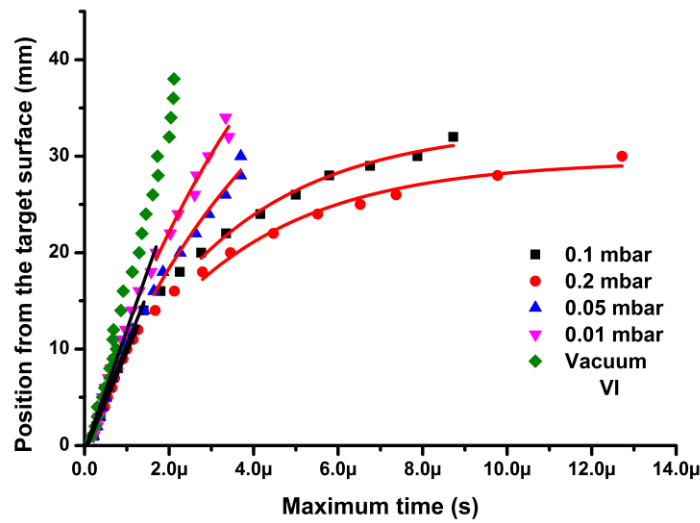

Figure 5.4 (a): Propagation of V I plume species (of VO_2 target) for different oxygen gas pressures fitted with the classical drag model (red) and a free-expansion (black).

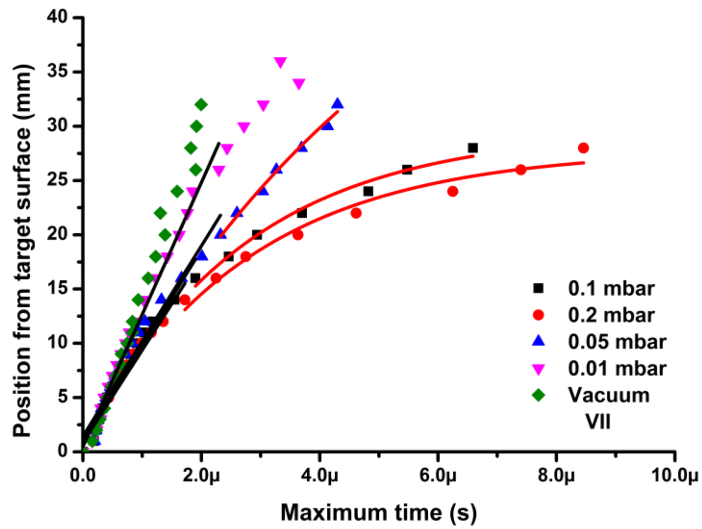

Figure 5.4 (b): Propagation of V II plume species (of VO_2 target) for different oxygen gas pressured fitted with the classical drag model (red) and a free-expansion (black).

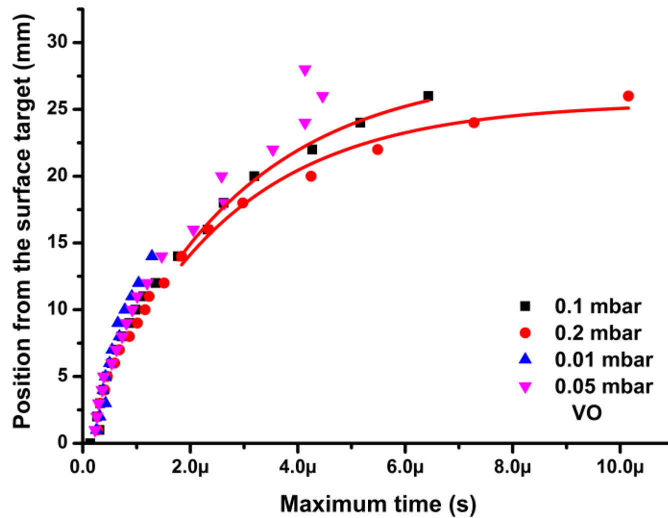

Figure 5.4 (c): Propagation of VO plume species (of VO_2 target) for different oxygen gas pressures fitted with the classical drag model (red).

From all the Figures 5.4, we observe that V I, V II and VO evolutions have the same behaviour up to approximately 12 mm from the target surface for different oxygen pressures, which means that the various species propagate at the same speed. At oxygen pressures of 0.1 mbar and 0.2 mbar, the expansion remains linear in the early time and the deviation increases with increasing time from free-plume species emission expansion to plume species emission slowing down for all the species. In this regime of the propagation, the ejected species collide with the oxygen gas molecules and lose their kinetic energy and later the plume species emission stops completely. The ejected species diffuse into the oxygen gas until they reach a distance where they lose their kinetic energy. The classical drag model fitted very well with the experimental data for all the species and at the later stage. The stopping distance, initial velocity and slowing coefficient are given in Table 5.4.

Table 5.4: Drag model parameter values for the plasma plume of VO_2 target at different oxygen pressures.

Classical drag model parameter for VO_2 target					
	Pressure (mbar)	**0.2**	**0.1**	**0.05**	**0.01**
V I	X_f (cm)	0.30	0.33	0.50	0.65
	β (μs^{-1})	3.19	3.12	4.31	4.81
	V_0 (10^6 cm/s)	0.94	1.04	2.14	3.14
V II	X_f (cm)	0.28	0.30	0.59	-

	β (μs^{-1})	2.71	2.63	3.39	-
	V_0 (10^6 cm/s)	0.76	0.78	1.98	-
VO	X_f (cm)	0.26	0.28	-	-
	β (μs^{-1})	2.48	2.65	-	-
	V_0 (10^6 cm/s)	0.63	0.75	-	-

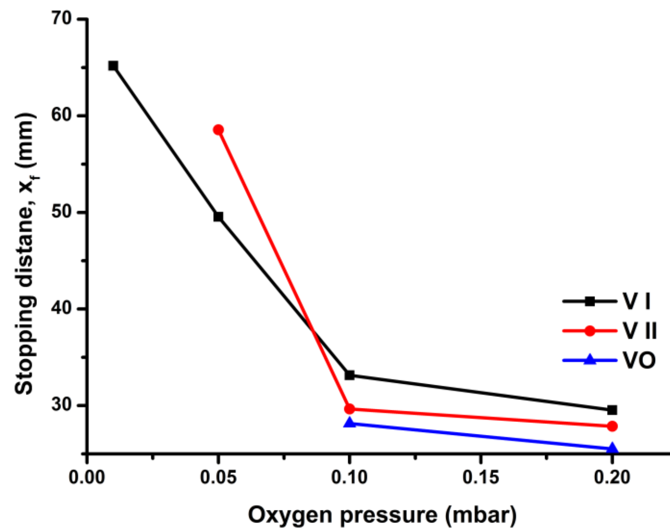

Figure 5.5 (a): Plasma plume stopping distance for different oxygen pressure (of VO_2 target).

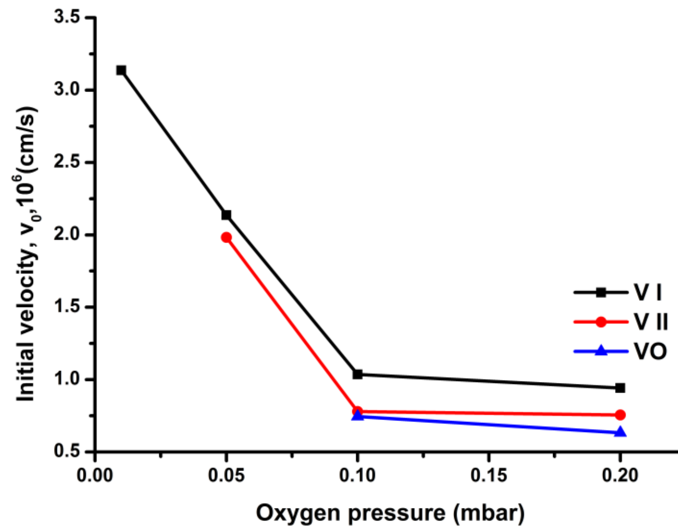

Figure 5.5 (b): Plasma plume initial velocity for different oxygen pressure (of VO_2 target).

The stopping distance and the initial velocity for all the species decreases as the oxygen gas pressure increases as indicated in Table 5.4, Figures 5.5 (a) and 5.5 (b), respectively. This is expected especially on the stopping distance due to the fact that as the oxygen gas increases the plume species interact with the oxygen gas and this slows the plume species propagation. While the increases of the initial velocity of the species is not in agreement with plume initial velocity in Chapter 4, which decreases as the oxygen pressure increases as shown in Figure 4.6 and Table 4.1. Currently, the reason for this observation is not yet known. However, may be this is due to the fact that some individual species velocity increases and other species velocity decreases as the oxygen gas pressure increases thus make the average plume initial velocity decreases.

Figure 5.6 shows the plot of the distance from the target surface against maximum time graph of the studied species (V I, V II and VO) of V target for the various oxygen pressure fitted with the classical drag model, respectively. Figure 5.6 (a) reveals a linear increase for vacuum, and these 0.01 – 0.1 mbar oxygen gas pressure, respectively. While for 0.2 mbar reveals a linear increase at early time and deviates as the distance from the surface target increases as shown in Figure 5.6 (a). This was also observed for all the species and oxygen pressures (Figures 5.6 (b) and 5.6 (c), respectively). The classical drag model fitted well at later stage for only oxygen pressures 0.1 and 0.2 mbar (Figure 5.6). For plume species V I, the model fitted well only for 0.2 mbar oxygen pressure (Figure 5.6 (a)). Whereas for plume V II and VO, the model fitted well at later stage for high oxygen pressures only (0.1 and 0.2 mbar) (Figures 5.6 (b) and 5.6 (c), respectively).

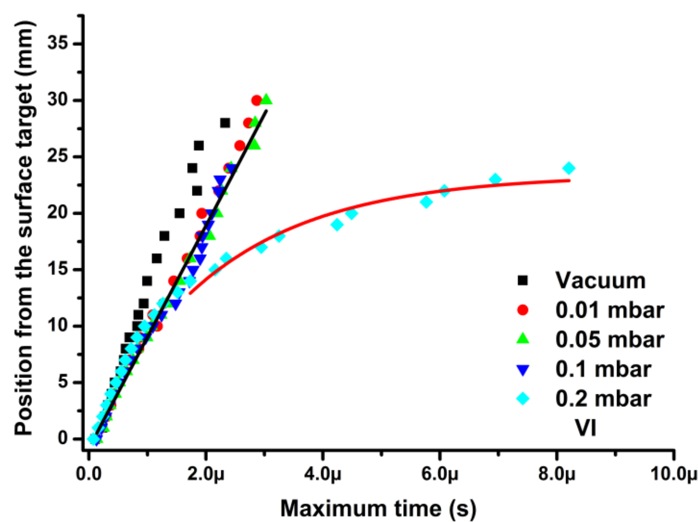

Figure 5.6 (a): Propagation of V I plume species of (of V target) for different oxygen gas pressures fitted with the classical drag model (red) and a free-expansion (black).

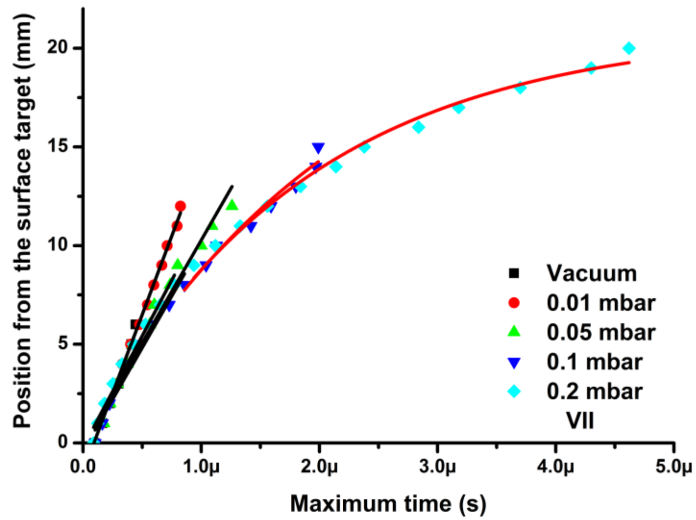

Figure 5.6 (b): Propagation of V II plume species (of V target) for different oxygen gas pressures fitted with the classical drag model (red) and a free-expansion (black).

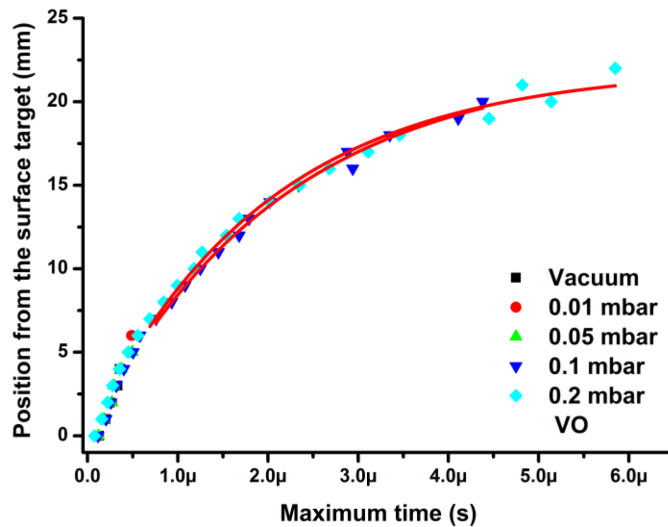

Figure 5.6 (c): Propagation of VO plume species (of V target) for different oxygen gas pressures fitted with the classical drag model (red).

Table 5.5 shows the classical drag model parameter values for the plume species at different oxygen pressures of V target. The classical drag model didn't fit with the experimental data for low oxygen pressure (0.01 and 0.05 mbar) for all the plume species (Figure 5.6). For high oxygen pressures (0.1 and 0.2 mbar), we found that the stopping distance and initial velocity increases as the oxygen pressure decreases (Table 5.5) for plume species V I and VO.

Table 5.5: Drag model parameter values for the plume species of V target at different oxygen pressures.

Classical drag model parameter for V target					
	Pressure (mbar)	**0.2**	**0.1**	**0.05**	**0.01**
V I	X_f (cm)	0.23	-	-	-
	β (μs^{-1})	2.16	-	-	-
	V_0 (10^6 cm/s)	0.51	-	-	-
V II	X_f (cm)	0.21	0.24	-	-
	β (μs^{-1})	1.84	2.17	-	-
	V_0 (10^6 cm/s)	0.39	0.52	-	-
VO	X_f (cm)	0.22	0.22	-	-
	β (μs^{-1})	1.97	2.13	-	-
	V_0 (10^6 cm/s)	0.43	0.48	-	-

Point-blast-wave model was used also to describe the plasma plume species expansion for both VO_2 and V targets. Figure 5.7 is a plot of the distance from the target surface against the maximum time graph of the studied species of VO_2 target for the different oxygen gas pressures. The model fitted well at later stages of plume propagation for all the plume species.

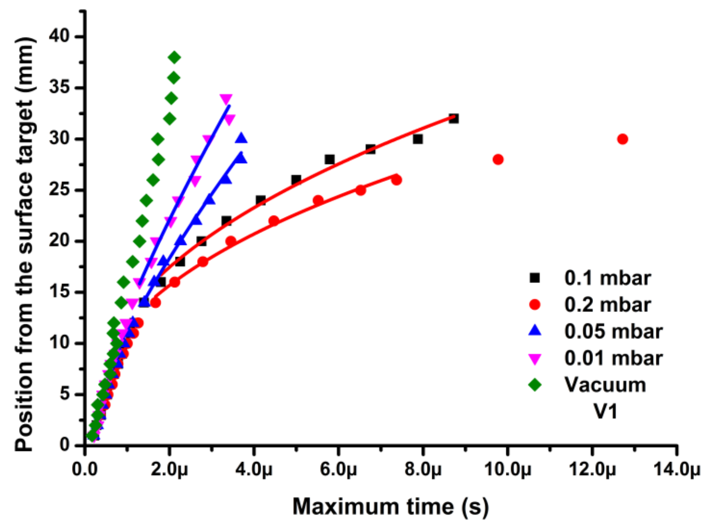

Figure 5.7 (a): Propagation of V I plume species (of VO_2 target) for different oxygen gas pressures fitted with the shock-wave model which is indicating plane-wave front (blue) and spherical-wave front (red).

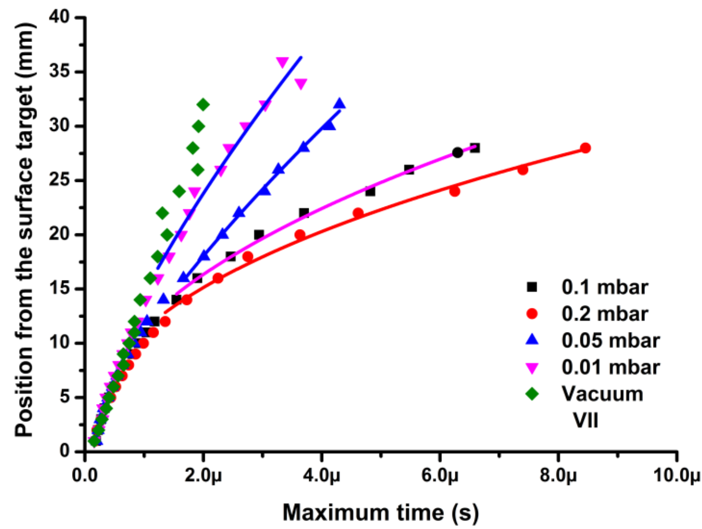

Figure 5.7 (b): Propagation of V II plume species (of VO_2 target) for different oxygen gas pressures fitted with the shock-wave model which is indicating plane-wave front (blue colour), cylindrical-wave front (pink) and spherical-wave front (red).

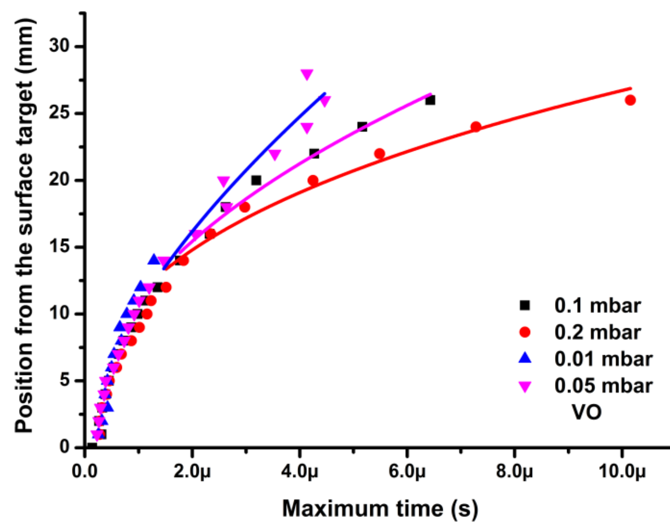

Figure 5.7 (c): Propagation of VO plume species (of VO_2 target) for different oxygen gas pressures fitted with the shock-wave model which is indicating plane-wave front (blue), cylindrical-wave front (pink) and spherical-wave front (red).

In Figure 5.7 (a), the model indicates that the shock-wave front is only spherical-wave front for high oxygen pressures (0.1 and 0.2 mbar), which is an ideal shock condition. Whereas for low oxygen pressures (0.01 and 0.05 mbar), the model indicates that the shock-wave front is only plane-wave front. In Figure 5.7 (b), the model reveals that the shock-wave front is spherical-wave front (0.2 mbar), cylindrical-wave front (0.1 mbar) and is plane-wave front (0.05 and 0.01 mbar). The model in Figure 5.7 (c) indicates that the shock-wave front is spherical-wave front (0.2 mbar), cylindrical-wave front (0.1 mbar) and is plane-wave front (0.05 mbar). As discussed earlier this is expected due to the fact that at high oxygen gas pressure, the plume species interacts with the oxygen gas and at low oxygen pressure there is no enough interaction between the plume species and the oxygen gas as indicated in the ICCD plume images.

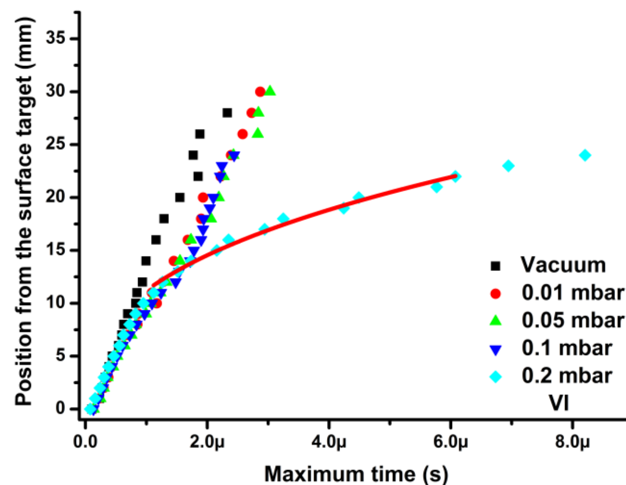

Figure 5.8 (a): Propagation of V I plume species (of V target) for different oxygen gas pressures fitted with the shock-wave model which is indicating spherical-wave front (red).

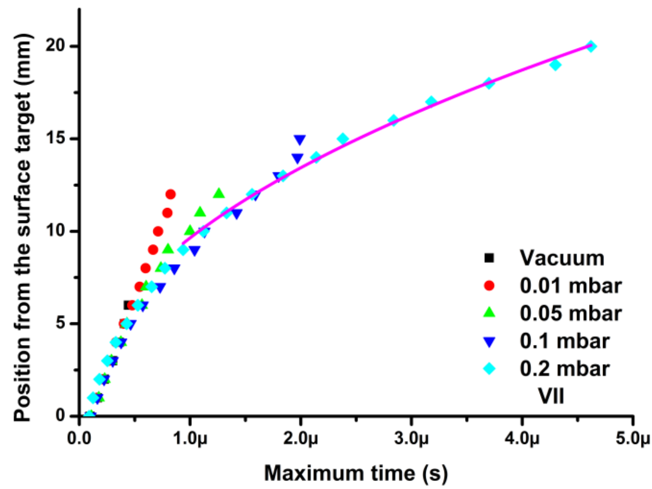

Figure 5.8 (b): Propagation of V II plume species (of V target) for different oxygen gas pressures fitted with shock-wave model which is indicating cylindrical-wave front (pink).

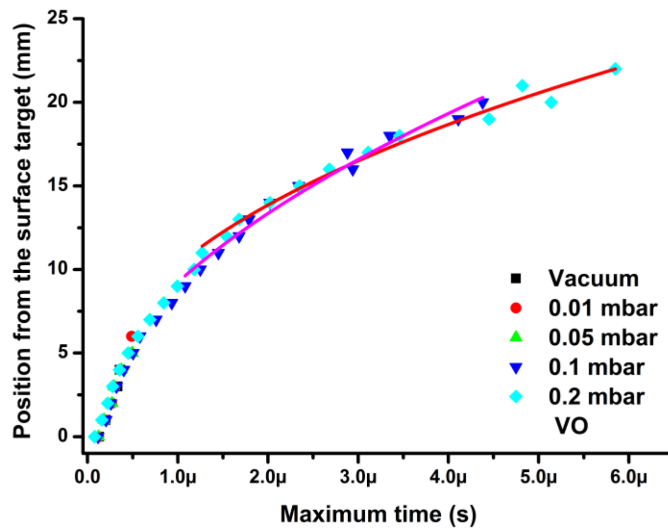

Figure 5.8 (c): Propagation of VO plume species (of V target) for different oxygen gas pressures fitted with the shock-wave model which is indicating cylindrical-wave front (pink) and spherical-wave front (red).

The graphs of the distance from the target surface against maximum time of the studied species (V I, V II and VO) of V target for different oxygen pressure fitted with the shock-wave model for only high oxygen pressure (0.2 and 0.1 mbar) as given in Figures 5.8 (a), 5.8 (b) and 5.8 (c), respectively. The point-blast-wave model fitted very well with the experimental data at the later stages of the plume species as given in Figures 5.8 (a), 5.8 (b) and 5.8 (c), respectively. The shock-wave model indicated an ideal shock condition for 0.2 mbar for VO and V I plume species as given in Figures 5.8 (a) and 5.8 (c). The model indicates the shock-wave front is cylindrical-wave front as given in Figure 5.8.

5.3 Conclusions

The classical drag and point-blast-wave models were used to explain the plasma plume species propagation. The stopping distance, initial velocity, slowing coefficient and the shock condition were determined. The classical drag model fitted very well at later stages to all stages of the plume species data. The shock-wave model fitted very well at intermediate stages of the plume species. The ideal shock condition was determined at high oxygen gas pressure for plume species. These results were consistent with the ICCD plume images observation of the shock sharpening and shock wave at the ICCD images.

References

5.1 D.A. Cremers, L.J. Radziemski, "Handbook of Laser-Induced Breakdown Spectroscopy", John Wiley & Sons, Chichester, (**2006**).

5.2 J. Hermann, C. Vivien, A.P. Caricato, C. Boulmer-Leborgne, “A spectroscopic study of laser ablation plasmas from Ti, Al and C targets” Appl. Surf. Sci.**127-129**, 645 (**1998**).

5.3 S.S. Harilal, C.V. Bindhu, V.P.N. Nampoori, C.P.G. Vallabhan, “Time evolution of the electron density and temperature in laser-produced plasma from $YBa_2Cu_3O_7$”, Appl. Phys. B **66**, 633 (**1998**).

5.4 S. Beke, “A review of the growth of V_2O_5 films from 1885 to 2010”, Thin Solid Films **519**, 1761 (**2011**).

5.5 B.S. Allimi, S.P. Alpay, C.K. Xie, B.O. Wells, J.I. Budnick, D.M. Pease, “Resistivity of V_2O_3 thin films deposited on α-plane (110) and c-plane (001) sapphire by pulsed laser deposition”, Appl. Phys. Lett. **92**, 202105 (**2008**).

5.6 D.H. Kim, H.S. Kwok, “Pulsed laser deposition of VO_2 thin films”, Appl. Phys. Lett. **65** (25), 3188 (**1994**).

5.7 C.H. Griffith, H.K. Eastwood, “Influence of stoichiometry on metal-semiconductor transition in vanadium dioxide”, J. Appl. Phys. **45**, 2201 (**1974**).

5.8 D.B. Chrisey, G.H. Hubler (Eds.), “Pulsed laser deposition of thin films”, John Willey Sons Inc., New York, (**1994**).

5.9 S. Beke, L. Kõrösi, L. Nanai, “In-situ optical emission spectroscopy of laser-induced vanadium oxide plasma in vacuum,” Vacuum **86**, 2002 (**2012**).

5.10 S. Amoruso, R. Bruzzese, N. Spinelle, R. Velotta, “Characterization of laser-ablation plasmas”, J. Phys, B **32**, R 131 (**1999**).

5.11 S. Amoruso, B. Toftmann, J. Schou, R. Velotta, X. Wang, “Diagnostics of laser ablated plasma plumes”, Thin Solid Films **453-454**, 562 (**2004**).

5.12 S. Canulescu, E.L. Papadopoulou, D. Anglos, Th. Lippert, C.W. Schneider, A Wokaun, “Mechanisms of the lase plume expansion during the ablation of LiMn2O4”, J. Appl. Phys. **105**, 063107(**2009**).

5.13 S. Abdelli-Messaci, T. Kerdja, A. Bendib, S. Malek, “CN emission spectroscopy study of carbon plasma in nitrogen environment”, Spectrochimica Acta Part B **69**, 955 (**2005**).

Chapter 6

Optimizing the Synthesis of Vanadium-Oxygen Nano-structures by Plasma Plume Dynamics

It is challenging to synthesize monoclinic vanadium dioxide (VO_2) (M1) with well-defined size and morphology because there are several stable vanadium oxide phases [6.1] and several nonhydrate polymorphs of VO_2 [6.2]. Pulsed laser deposition (PLD) is an excellent tool for the deposition of vanadium oxide (V_xO_y) clusters in the nano-scale size range [6.3], but it is presently not selective in the phase that is generated in the final material. Here we overcome these limitations in PLD by making use of the plasma plume dynamics and plume species results obtained in Chapter 4 and 5, respectively.

In this Chapter, we investigate the relationship between the plasma plume dynamics and deposited V_xO_y compound thin films using the same conditions of the oxygen pressure and fluencies used for the plasma plume study in Chapter 4 and Chapter 5. The target used was VO_2. A Corning glass was used as a substrate. The substrate temperature was maintained at 600 ^oC and the target-substrate distance was fixed at 40 mm. X-Ray Diffraction (XRD), Raman spectroscopy, Scanning Electron Microscopy (SEM) and Atomic Force Microscopy (AFM) were used to study the V_xO_y phase, structure, grain size and roughness measurement, respectively. UV-vis-NIR spectrophotometry and Four-point probe both coupled with heating/cooling stages were used to study the optical and electrical properties of VO_2 thin films, respectively.

6.1 Experimental Set-up

The experimental setup used to conduct the study of the plume expansion dynamics of the laser-ablated targets has already been described in previous chapters (Chapters 4 and 5) and will be only briefly discussed here. V_xO_y thin films were subsequently deposited using the same plasma plume parameters, on heated Corning glass substrates (600 °C), which were placed at a target-to-substrate distance of 40 mm for 10 minutes. V_xO_y thin films were deposited using the same oxygen pressures (0.01 – 0.2 mbar) and laser fluence used in Chapters 4.

6.2 Results and Discussion

A. Structural Properties

XRD is a non-destructive technique for characterization of crystalline materials and it provides the information on the structure, phase and other structural parameters [6.4]. Whereas SEM is primarily used to study the surface, structure of bulk specimens [6.5], AFM provides very high resolution images of the sample with resolution on the orders of fractions of a nano-meter as well as to measure the roughness of the material [6.6].

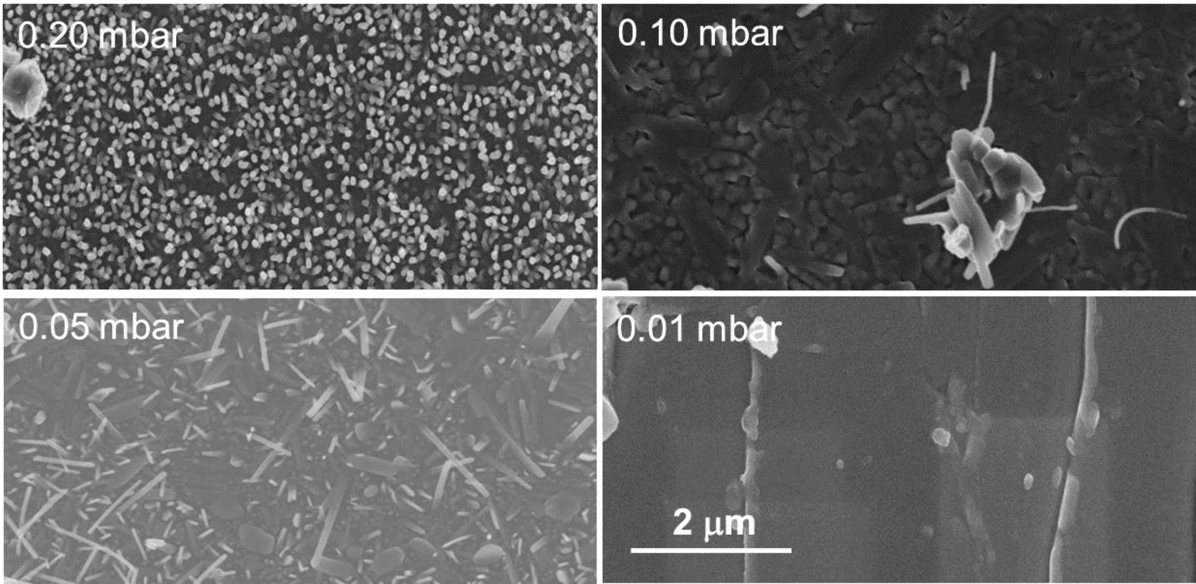

Figure 6.1: SEM micrographs of thin films prepared at various oxygen pressures for target-substrate distance of 40 mm. Scale for all the micrographs is 2 μm.

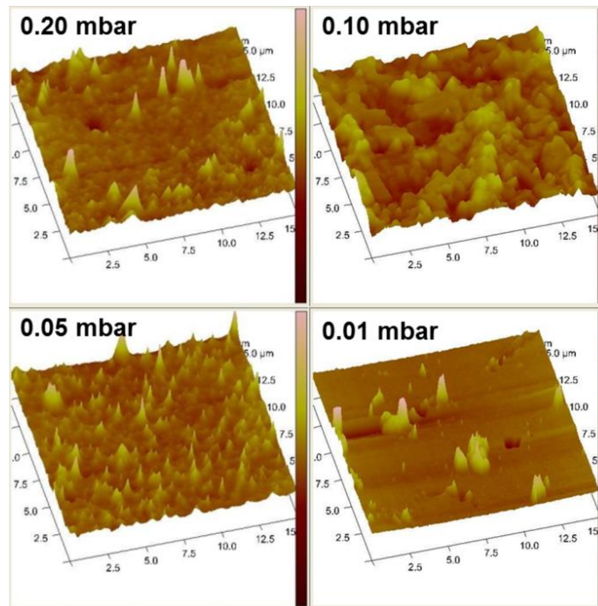

Figure 6.2: AFM images of thin films prepared at various oxygen pressures for target-substrate distance of 40 mm.

SEM micrographs, AFM images and XRD spectra of V_xO_y thin films prepared at various oxygen pressures for a target-substrate distance of 40 mm are shown in Figures 6.1, 6.2 and 6.3, respectively. At high oxygen pressures (0.10 and 0.20 mbar), we observed the formation of nano-rods and a mixed structure of nano-particles and nano-plates (Figure 6.1). More details of the nano-structures were observed in AFM images, as shown in Figure 6.2. Large nano-plates and grains were observed for the 0.10 mbar sample while nano-rods and particles were observed for the 0.20 mbar sample. The thin films are homogeneous (0.20 mbar) and rough (0.10 mbar) according to the AFM analysis with the root mean square roughness of 10.3 nm and 105 nm, respectively.

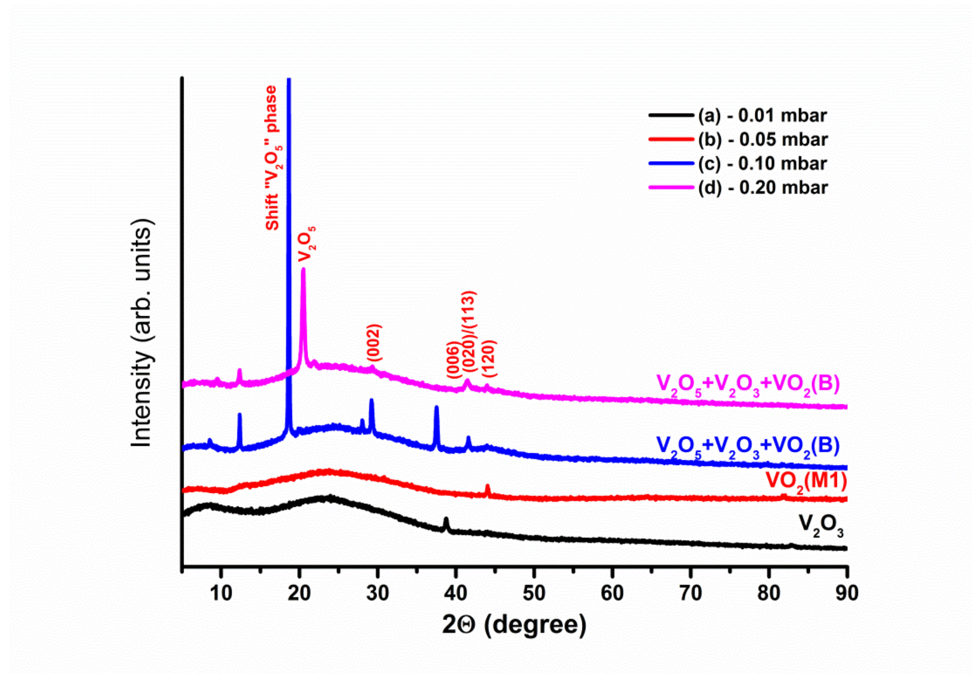

Figure 6.3: XRD spectra of thin films prepared at various oxygen pressures for target-substrate distance of 40 mm.

The XRD spectra show that the thin films (0.10 and 0.20 mbar) comprise a mixture of V_xO_y phases, such as, highly-oriented orthorhombic pentoxide (V_2O_5) phase (space

group: PmmnE, JCPDS No. 001-0359), and minor phases of rhombohedral vanadium trioxide (V_2O_3) (space group: R-3c, JCPDS No. 001-1293) as shown in Figure 6.3. The presence of V_2O_5 and V_2O_3 phases is likely due to the influence of the plasma plume dynamics: at high oxygen pressure there is a high degree of interaction between the oxygen and plasma plume species resulting in the formation of a shocked layer, where highly reactive atomic oxygen is produced and oxygen enrichment in the synthesized films is expected.

Amoruso *et al.* [6.7] observed similar finding while investigating the effect of ambient gas on the expansion dynamics of the plasma plume generated by XeF excimer laser ablation of a $LaMnO_3$ target by using fast photography and optical emission spectroscopy. Their optical emission spectroscopy analysis shows that oxides are mainly formed during the interaction of the plume with the background gas. In particular, oxides are efficiently produced when a shock-wave like propagation stage is achieved. We observed a shift in the XRD peaks from 19° to 20° (identified as V_2O_5 phase) for 0.10 mbar and 0.20 mbar, respectively as indicated in Figure 6.3. This could be due to the increase of oxygen pressure from 0.10 to 0.20 mbar. At low oxygen pressures (0.05 and 0.01 mbar), mixed nano-structures (nano-plates and nano-fibres) and smooth structures, respectively, are observed in Figure 6.1. AFM images indicate the structures in more details in Figure 6.2. Mostly smooth surface together with nano-structures are observed for 0.01 mbar samples in Figure 6.1. Mostly nano-fibres and few nano-plates are observed for 0.05 mbar sample in Figure 6.1. The thin films are homogeneous according to the AFM images with the root mean square roughness of 9.83 nm (0.05 mbar) and 10.7 nm (0.01 mbar), respectively. Here the XRD spectra

indicate the presence of mixed V_xO_y phases: highly oriented monoclinic rutile-type VO_2 (M1) phase (JCPDS No. 44-0252) and minor V_2O_3 phase (JCPDS No. 001-1293) and a broad peaks at around 20° to 30° which is introduced by the Corning glass substrate (Figure 6.3). These V_xO_y phases correspond well with the plasma plume study: as indicated that at low oxygen pressure there is insufficient oxygen-plasma interaction to produce oxygen-enriched films as shown in Figures 4.2 (a) and 4.2 (b).

The formation process of the surface morphology of PLD V_xO_y as a function of the oxygen pressure and target-substrate distance can be described as follows: the mechanism of the formation of the V_xO_y surface morphology starts when the pulsed laser heats and vaporizes the target material [6.8, 6.9]. The collisions take place between the oxygen molecules and the ablated species depending on the amount of oxygen pressure in the chamber. This results in the condensation and formation of nano-particles in the gas phase [6.9]. These nano-particles migrate to the substrate surface, due to the ad-atom mobility with the energy supplied via substrate heating as given in Figure 6.2 (for 0.01 mbar and AFM image). At this oxygen pressure, there was not enough interaction between the ablated species and the oxygen molecules for the nano-particles to increase in dimension. Due to this, smooth surface morphology together with nano-particles was produced as shown in Figures 6.1 and 6.2 for 0.01 mbar. As the oxygen pressure was increased the dimension of the nano-particles also increased, due to the fact that the interaction between the ablated species and oxygen molecules increases and the plasma plume becomes bigger. The plasma plume splitting and the formation of the shock layer at the edge of the plasma plume results in an increase in the number of nano-particles arriving at the substrate. Because there is

sufficient thermal energy via the substrate temperature (600 °C), these nano-particles aggregate with each other to form nucleation centres. The aggregation becomes larger with more nano-particles on the surface and there is an increase of the nano-structure's dimension. Due to these factors, nano-fibres, nano-plates and nano-rods surface morphology were produced as shown in Figure 6.1 (for 0.05, 0.1 and 0.2 mbar).

Wang *et al.* [6.10] synthesized similar V_2O_5 nano-rods by heating in air at ~500 °C a V_2O_3 thin film deposited on a silicon substrate. It was oxidized into V_2O_5 and started to transform into nano-rods. These results correspond very well with the V_2O_5 deposited in this study. Their V_2O_5 nano-rods could emit intense visible light, which is ascribed to formation of defects during the oxidation process. Zou *et al.* [6.11] grew β-V_2O_5 nano-rods by heating in oxygen an amorphous V_2O_5 thin film deposited on glass substrate. They suggested that surface diffusion played an important role in the growth process of nano-rods. Since the post-annealing temperature is quite high, a high degree of surface mobility is expected for the annealing or synthesis process in oxygen gas, thus favouring the growth of nano-rods. In this study, V_2O_5 nano-rods were synthesized by PLD with the Corning glass substrate heated to 600 °C. We believe the V_2O_5 nano-rods synthesized in this study follow the same growth mechanisms described by Zou *et al.* [6.11]. It is known that during the process of solid state growth for elongated nano-materials, from initial nano-particles or powders surface diffusion phenomena are common [6.12]. These V_2O_5 nano-rods were deposited beyond the stopping distance of the plasma plume (see Figure 4.3 in Chapter 4) and we believe this may have played an important role on the nano-rods growth mechanisms. In comparison, thin films grown

at the plasma plume stopping distance possess stoichiometry close to the target material, in this case VO_2 [6.13].

B. Optical Switching Properties

After optimizing the oxygen pressure for the growth of monoclinic rutile-type VO_2 (M1), determined to be 0.05 mbar, the effect of target-substrate distance d on the thin film phase and structure is investigated by increasing this distance to 50 mm. The deposition time was also increased to 15 minutes to increase the thin film thickness. A mixture of nano-structures (nano-fibre and nano-plates) for thin film deposited at d = 40 mm and nano-particles (nano-fibres and large grains) for d = 50 mm were found (Figure 6.4). The thin film deposited at d = 40 mm is homogeneous with the root mean square of 9.83 nm while the thin film deposited at d = 50 mm is rough with root mean square of 18.7 nm, according to the AFM images in Figure 6.5. XRD spectra indicate monoclinic rutile-type VO_2 (M1) phase and monoclinic VO_2 (B) (Space group: C2/m, JCPDS No: 31-1438) as given in Figure 6.6. The SEM and XRD results indicate that it is possible to optimize phases by varying the target-substrate distance.

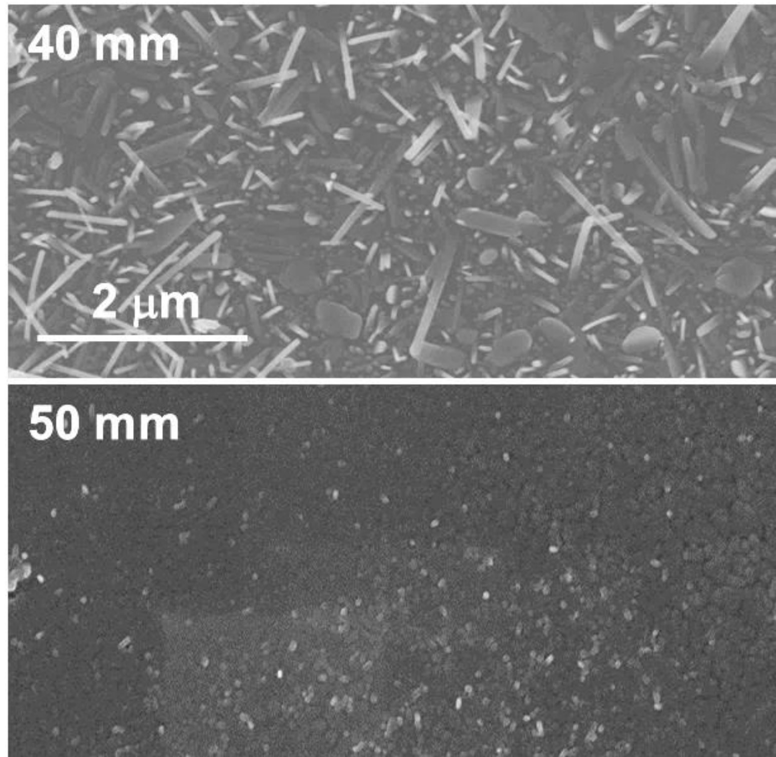

Figure 6.4: SEM micrographs of thin films prepared under 0.05 mbar oxygen pressure for target-substrate distance of 40 and 50 mm. Scale for all the micrographs is 2 μm.

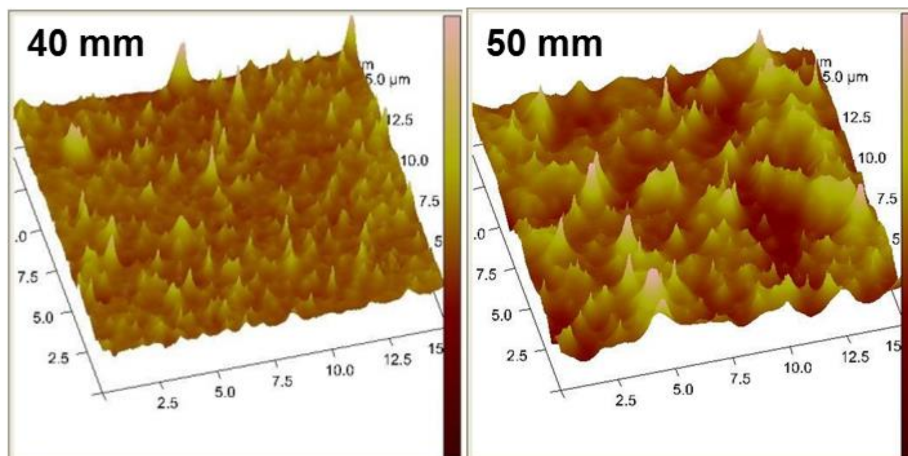

Figure 6.5: AFM images of thin films prepared under 0.05 mbar oxygen pressure for target-substrate distance of 40 and 50 mm.

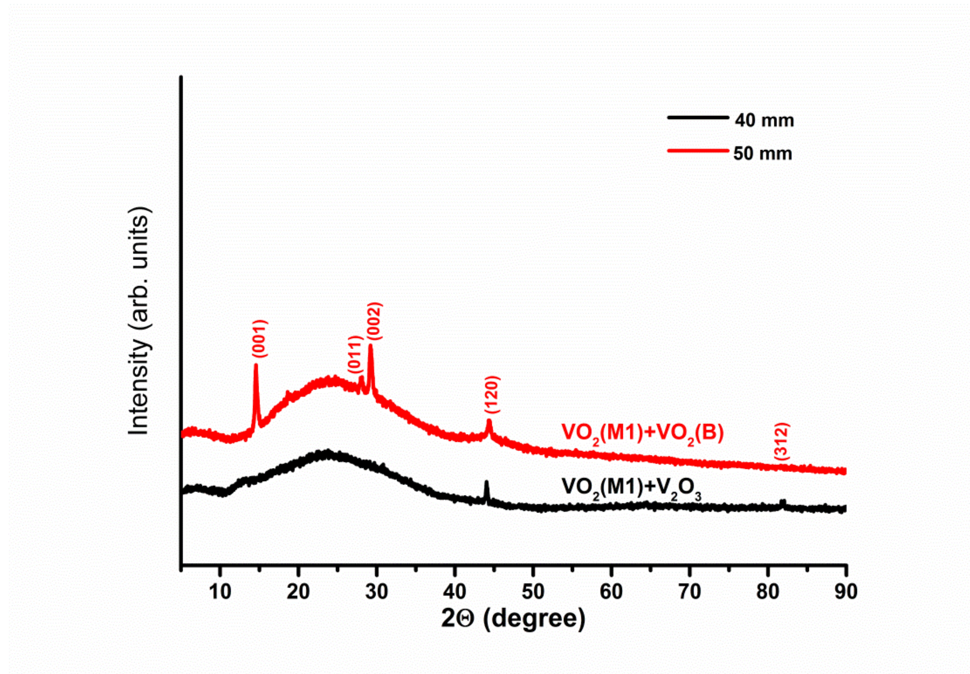

Figure 6.6: XRD spectra of thin films prepared under 0.05 mbar oxygen pressure for target-substrate distance of 40 and 50 mm.

UV-Vis-NIR spectrophotometer is useful in revealing the optical switching properties of VO_2 (M1) from the room temperature monoclinic structure to a tetragonal rutile-type structure at above 68 °C [6.14]. Wavelength dependent transmittance was measured in the range 300 – 2500 nm temperature cycling from 25 °C to 100 °C corresponding to semiconductor and metallic states of VO_2 film. Transmittance as a function of a temperature measured at 2.5 μm, a wavelength at which most of the samples show the largest contrast in transmittance on switching. The MIT temperature was obtained in this study as the minimum of the derivative of the temperature dependence of transmittance [6.15].

Figure 6.7 and Figure 6.8 indicate change of the transmittance as a function of wavelength and temperature for thin films prepared at 0.05 mbar for target-substrate distances of 40 and 50 mm, respectively. The graphs show a 34% and 42% transmittance for thin film deposited at 0.05 mbar for 40 mm and 50 mm, respectively. The reason for the dissimilarity in the temperature-dependent transmittance of the two thin films is likely due to different composition of phases of the vanadium oxides previously identified by XRD. We observed poor phase transition in sample d = 40 mm, while we obtained a good phase transition for sample with d = 50 mm (Figures 6.7 and 6.8, respectively). We successfully optimised the monoclinic rutile-type VO_2 (M1) by varying the target-substrate distance as shown in Figure 6.8 and we reduced the phase transition temperature from 68 °C to 60.9 °C. It has been observed that the majority of reports on VO_2 (M) nano-particles deposition using PLD could only be synthesized after post-annealing [6.16]. The first report of room-temperature growth of VO_2 by PLD without post-annealing is by Maaza *et al.* [6.17] and the deposited films showed rather sharp phase transition at around 70 °C, however, thus far it has not been reproduced by any other group yet. We have shown that a high quality monoclinic rutile-typed VO_2 (M1) can be deposited on the Corning glass at the substrate temperature of 600 °C. Kim *et al.* [6.18] have also reported the deposition of high quality VO_2 films on sapphire by PLD at high temperature without post-annealing. In this study, we have shown the link between the plasma plume expansion on the growth and phase of the VO_2 nano-particle.

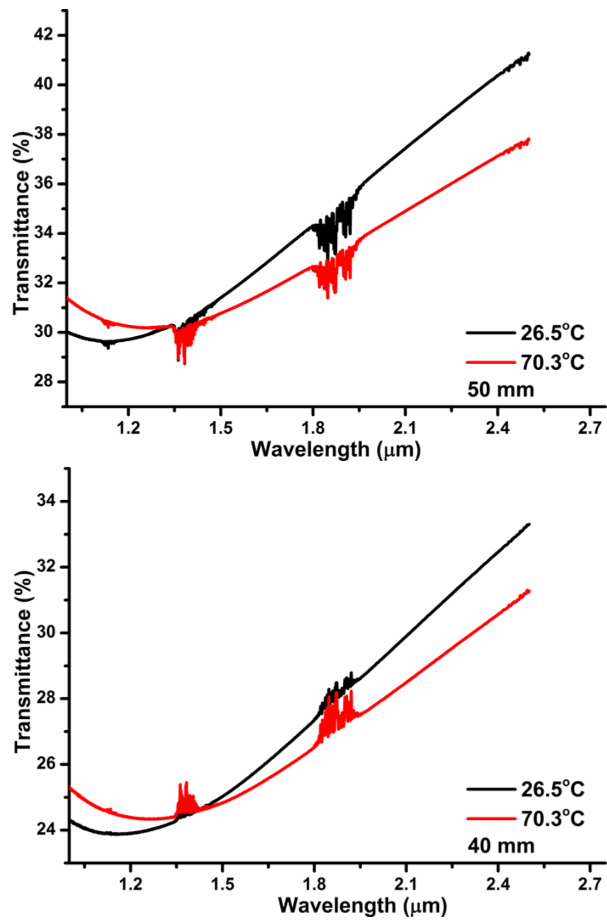

Figure 6.7: Change of transmittance at different wavelengths for 26.5 °C and 70.3 °C for a thin film prepared at 0.05 mbar for target-substrate distances of 40 and 50 mm.

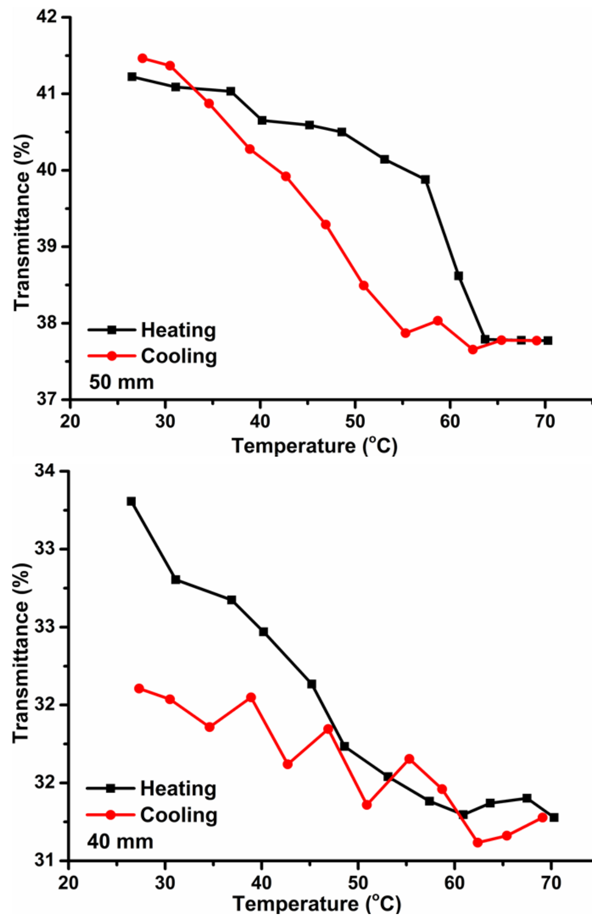

Figure 6.8: Change of transmittance under temperatures at 2.5 μm for a thin film prepared at 0.05 mbar for target-substrate distances of 40 and 50 mm.

The most important stage during the PLD process is the interaction between the plasma plume species and the background gas. Chaoui *et al.* [6.19] measured the oxygen incorporated in the thin films to be 54% and 46% of oxygen originates from the target and background gas, respectively. Roman *et al.* [6.120] established that the oxygen is only incorporated into the thin films during the growth step and measured that 45% of the oxygen originated from the background gas. They also showed that the main mechanism of oxygen incorporation corresponds to the dissociation of molecular oxygen absorbed at the surface, leading to the formation of very reactive atomic oxygen

which is further injected in the thin films. The dissociation of molecular oxygen take place during the plasma plume expansion when as shock layer is produced [6.21] or on the substrate surface as a result of the interaction with the high flux of species coming from the target. The molecular oxygen could be incorporated directly into growing thin film or first form oxides before being incorporated. In this study, the degree of interaction between the plasma plume species and oxygen molecules is lower at 40 mm and higher at 50 mm. This means more oxygen dissociation and incorporation occurred at d = 50 mm. And this also could be accentuated by a strong shock effect and a lower re-pulverization effect. The latter is more pronounced for the lighter element of atomic oxygen. The maximum of oxide molecules is produced at a distance where the plasma plume loses all its kinetic energy, the so-called plasma plume stopping distance where generally the thin films stoichiometry was closed to the target one [6.13]. These phenomena explain the formation of the sub-stoichiometric phases of VO_2, V_2O_3 for 40 mm and VO_2 (M1), VO_2 (B) for 50 mm, as well as all the sub-stoichiometric phases of V_xO_y in this work.

6.3 Conclusions

The expansion dynamics of a laser ablation plume produced during KrF excimer laser irradiation of a VO_2 pellet in oxygen ambient has been investigated using a fast ICCD camera. The time evolution of the plume images has enabled observations of the plume propagation behaviour under different background gas pressure, from vacuum to few mbars. The experimental findings reveal several interesting features which are of general character and interest, with the temporal dynamics found to be dependent on the oxygen pressure. Thin films deposited with these plasma conditions revealed the

presence of V_xO_y nano-rods, nano-plates and nano-fibres. The V_2O_3 phase was produced at low oxygen pressure (0.01 mbar), while VO_2 (M1) and VO_2 (B) nano-rods phases were deposited at 0.05 mbar oxygen pressure. The plume expansion and the V_xO_y thin films analysis shows that oxides are mainly formed during the interaction of the plume with the background gas. In particular, high oxides thin films are efficiently produced when a shock-wave like propagation stage is achieved. A transition temperature of around 61 °C has been measured for a sample deposited at an oxygen pressure of 0.05 mbar oxygen pressure. We showed a proof of concept, that VO_2 (M1) film growth is possible only under particular conditions and we are able to precisely control them as revealed by comprehensive structural and optical characterisation of the film grown, and through study of plume dynamics which behaves similar to other studies for other types of materials. This improved knowledge of the plume characteristics provided by this study may open up the route to search for the more suitable experimental conditions for the growth of any complex oxide material, depending on its specific criticalities.

References

6.1 U. Schwingenschlogly, V. Eyert, "The vanadium magneli phases $V_{(n)}O_{(2n-1)}$" Ann. Phys. **13**, 475 (**2004**).

6.2 S.R. Popuri, A. Artemenko, C. Labrugere, M. Miclau, A. Villesuzanne, M. Pollet, "VO_2 (A): Reinvestigation of crystal structure, phase transition and crystal growth mechanisms", J. of Solid State chem. **213**, 79 (**2014**).

6.3 R.K. Singh, J. Narayan, "Pulsed-laser evaporation technique for deposition of thin films: Physics and theoretical model" Phys. Rev. B **41**, 8843 (**1990**).

6.4 B.E. Warren, X-Ray Diffraction, Addision-Wesley, Reading, MA (**1969**).

6.5 M.T. Postek, K.S. Howard, A.H. Johnson, K.L. McMichael, Scanning Electron Microscopy: A student's Handbook, Ladd Research Ind., Inc. Williston, VT. (**1980**).

6.6 R.N. Jagtap, A.H. Ambre, "Overview literature on atomic force microscopy (AFM): Basics and its important applications for polymer characterisation" Indian J. of Eng. And Mat. Sci. **13**, 368 (**2006**).

6.7 S. Amoruso, A. Sambri, X. Wang, "Plume expansion dynamics during laser ablation of manganates in oxygen atmosphere" Appl. Surf. Sci. **253**, 7696 (**2007**).

6.8 N. Rama, M.S. Ramachandra Rao, "Synthesis and study of electrical and magnetic properties of vanadium oxide micro and nano-sized rods grown using pulsed laser deposition technique" Solid State Comm. **150**, 1041 (**2010**).

6.9 R.Q. Guo, J. Nishimura, M. Matsumoto, D. Nakamura, T. Okada, "Catalyst-free synthesis of vertically-aligned ZnO nano-wires by nano-particles-assisted pulsed laser deposition" Appl. Phys. A **93**, 843 (**2008**).

6.10 Y. Wang, Z. Li, X. Sheng, Z. Zhang, "Synthesis and optical properties of V_2O_5 nano-rods", J. of Chem. Phys. **126**, 164701 (**2007**).

6.11 C.W. Zou, X.D. Yan, J. Han, R.Q. Chen, W. Gao, "Microstructures and optical properties of β-V_2O_5 nano-rods prepared by magnetron sputtering", J. Phys. D: Appl. Phys. **42**, 145402 (**2009**).

6.12 A.M. Glushenkov, V.I. Stukachev, M.F. Hassan, G. Kuvshinov, "A Novel approach for real mass transformation from V_2O_5 particles to nano-rods", Cryst. Growth Des. **8**, 3661 (**2008**).

6.13 P.R. Wilmott, J.R. Hubert, "Pulsed laser vaporization and deposition" Rev. Mod. Phys. **72** (1), 315 (**2000**).

6.14 R.J. Morin, "Oxides which show a metal-to-insulator transition at the Neel temperature", Phys. Rev. Lett. **3**, 34 (**1959**).

6.15 A.R. Begishev, G.B. Galiev, A.S. Ignat'ev, V.G. Mokerov, V.G. Poshin, "Influence of deviations from the crystal lattice periodicity on the semiconductor-metal phase transition in vanadium dioxide", Sov. Phys. Solid State **20** (6), 951 (**1978**).

6.16 J. Nag, R.F. Haglund Jr., "Synthesis of vanadium dioxide thin films and nano-particles" J. Phys.: Condens. Matter **20**, 26401 (**2008**).

6.17 M. Maaza, K. Bouziane, J. Maritz, D.S. McLachlan, R. Swanepool, J.M. Frigerio, M. Every, "Direct production of thermochromic VO_2 thin film coatings by pulsed laser ablation" Opt. Mater. **15**, 41 (**2000**).

6.18 D.H. Kim, H.S. Kwok, "Pulsed laser deposition of VO_2 thin films" Appl. Phys. Lett. **65**, 3188 (**1994**).

6.19 N. Chaoui, E. Millin, J.F. Muller, P. Ecker, W. Bieck, H.N. Migeon, "Perovskite lead titanate PLD thin films: study of oxygen incorporation by ^{18}O tracing technique", Mater. Chem. Phys. **59**, 114 (**1999**).

6.20 R. Gomez-San Roman, R. Perez Casero, C. Marechal, J.P. Enard, J. Perriere, "^{18}O isotopic tracer studies of the laser ablation of $Bi_2Sr_2Ca_1Cu_2O_8$", J. Appl. Phys. **80**, 1787 (**1996**).

6.21 S. Amoruso, M. Angelon, G. Balestrino, N. Boggio, R. Bruzzese, P.G. Medaglia, A. Tebano, M. Vitiello, X. Wang, "Optimization of $La_{0.7}Ba_{0.3}MnO_{3-\delta}$ complex oxide laser ablation conditions by plume imaging and optical emission spectroscopy" Appl. Surf. Sci. **247**, 64 (**2005**).

Chapter 7

Phase-Selective Vanadium Dioxide (VO_2) Nano-structured Thin Films by Pulsed Laser Deposition

While several synthesis methods [7.1, 7.2, 7.3] have been used to produced vanadium dioxide (VO_2), pulsed laser deposition (PLD) [7.4, 7.5, 7.6, 7.7] is known for its rational fabrication of smart and functionally high quality metal oxide particulate thin films and coatings. Several deposition parameters need to be optimized in order to deposit monoclinic rutile-type (VO_2) (M1) including gas pressure [7.8], nature of substrate [7.9], substrate temperature [7.10] and nature of target [7.11]. Several target materials and substrates have been use to deposit VO_2 (M1), however literature indicates that more often than not, as-deposited V_xO_y films were subsequently annealed in various atmospheres in order to improve the VO_2 stoichiometry [7.12, 7.13, 7.14] and non-glass substrates have been employed [7.15]. In contrast, VO_2 thin films grown on the glass substrates have not been extensively studied with only a few reports over decades [7.15, 7.16, 7.17].

The plasma plume expansion (in Chapters 4 and 5) and the V_xO_y thin films (in Chapter 6)' analysis shows that oxides are mainly formed during the interaction of the plume with the background gas. In this chapter, then we show that it is possible to improve the VO_2 composition by investigating the link between the V-O plume and the VO_2 stoichiometry in a PLD process without the need of post-deposition annealing. The plasma plume expansion dynamics of an ablated VO_2 target was investigated using fast-imaging technique under a range of oxygen partial pressures and under vacuum, and correlated to two well-known plasma propagation models as discussed in Chapters 4

and 5. By optimization of the parameters we report high quality VO_2 (M1) nano-particles on a glass substrate, without post-deposition annealing. Samples demonstrate a reversible MIT at ~43 °C, without any doping, paving the way to switchable transparency in optical materials at room temperature.

7.1 Experimental Set-up

The schematic diagram of the experimental setup used to synthesize V_xO_y thin films in this chapter is already discussed in Chapter 4 and is shown in Figure 4.1. V_xO_y thin films were deposited on Corning glass substrate under the same conditions/parameters of the oxygen pressure (0.01 and 0.05 mbar) and laser parameters (laser fluences = 2 Jcm^{-2}, pulse repetition rate = 5 Hz) used for the plasma and plasma plume species studies (Chapter 4 and 5). The substrate temperature was set to be 500 °C and the deposition time was 10 minutes. The target to substrate distance was determined using the plasma plume propagation graph (Chapter 4).

7.2 Results and Discussion

A. Plume Dynamics Results

It is well known that the plasma dynamics plays an important role in growing high-quality complex oxide thin films when target-substrate distance (d) is optimised with respect to the oxygen pressure (P) in PLD [7.18]. Beyond a certain target-substrate distance (d), the plasma flux loses its unidirectional velocity, scatters and thermalizes and this distance provides the optimum conditions for film growth [7.19, 7.20]. As discussed in Chapter 4, the plasma plume in this study was correlated using two well-known plasma plume models. Here in this chapter only the point-blast-wave model

fitted in the plasma plume propagation graph was used to determine the deposition parameter (Figure 7.1). In this study, we showed that at optimum conditions for VO_2 (M1) thin film growth is below certain oxygen level and when the plume starts slowing down (slow shock) as indicated in Figure 7.1. Point A and B in Figure 7.1 satisfy this condition.

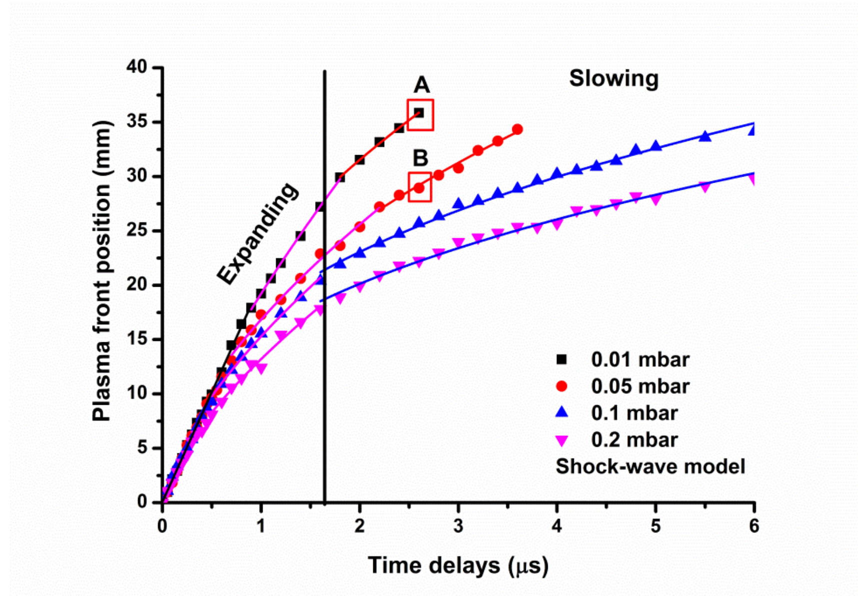

Figure 7.1: Propagation of plasma plume front position for different oxygen gas pressure fitted with the point-blast-wave which is indicating a free-expansion (black), plane-wave front (magenta), cylindrical-wave front (red) and spherical-wave front (blue) propagation.

B. Structural Analysis

Atomic Force Microscopy (AFM), Scanning Electron Microscopy (SEM) and X-Ray Diffraction (XRD) were used to characterize the surface microstructures and to identify the vanadium oxide phases of the thin films. Figure 7.2 indicates a XRD pattern of single crystalline structure of the monoclinic (M1) phase VO_2 deposited on a Corning glass.

The prominent XRD peak is occurring around 2θ = 27.81°, corresponding to (011) diffraction plane, along with other three weak diffraction peaks: (001) [7.21] (JCPDS No. 72-1278), (211), (022) which confirms the monoclinic VO_2 film (space group: $P2_1/c$. JCPDS No. 44-0252).

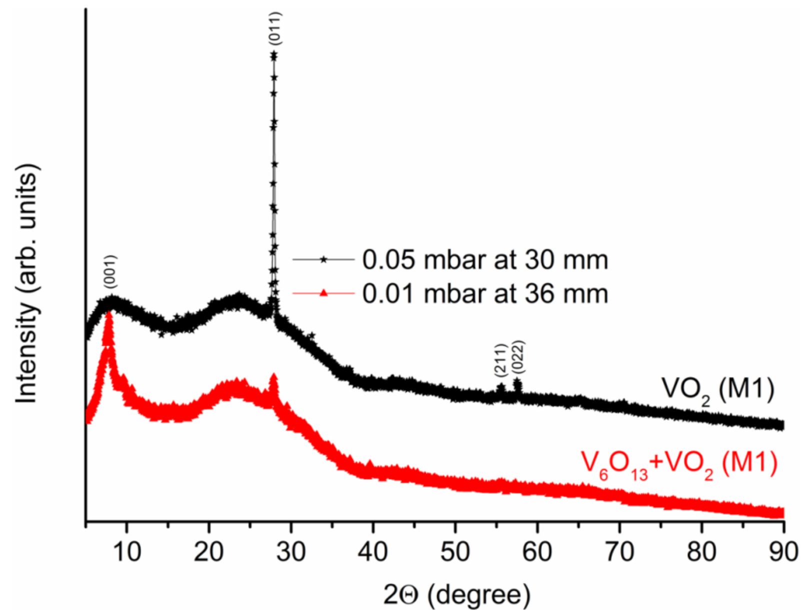

Figure 7.2: XRD spectra of VO_2 (M1) thin films deposited under low oxygen gas pressure (0.05 and 0.01 mbar) and target-substrate distance for 30 and 36 mm and substrate temperature of 500 °C.

We deposited a pure monoclinic rutile-type VO_2 (M1) more single crystalline nature of the film for target-substrate distance of a 30 mm for 0.05 mbar oxygen pressure as indicated by XRD patterns in Figure 7.2. However mixed phases were deposited for sample prepared at 0.01 mbar oxygen pressure for target-substrate of 36 mm, a monoclinic rutile-type VO_2 (M1) phase around 2θ = 27.81° (011) and 2θ = 7.8° which has identified as V_6O_{13} (001) [7.21] (JCPDS No. 72-1278) as indicated by XRD patterns in Figure 7.2. The XRD patterns in Figure 7.2 indicated that the VO_2 (011) peak emerges

from a broad peak. This broad peak is attributed to the glass substrate. The XRD results indicate that the more single crystalline VO_2 film formed on the amorphous substrate (thus glass) surface and showed a preferential orientation along the (011) plane located at 27.81° on the XRD patterns.

Chin *et al.* [7.22] made similar findings when they were attempting to control the crystallographic orientation of VO_2 on glass. Lafane *et al.* [7.23] also made similar findings when they obtained a highly (011) oriented VO_2 on Corning glass at low pressures in the range of 0.004 – 0.02 mbar by PLD. These results are in good agreement with the plasma propagation graph in Figure 7.1 (more information in Chapter 4). This is due to the fact that these oxygen pressures are close to vacuum where the plasma plume propagates relatively free and there is not enough interaction in these pressure-distance couples to develop the shocked layer. The deposition target-substrate distance used in this study for both oxygen pressures correspond to the planar expansion regime of the plasma plume to be more determinant to qualify the slow shock as shown in Figure 7.1 (more information in Chapter 4). Highly reactive atomic oxygen is produced in the shock layer and oxygen enrichment in the deposited films is expected. Generally according to plasma dynamics principle, the target stoichiometry is reproduced close to the plume stopping distance [7.24]. However the deposition target-substrate distances used in this study, are expected to yield small vanadium valence, but the target stoichiometry was produced at the target-substrate distance less than the stopping distance. It can be speculated that the substrate temperature enhances the surface mobility of the adatoms and thereby the surface reactivity. Furthermore, the target-substrate distance is short, where one can expect a high instantaneous deposition rate that fixes oxygen atoms before they can desorb. The

high quality of the VO_2 thin film prepared at 0.05 mbar (30 mm) is evident from the relatively small full width half-maximum (FWHM) of ~0.22° of this diffraction peak (011) as shown in Figure 7.2.

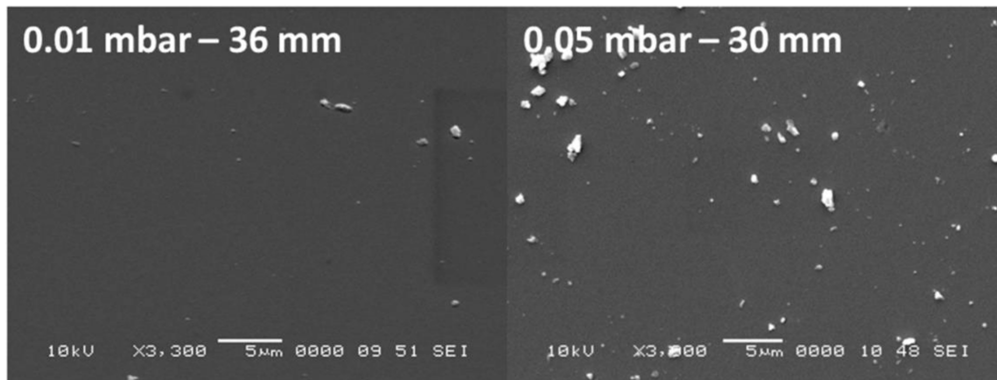

Figure 7.3: SEM micrographs of VO_2 (M1) thin films deposited under low oxygen gas pressure (0.05 and 0.01 mbar) and target-substrate distance for 30 and 36 mm and substrate temperature of 500 °C.

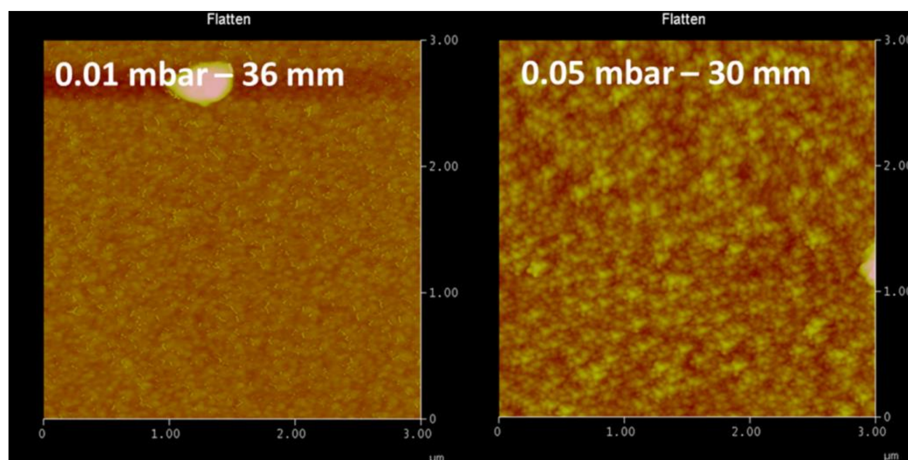

Figure 7.4: AFM images of VO_2 (M1) thin films deposited under low oxygen gas pressure (0.05 and 0.01 mbar) and target-substrate distance for 30 mm and 36 mm and substrate temperature of 500 °C.

The corresponding SEM micrographs and 3 x 3 µm AFM images for both thin films (0.05 and 0.01 mbar) reveal nano-particles and smooth surfaces as given in Figures 7.3 and 7.4, respectively. The AFM images show that the thin films are homogeneous and particulate with high surface coverage with root mean square (rms-) roughness of ~8.5 nm for 0.01 mbar (36 mm) and ~2.7 nm for 0.05 mbar (30 mm). The particle sizes are ~0.06 µm for 0.01 mbar (36 mm) and ~0.1 µm for 0.05 mbar (30 mm), according to the AFM images.

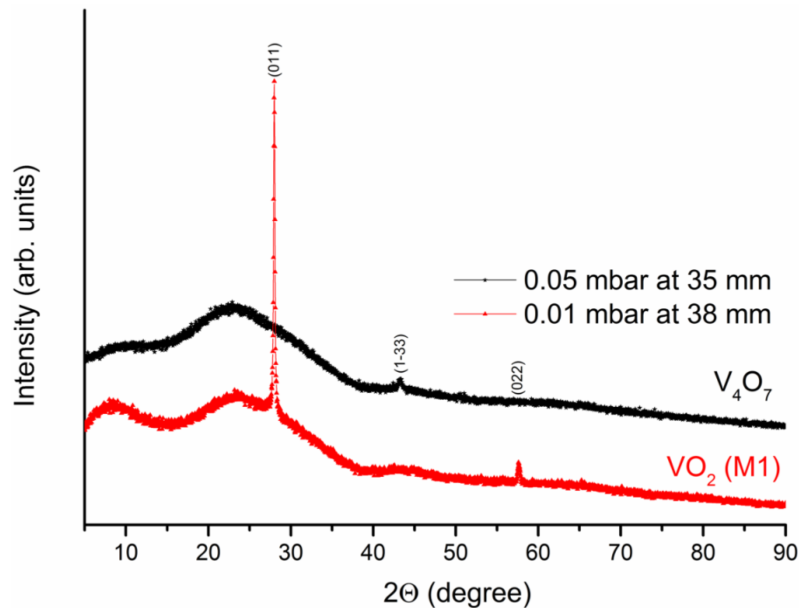

Figure 7.5: XRD spectra of V_xO_y thin films deposited under low oxygen gas pressure (0.05 and 0.01 mbar) and target-substrate distance for 35 mm and 38 mm and substrate temperature of 500 °C.

We successfully optimized the VO_2 (M1) thin film prepared at 0.01 mbar oxygen pressure by increasing the target-substrate distance from 36 mm to 38 mm as indicated by XRD pattern in Figures 7.2 and 7.5, respectively. Figure 7.5 indicates pure monoclinic rutile-type VO_2 (M1) phase for target-substrate distance for 38 mm prepared at 0.01

mbar oxygen pressure. Even though the oxygen partial pressure was controlled within the range in which the pure VO_2 phase could be formed on the glass substrate, the crystalline orientation of vanadium oxide (V_xO_y) thin films was drastically changed for thin film prepared under 0.05 mbar oxygen pressure at 35 mm target-substrate distance as XRD pattern revealing $2\theta = 43.48°$ peak angle as V_4O_7 (1-33) (JCPDS No. 72-1718) as given in Figure 7.5. The high quality of the VO_2 thin film prepared at 0.01 mbar (38 mm) is evident from the FWHM of ~0.22 of this diffraction peak (011) as given in Figure 7.5.

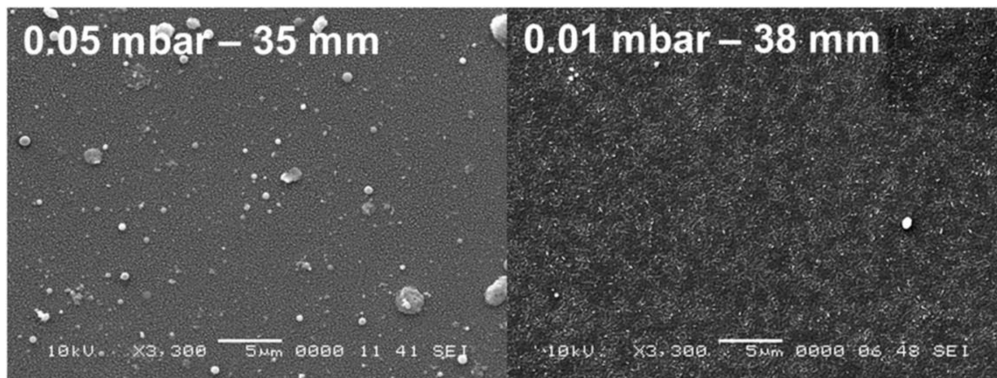

Figure 7.6: SEM micrographs of V_xO_y thin films deposited under low oxygen gas pressure (0.05 and 0.01 mbar) and target-substrate distance for 35 mm and 38 mm and substrate temperature of 500 °C.

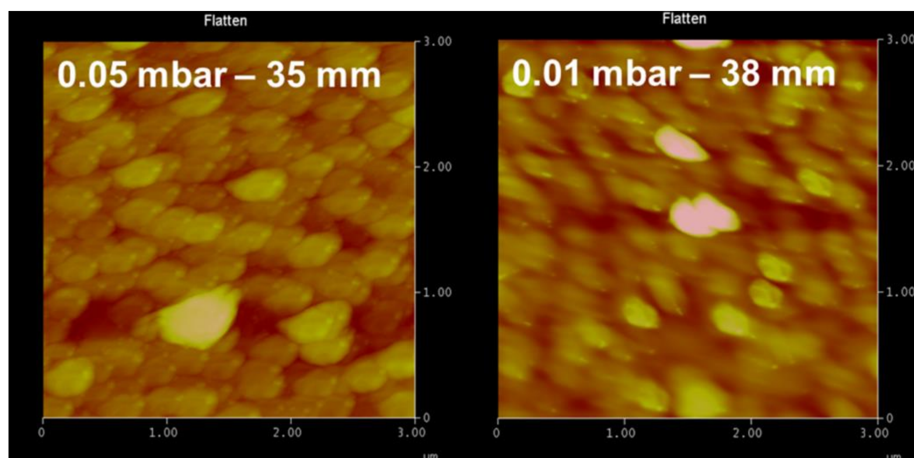

Figure 7.7: AFM images of V_xO_y thin films deposited under low oxygen gas pressure (0.05 and 0.01 mbar) and target-substrate distance for 35 mm and 38 mm and substrate temperature of 500 °C.

The corresponding SEM micrographs and AFM images indicate nano-particles as given in Figures 7.6 and 7.7 for both thin films, respectively. The AFM images show that the thin films are homogeneous with root mean square roughness of ~9.9 nm for 0.05 mbar and ~21.2 nm for 0.01 mbar, respectively. As the target-substrate distance increases, an increase in the grain size of the nano-particles was observed as indicated in Figures 7.4 and 7.7. The grain sizes according to the AFM analysis is in the same order of ~0.3 μm for both thin films. The well-known Debye's formula [7.25] was used to estimate the grain sizes of the three VO_2 thin films using the XRD peak of 27.81° (011), giving 27 nm (0.01 mbar – 36 mm), 41 nm (0.01 mbar – 38 mm) and 39 nm (0.05 mbar – 30 mm). The grain sizes for samples prepared on 0.01 mbar oxygen pressures indicates that as target-substrate increases the grain size increases as well. Whereas samples prepared on 0.01 mbar (38 mm) and 0.05 mbar (30 mm) have the same grain size. Both these were observed in AFM images as well (Figures 7.4 and 7.7).

C. Electrical and Optical Properties

UV-Vis-NIR transmittance spectrophotometer and four-point probe are useful in measuring the switching properties of VO_2 from the room temperature monoclinic structure to a tetragonal rutile-type structure at above 68 °C [7.26]. Wavelength dependent transmittance was measured in the range 300 – 2500 nm at temperature cycling from 30 °C – 100 °C corresponding to semiconductor and metallic states of VO_2 film. Transmittance as a function of a temperature measured at 2500 nm, a wavelength at which most of the samples show the largest contrast in transmittance on switching. Sheet resistance of the films as a function of temperature was measured by four point-probe method in the temperature cycling from 25 – 100°C corresponding to semiconductor and metallic phases of the films.

There are several methods used in the literature to determine the MIT temperature such as midpoint hysteresis loop [7.27], derivative of the heating and cooling profiles of the resistance/transmittance allows the estimation of average value of the MIT temperature [7.6, 7.7] and the minimum of the derivative of the temperature dependence of transmittance/resistance [7.28] among others. The MIT temperature was obtained in this study as the minimum of the derivative of the temperature dependence of transmittance/resistance.

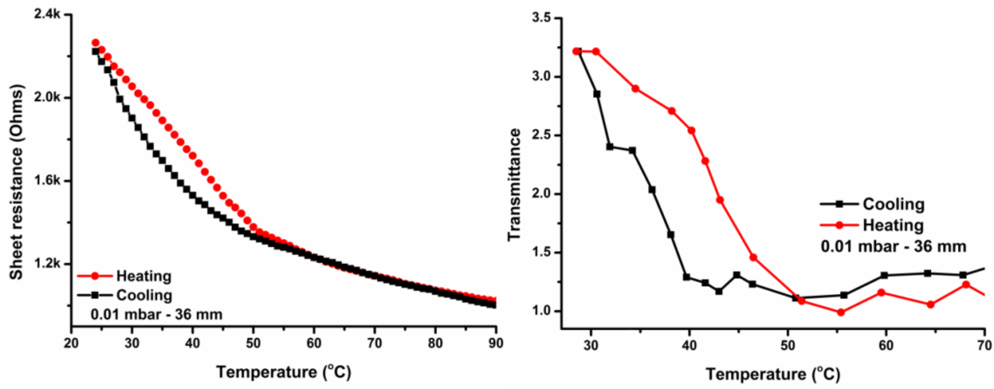

Figure 7.8: Change of the resistance and transmittance of a thin film under temperature cycling prepared at 0.01 mbar oxygen pressure for target-substrate distance of 36 mm.

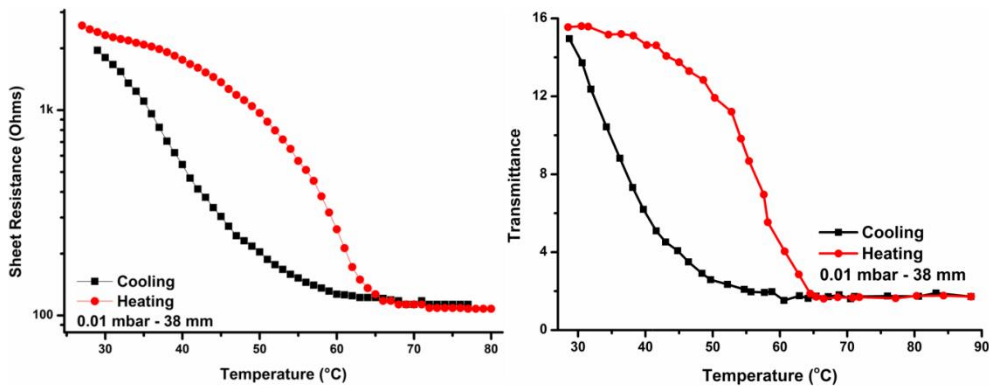

Figure 7.9: Change of the resistance and transmittance of a thin film under temperature cycling prepared at 0.01 mbar oxygen pressure for target-substrate distance of 38 mm.

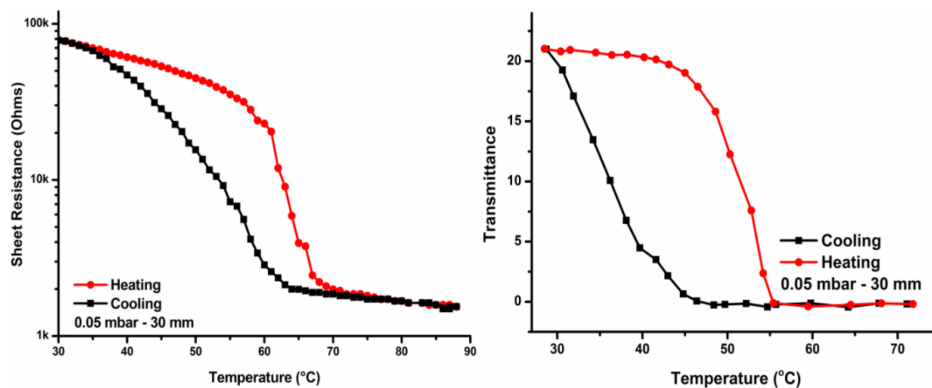

Figure 7.10: Change of the resistance and transmittance of a thin film under temperature cycling prepared at 0.05 mbar oxygen pressure for target-substrate distance of 30 mm.

Table 7.1: Electrical and optical switching properties parameter.

Samples	Grain size (nm)	MIT temperature (°C)	Hysteresis width (°C)
0.01 mbar – 36 mmm	27	43	12
0.01 mbar – 38 mm	41	57.3	24
0.05 mbar – 30 mm	39	52 – Optical	17
		63 – Electrical	11.2

The change of the resistance and transmittance of a thin film under temperature cycling prepared at 0.01 mbar (36 and 38 mm) and 0.05 mbar for 30 mm are shown in Figures 7.8 to 7.10, respectively. From electrical and optical properties point of view, both the VO_2 (M1) thin films prepared at 0.01 mbar oxygen pressure but at varying substrate-to-target distances of 36 and 38 mm exhibit, within the error bar similar hysteresis loops in electrical resistance and optical transmittance transitions located ~43 °C and ~57.3 °C as shown in Figures 7.8 and 7.9, respectively. These transition temperatures are implying a decrease in the transition temperature of about ~25 °C and 10.7 °C, respectively. Maaza *et al.* [7.29] found similar finding when comparing the hysteresis loops in electrical resistance and optical transmittance transitions. However, the VO_2 (M1) thin film prepared at 0.05 mbar oxygen pressure (30 mm) exhibit, non-similar hysteresis loops in electrical resistance and optical transmittance transitions located ~63 °C and ~52 °C, respectively, which a decrease in the transition temperature of about ~5 °C and ~16 °C (Figure 7.10). The big difference between the electrical and optical transmittance transitions for this sample (0.05 mbar) is still to be investigated.

The VO_2 (M1) films prepared at 0.01 mbar for 36 mm, 38 mm acquired narrower and wider hysteresis loops with width of ~12 °C, ~24 °C and obtained lower phase transition temperature of ~43 °C and ~57.3 °C, respectively as indicated in Figures 7.8 and 7.9. Whereas the thin film prepared at 0.05 mbar for 30 mm obtained higher shaper phase transition in the electrical resistance hysteresis, ~63 °C with a wider hysteresis loop of ~11.2 °C as shown in Figure 7.10. In case of the optical transmittance, we obtained low phase transition, ~52 °C with a wider hysteresis loop of ~17 °C as shown in Figure 7.10 and Table 7.1.

It is known that the sharpness, shape, width, position and switching ratio of the thermal hysteresis loops of VO_2 films is determined by several factors, such as crystallinity, stoichiometry, impurities, grain size, distribution and orientation as well as interface energy [7.30 - 7.33]. The results of this study suggest that the variance of widths of thermal hysteresis loop of the VO_2 (M1) film is inferred to originate from the grain/crystallite size variation. The bigger grains result wider hysteresis and smaller grains are leading to narrower hysteresis as given in Figures 7.8 to 7.10. According to Lopez *et al.* [7.34] the smaller the grain sizes, more grain boundaries exist, which will accelerate the completion of the reversible phase transition near transition temperature, such as the thin film prepared at 0.01 mbar (36 mm) perform narrower hysteresis with a width of ~12 °C compared to a wider hysteresis of samples prepared at 0.01 mbar (38 mm) in Figures 7.8 to 7.9.

The transition temperature of all the samples in this study are lower than to that of the bulk single-crystal VO_2 which is 68 °C [7.26]. The phenomenon of the transition temperature increasing with the increase in grain size was observed in this study in all the VO_2 thin films grown at both oxygen pressures (36 mm – 0.01 mbar (grain size = 27 nm); 30 mm – 0.05 mbar (grain size – 39 nm) and 38 mm – 0.01 mbar (grain size = 41 nm)). Furthermore, the increase of the hysteresis width in these VO_2 thin films as a function of the grains sizes was also observed as shown in Table 7.1. These are in agreement with the several studies [7.35-7.36]. Figure 7.2 indicates possible impurities in VO_2 thin film prepared at 36 mm target-substrate distance for 0.01 mbar oxygen pressure from the peak angle of about 7.8° identified as V_6O_{13} and this would explain why we have observed low transmittance intensity.

Kang *et al.* [7.27] prepared a high quality VO_2 (M1) using a polymer-assisted deposition technique. They made used of a cheap inorganic vanadium (IV) precursors, polymer and tungsten ion as a doping agents. Then the spun the precursor solutions and subsequently annealing the gel films at temperature range of 300-600°C in N_2. Their samples showed excellent optical properties compared to those prepared by this study, with an integral visible transmittance of 54.5% and IR reduction of 41.5% at 2000 nm. In this study, we obtained ~22% at 2500 nm IR transmittance and ~27% at visible transmittance for sample prepared at 0.05 mbar oxygen pressure for target-substrate distance of 30 mm as given in Figure 6.10. The VO_2 film prepared by this technique doped by 1% tungsten ion exhibits a hysteresis loop centered at 54 °C with width of 16 °C, whereas in this study, we achieved MIT temperatures ~43 °C, 52 °C and 57 °C without doping and without annealing. A comparative study of the energy-saving effect

of VO_2-coated float glass and non-coated glass was conducted by Gao *et al.* [7.37] The VO_2 film was prepared by casting VO_2 and Sb: SnO_2 (ATO) nano-particles. This film indicated a phase transition temperature of ~30 °C. Their model house results show that under similar infrared irradiation the temperature difference between the two inner-rooms was significant (~9 °C), suggesting that a significant amount of irradiation was blocked. Additionally, their results show that VO_2 smart windows have a good energy-saving effect, which can be further improved by depositing a high quality VO_2 nano-particles thin film. However in this study, we offer an approach to follow for the creation of VO_2 by judicious choice of laser and plasma conditions using PLD without doping.

This study successfully synthesized and optimized a high quality VO_2 (M1) on Corning glass using PLD without further annealing. The results indicate a certain pattern to follow when one needs to deposit the VO_2 (M1) using PLD. This certain pattern points to distance-pressure scaling law [7.20]. We find that VO_2 will normally be deposited when a substrate is far away from the target (typically 30 mm to 40 mm) and when the corresponding oxygen partial pressure are low or close to vacuum as shown in Figures 7.2 and 7.5. Futhermore, in term of plasma dynamics, VO_2 will normally be deposited when the plume start slowing down (typical slow shock) and below certain oxygen partial pressure (typical close to vacuum) as shown in Figure 7.1. As mentioned earlier, the two optimized VO_2 samples were deposited at distances of planar expansion.

7.3 Conclusions

A pure monoclinic rutile-type VO_2 (M1) phase was successfully deposited at 0.05 mbar of 30 mm and 0.01 mbar of 38 mm without post-annealing on Corning glass. These VO_2 (M1) films demonstrate a reversible MIT at ~52 °C and ~57.3 °C, without any doping respectively. Whereas the VO_2 (M1) deposited at 0.01 mbar of 36 mm demonstrates a reversible MIT at ~43 °C without any doping. Our results indicate that the VO_2 will normally be deposited when the plume start slowing down (slow shock) and at below certain oxygen partial pressures. We found that by increasing the target-substrate distance, the grain size of the VO_2 (M1) nano-particles can be increased. Furthermore, the increases of the hysteresis width and transition temperature as function of the grain size were also observed. This is in agreement with several results reported in the literature. We have shown that by understanding the plasma plume propagation of the various species presents good control of the stoichiometry and grain size of the deposited nano-particle thin films is possible. There is a good agreement between the deposited vanadium oxide phases and structure with the plasma plume propagation.

References

7.1 J. Nag, R.F. Haglund Jr.,"Synthesis of vanadium dioxide thin films and nanopartilces", J. Phys.: Condens. Matter. **20**, 26401 (**2008**).

7.2 B.W. Mwakikunga, E. Sideras-Haddad, M. Maaza, "First synthesis of vanadium dioxide by ultrasonic nebula-spray pyrolysis", Opt. Mater. **29** (5), 481 (**2007**).

7.3 B.W. Mwakikunga, A. Forbes, E. Sideras-Haddad, C. Arendse, "Raman spectroscopy of WO_3 nano-wires and thermos-chromism study of VO_2 belts

produced by ultrasonic spray and laser pyrolysis techniques",Phys. Stat. Solid (a) **205**, 150 (**2008**).

7.4 P.R. Wilmott, J.R. Hubert, "Pulsed laser vaporization and deposition", Rev. Mod. Phys.**72** (1), 315 (**2000**).

7.5 B.D. Ngom, M. Chaker, A. Diallo, I.G. Madiba, S. Khamlich, N. Manyala, O. Nemraoui, R. Madjoe, A.C. Beye, M. Maaza, "Competitive growth texture of pulsed deposited vanadium dioxide nanostructures on a glass substrate", Acta Materialia **65**, 32 (**2014**).

7.6 L. Mathevula, B.D. Ngom, L. Kotsedi, P. Sechogela, T.B. Doyle, "Thermochromic VO_2 on Zinnwaldite Mica by pulsed laser deposition", Appl. Sur. Sci. **314**, 476 (**2014**).

7.7 A. Diallo, N.M. Ndiaye, B.D. Ngom, S. Khamlich, K. Talla, S. Ndiaye, N. Manyala, O. Nemaraoui, R. Madjoe, A.C. Beye, M. Maaza, "Effect of substrate temperature on the structure and the metal insulator transition in pulsed laser deposed VO_2/films on soda lime glass", J. Opt. **44** (1), 36 (**2015**).

7.8 D. Ruzmetov, S.D. Senanayake, V. Narayanamurti, S. Ramanathan, "Correlation between metal-insulator transition characteristics and electronic structure changes in vanadium oxide thin films", Phys. Rev. B **77**, 195442 (**2008**).

7.9 J. Lappalainen, S. Heinilehto, S. Saukko, V. Lantto, H. Jantunen, "Microstructure dependent switching properties of VO_2 thin films", Sens. Actuators A. Phys. **142**, 250 (**2008**).

7.10 D. Ruzmetov, S. Ramanathan, "Thin film metal-oxides", Springer New York, **51** (**2010**).

7.11 H. Liu, O. Vasquez, V.R. Santiago, L. Diaz, A.J. Rua, F.E. Fernandez, "Novel pulsed-laser-deposition-VO_2 thin films for ultrafast applications", J. Electron. Mater. **34**, 491 (**2005**).

7.12 S.B. Wang, S.B. Zhou, G. Huang, X.J. Yi, "VO_x thin films obtained by ion beam sputtering and oxidation process", Surf. Coat. Technol. **191**, 330 (**2005**).

7.13 J.H. Li, N.Y. Yuan, J.S. Xie, "Annealing characteristics of the vanadium oxide filsm prepared by modified ion beam enhanced deposition", Appl. Surf. Sci. **243**, 437 (**2005**).

7.14 C. Chen, X. Yi, J. Zhang, X. Zhao, "Linear uncooled microbolometer array based on VO<i>x</i> thin films", Infrared Phys. Technol. **42**, 87 (**2001**).

7.15 B.N. Masina, S. Lafane, L. Wu, S. Abdelli-Messaci, T. Kerdja, A. Forbes, "Optimisation study of the synthesis of vanadium oxide nano-structures suing pulsed laser deposition", Proc. Of SPIE **8996**, 899615 (**2004**).

7.16 B.N. Masina, S. Lafane, L. Wu, S. Abdelli-Messaci, T. Kerdja, A. Forbes, "Optimizing the synthesis of vanadium-oxygen nanostructures by plasma dynamics using optical imaging", OE **54** (3), 037106 (**2015**).

7.17 P.E. Dyer, A. Issa, P.H. Key, "Dynamics of excimer laser ablation of superconductor in an oxygen environment", Appl. Phys. **57**, 186 (**1990**).

7.18 H.S. Kwok, H.S. Kim, D.H. Kim, W.P. Shen, X.W. Sun, R.F. Xiao, "Correlation between plasma dynamics and thin films properties in pulsed laser deposition", Appl. Sur. Sci. **109/110**, 595 (1997).

7.19 H.S. Kim, D.H. Kim, H.S. Kwok, "Correlation between target-substrate distance and oxygen pressure in pulsed laser deposition of YBa2Cu3O7", Appl. Phys. Lett. **61**, 2234 (**1992**).

7.20 R. Castro-Rodriguez, D.R. Coronado, A. Iribarren, B.E. Watts, F. Leccabue, J.L. Pena, "Correlation between target-substrate distance and oxygen pressure in pulsed laser deposition", Appl. Phys. A **81**, 1503 (**2005**).

7.21 C. Julien, G.A. Nazri, O. Bergström, "Raman scattering studies of microcrystalline V6O13", Phys. Stat. Sol. (b) **201**, 319 (**1997**).

7.22 T.W. Chiu, K. Tonooka, N. Kikuchi, "Influence of oxygen pressure on the structural, electrical and optical properties of VO_2 thin films deposited on ZnO/glass substrates by pulsed laser deposition", Thin Solid Films **518**, 7441 (**2010**).

7.23 S. Lafane, T. Kerdja, S. Abdelli-Messaci, Y. Khereddine, M. Kechouane, O. Nemraoui, "Correlation of plume dynamics and oxygen pressure with VO_2 stoichiometry during pulsed laser deposition", Appl. Phy. A **112**, 159 (**2013**).

7.24 S. Amoruso, A. Sambri, X. Wang, "Plume expansion dynamics during laser ablation of manganates in oxygen atmosphere", Appl. Surf. Sci. **253**, 7696 (**2007**).

7.25 X. Cao, N. Wang, J.Y. Law, S.C.J. Loo, S. Magdassi, Y. Long, "Nanoporous thermochromics VO2 (M) thin films: controlled porosity, largely enhanced luminous transmittance and solar modulating ability", Langmuir **30**, 1710 (**2014**).

7.26 R.J. Morin, "Oxides which show a metal-to-insulator transition at the Neel temperature", Phys. Rev. Lett. **3**, 34 (**1959**).

7.27 L. Kang, Y. Gao, H. Luo, "A novel solution process for the synthesis of VO_2 thin films with excellent thermochromics properties", Appl. Mater. And Inter. **1** (10), 2211 (**2009**).

7.28 A.R. Begishev, G.B. Galiev, A.S. Ignat'ev, V.G. Mokerov, V.G. Poshin, "Influence of deviations from the crystal lattice periodicity on the semiconductor-metal phase transition in vanadium dioxide", Sov. Phys. Solid State **20** (6), 951 (**1978**).

7.29 M. Maaza, K. Bouziane, J. Maritz, D.S. McLachlan, R. Swanepool, J.M. Frigerio, M. Every, "Direct production of thermochromics VO_2 thin film coatings by pulsed laser ablation", Opt. Mat. **15** (1), 41 (**2000**).

7.30 J.Y. Suh, R. Lopez, L.C. Feldman, R.F. Haglund Jr, "Semiconductor to metal phase transition in the nucleation and growth of VO_2 nanoparticles and thin films", J. Appl. Phys. **96** (2), 1209 (**2004**).

7.31 P. Jin, S. Nakao, S. Tanemura, "High-energy W ion implantation into VO_2 thin film", Nucl. Instrum. Methods Phys. Res. Sect. B **141**, 419 (**1998**).

7.32 R.A. Aliev, V.N. Andreev, V.M. Kapralova, "Effect of grains sizes on the metal-semiconductor phase transition in vanadium dioxide polycrystalline thin films", Phys. Solid State **48**, 929 (**2006**).

7.33 V.A. Klimov, I.O. Timofeeva, S.D. Khanin, "Hysteresis loop construction for the metal-semiconductor phase transition in vanadium dioxide films", Tech. Phys. **47**, 1134 (**2002**).

7.34 R. Lopez, T.E. Haynes, L.A. Boatner, "Size effects in the structural phase transition of VO_2 nanoparticles", Phys. Rev. B **65**, 224 (**2002**).

7.35 A. Ilinski, F. Silva-Andrade, E. Shandrin, V. Klimov, "Variations in optical reflectivity in the semiconductor-metal phase transition of vanadium dioxide", J. Non-Cryst. Solids **338-334**, 266 (**2004**).

7.36 J.B. Kana Kana, J.M. Ndjaka, B.D. Ngom, A.Y. Fasasi, O. Nemraoui, R. Nemutudi, D. Knoesen, M. Maaza, "High substrate temperature induced

anomalous phase transition temperature shift in sputtered VO_2 thin films", Opt. Mater. **32**, 739 (**2010**).

7.37 Y. Gao, S. Wang, L. Kang, Z. Chen, J. Du, X. Liu, H. Luo, M. Kanehira, "VO_2-Sb:SnO_2 composite thermochromics smart glass foil", Energy Environ. Sci. **5**, 8234 (**2012**).

Chapter 8

Pulsed Laser Deposition of β-V_2O_5 nano-rods thin films

Vanadium pentoxide (V_2O_5) material has attracted much interest and extensively studied because of its excellent properties and applications in a wide range of fields [8.1-8.2]. V_2O_5 is a promising material for microelectronic, electrochemical, gas sensing and optoelectronic devices due to its excellent properties such as multiple valency, wide optical band gap, good chemical and thermal stability, excellent thermoelectric property [8.2-8.6]. Generally, V_2O_5 is a non-stoichiometric material, which is known for its catalytic properties in oxidation reactions [8.7], owing to its rich and diverse chemistry that is based on two factors; namely the variety of vanadium oxidation states, ranging from 2^+ to 5^+, and the variability of oxygen coordination geometries. V_2O_5 is the most saturated (highest oxidation state) and therefore the most stable one in the V-O system. Moreover V_2O_5 has several polymorphs, including α-V_2O_5 (orthorhombic) phase which is the most stable and common phase [8.8-8.9], β-V_2O_5 (monoclinic or tetragonal) metastable phase and γ-V_2O_5 (orthorhombic) [8.10-8.11].

Several deposition techniques have been already used to prepared V_2O_5 thin films on different substrates including sol-gel technique [8.12], magnetron sputtering [8.13], pulsed laser deposition (PLD) [8.14]. However, literature indicates that more often than not, as-deposited V_xO_y films were subsequently annealed in various atmospheres in order to improve the V_2O_5 stoichiometry and nano-structures. Fang et al. [8.15] have prepared α-V_2O_5 thin films with a V_2O_5 target by PLD and followed by post-deposition annealing on the ITO glass substrate. The α-V_2O_5 thin films have been sufficiently

investigated [8.16-8.19] whereas there has been little experimental investigation of the β-V_2O_5 and γ-V_2O_5 phases due to the demanding preparation conditions [8.20]. Few reports indicate that the metastable phase of β-V_2O_5 thin films can be deposited by using magnetron sputtering and the temperature of substrates plays an important role during the deposition process and followed by post-annealing [8.10, 8.21]. Zou *et al.* [8.22-8.23] deposited nano-rods β-V_2O_5 by post-annealing amorphous α-V_2O_5 thin film under oxygen atmosphere from 400 – 550 °C for 1 hour.

The plasma plume expansion (in Chapters 4 and 5) and the V_xO_y thin films (in Chapter 6)' analysis shows that high oxides thin films are efficiently produced when a shock-wave-like propagation stage is achieved. In this chapter, then we show that it is possible to synthesize and improve the β-V_2O_5 composition by investigating the link between the V-O plume and the V_2O_5 stoichiometry in PLD without the need of post-deposition annealing. The plasma plume expansion dynamics of an ablated VO_2 target was investigated using fast-imaging technique under a range of oxygen partial pressures and under vacuum, and correlated to two well-known plasma propagation models as discussed in Chapter 4. By optimization of the parameters we report high quality β-V_2O_5 nano-rods, without post-deposition annealing, and on a glass substrate.

8.1 Experimental Set-up

The schematic diagram of the experiment setup used to synthesized V_xO_y thin films in this chapter is already discussed in Chapter 4 and is given in Figure 4.1. V_xO_y thin films

were deposited on 500 °C Corning glass at a pulse repetition rate of 5 Hz for 10 minutes under the same pressures (0.1 and 0.2 mbar) and pulse energy conditions as that used for the plasma plume study. The target to substrate distance was determined using the plasma plume propagation graph as discussed in Chapter 4. The plasma plume experiment details have been discussed in Chapters 4 and 5.

8.2 Results and Discussion

A. Plume Dynamics Results

It has been shown that the plasma dynamics plays an important role in growing high-quality complex oxide thin films when target-substrate distance is optimised with respect to the oxygen pressure (P) in PLD [8.24]. Beyond a certain target-substrate distance, the plasma flux loses its unidirectional velocity, scatters and thermalizes and this distance provides the optimum condition for film growth [8.25-8.26]. In this study, we showed that an optimum conditions for β-V_2O_5 thin film growth is below certain oxygen level and when the plume start slowing down (slow shock) as shown in Figure 8.1. Points A, B, C and D in Figure 8.1 satisfy this condition.

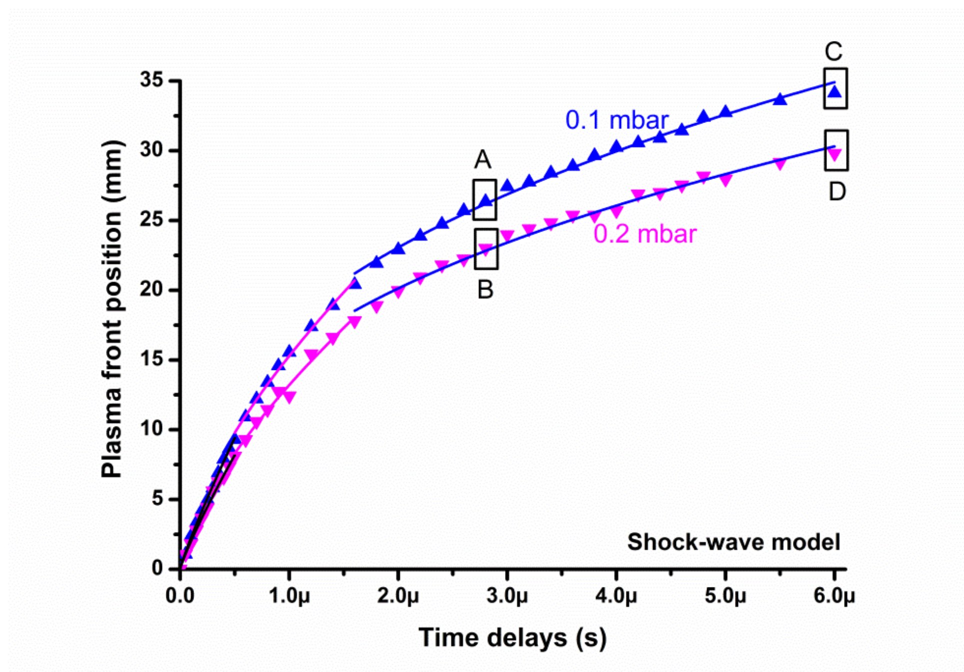

Figure 8.1: Propagation of plasma plume front position for different oxygen gas pressure fitted with the point-blast-wave which is indicating a free-expansion (black), plane-wave front (magenta) and spherical-wave front (blue) propagation.

B. Structural Analysis

We deposited polymorphs of V_2O_5 thus are α-V_2O_5 (space group: PmmnE, JCPDS No. 001-0359) and β-V_2O_5 [8.22-8.23] for target-substrate distance of 23 and 27 mm as shown in Figure 8.2. This was confirmed by Raman analysis as given in Figure 8.3. The Raman spectra indicates V_2O_5 phase for both samples [8.4]. A trace amount of VO_2 (M1) β-phase (space group: PmmnE, JCPDS No. 44-1438) was observed for 0.1 mbar (27 mm) thin film as shown in Figure 8.2. A trace amount of β-V_2O_5 was observed for 0.2 mbar (23 mm) thin film as shown in Figure 8.2. SEM micrographs indicate nano-rods for 0.2 mbar (23 mm) thin film and nano-particles for 0.1 mbar (27 mm) as shown in Figure 8.4. However the corresponding 3 x 3 μm AFM indicates nano-rods for both thin

films as shown in Figure 8.5. The thin films are homogeneous with the root mean square roughness of ~18.8 nm for 0.1 mbar (27 mm) and ~27.2 nm for 0.2 mbar (23 mm). The diameters of the nano-rods are ~100 nm for 0.1 mbar (27 mm) and 500 nm for 0.2 mbar (23 mm) according to AFM analysis. For these oxygen pressures (0.1 and 0.2 mbar), we obtain high oxidation phases of vanadium. This is understandable since at these oxygen pressures we observed the plume splitting and plume sharpening due to the interaction between the plume species and the background gas. This corresponds very well with the point-blast-wave model as the model indicated that at these oxygen pressures an ideal shock condition was achieved as shown in Figure 8.1. Therefore highly reactive atomic oxygen is produced in the shocked layer and oxygen enrichment in the deposited film is expected [8.27], as shown in Figure 8.2.

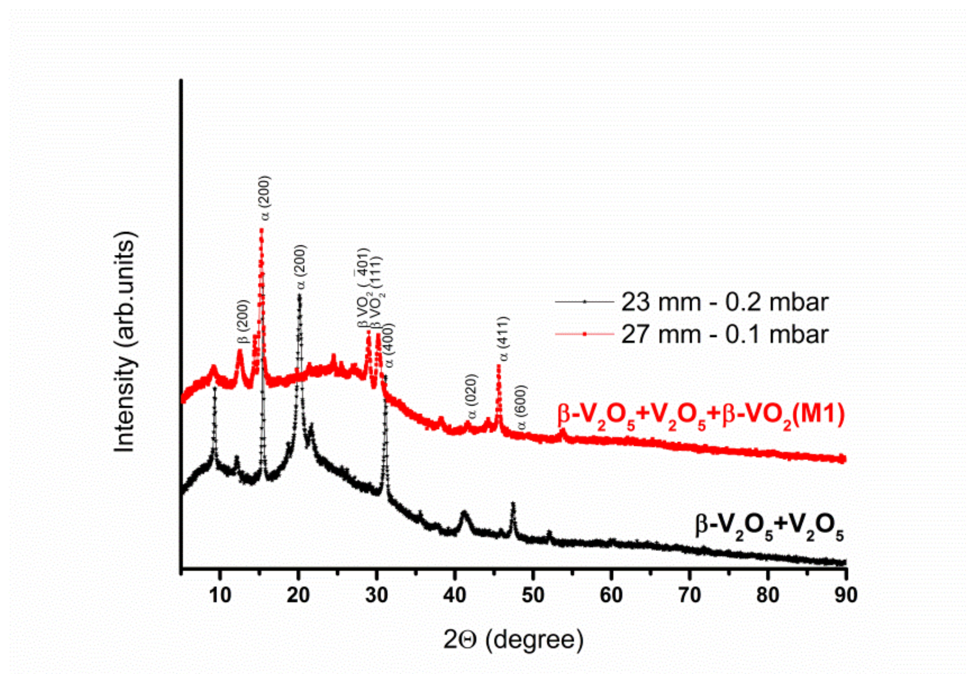

Figure 8.2: XRD spectra of V_xO_y thin films deposited under high oxygen gas pressure (0.2 and 0.1 mbar) and target-substrate distance for 23 and 27 mm. These parameters were determined from points A and B in the plasma propagation graph as given in Figure 8.1.

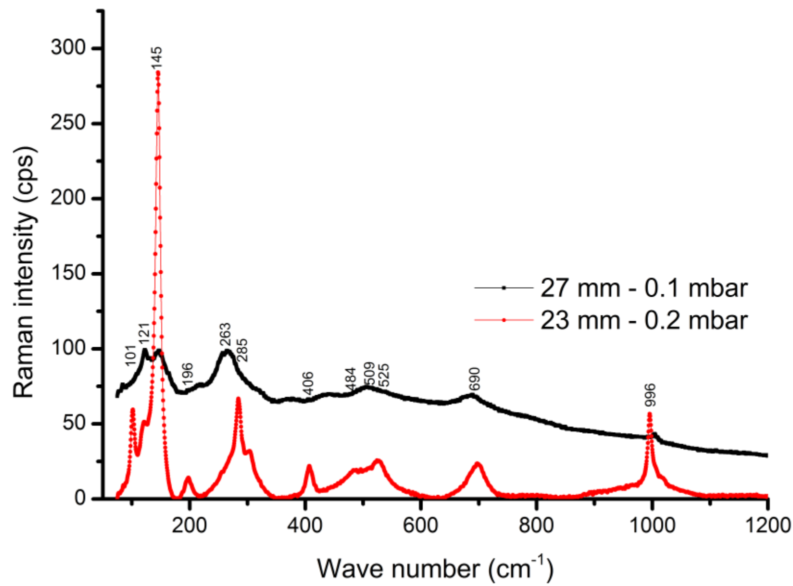

Figure 8.3: Raman spectra of V_2O_5 thin films deposited under 0.2 and 0.1 mbar oxygen pressure and target-substrate distance for 23 and 37 mm. These parameters were determined from points A and B in the plasma propagation graph as given in Figure 8.1.

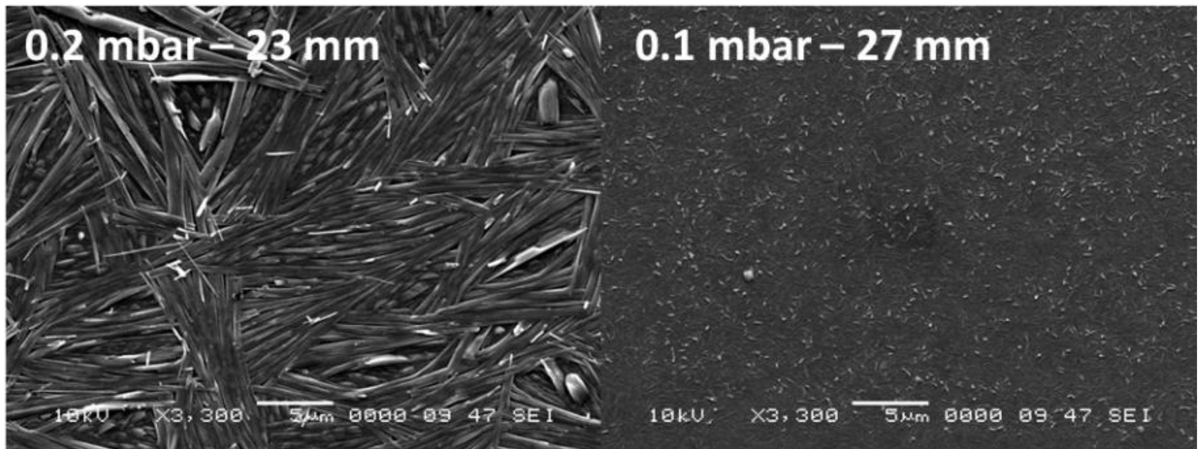

Figure 8.4: SEM micrographs of V_xO_y thin films deposited under high oxygen gas pressure (0.2 and 0.1 mbar) and target-substrate distance for 23 and 27 mm. These parameters were determined from points A and B in the plasma propagation graph as shown in Figure 8.1.

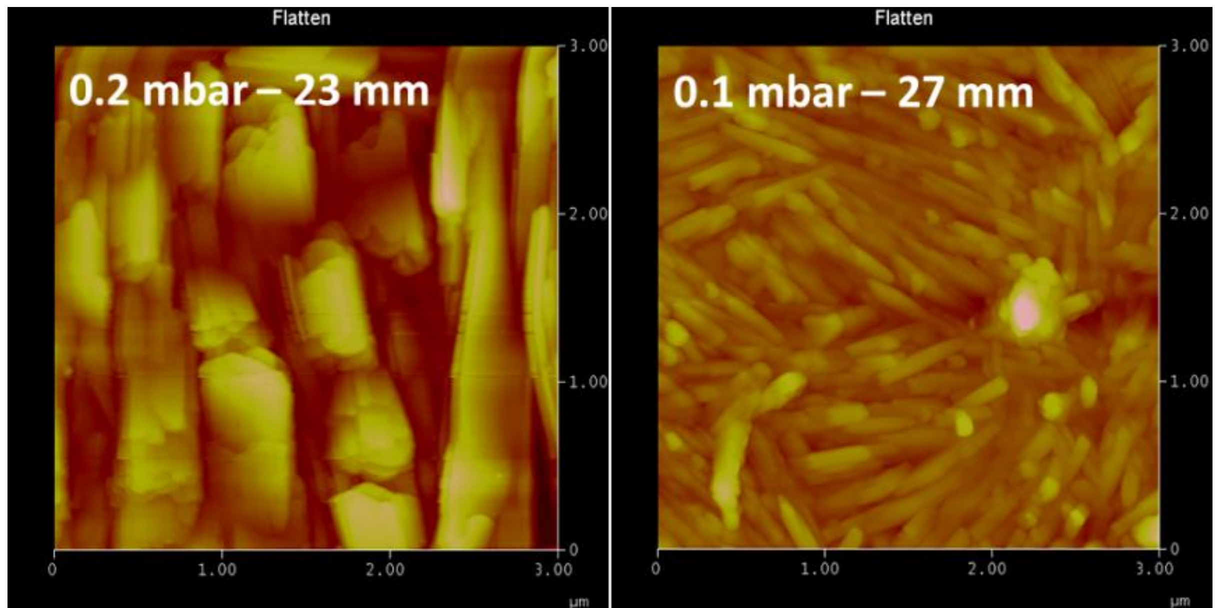

Figure 8.5: AFM images of V_xO_y thin films deposited under high oxygen gas pressure (0.2 and 0.1 mbar) and target-substrate distance for 23 and 27 mm. These parameters were determined from points A and B in the plasma propagation graph as given in Figure 8.1.

We optimized the V_xO_y thin films by increasing the target–substrate distances per oxygen pressures. The target-substrate distance per oxygen pressures at the 5.6 μs time-delay in the plasma plume propagation graph are 34 mm for 0.1 mbar and 29 mm for 0.2 mbar, as shown in Figure 8.1. These parameters are indicated as point C and D in the plasma plume propagation graph as shown in Figure 8.1. As the target-substrate distance increases, the β-V_2O_5 diffraction peak increases for thin films prepared at 0.2 mbar oxygen pressure at 29 mm target-substrate distance as shown in Figure 8.6. However for thin film prepared at 0.1 mbar oxygen pressure at 34 mm, all the diffraction peaks decreases and/or disappear as shown in Figure 8.6. These were observed in the Raman spectra as well and are given in Figure 8.7. SEM micrographs and AFM (3 μm x 3 μm) images indicates nano-rods for both thin films as shown in

Figures 8.8 and 8.9, respectively. The grain width size of the nano-rods reduced as the target-substrate distance increases for both thin films prepared at 0.2 and 0.1 mbar oxygen pressures as shown in Figures 8.5 and 8.9. β-V_2O_5 phase was successfully obtained at 0.2 mbar oxygen pressure as the target-substrate increased.

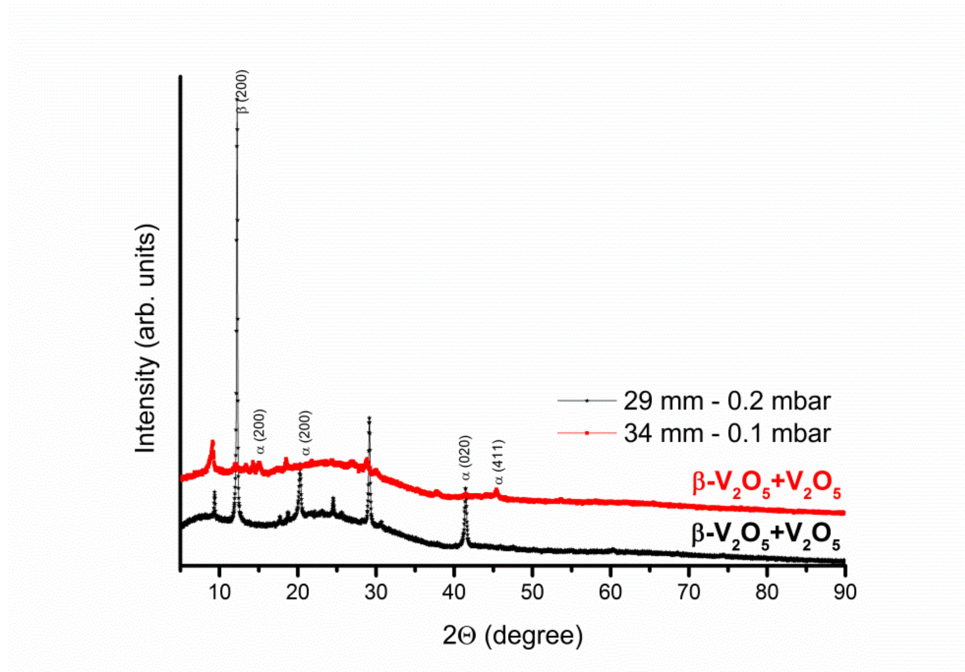

Figure 8.6: XRD spectra of V_2O_5 thin films deposited under 0.2 and 0.1 mbar oxygen pressure and target-substrate distance for 29 and 34 mm. These parameters were determined from points C and D in the plasma propagation graph as given in Figure 8.1.

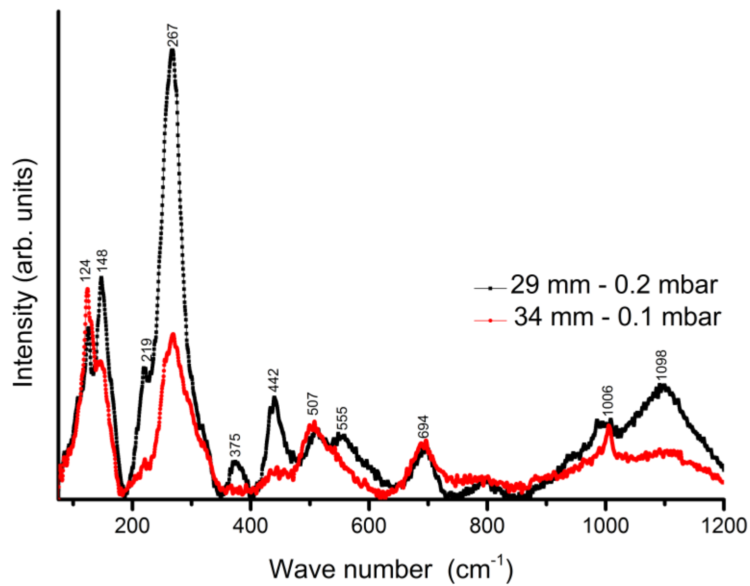

Figure 8.7: Raman spectra of V_2O_5 thin films deposited under 0.2 and 0.1 mbar oxygen pressure and target-substrate distance for 29 and 34 mm. These parameters were determined from points C and D in the plasma propagation graph as given in Figure 8.1.

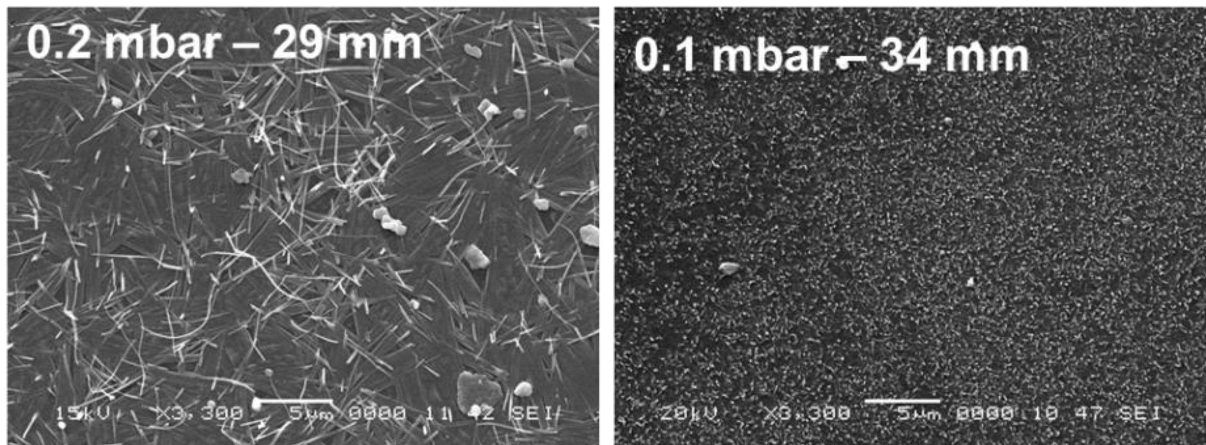

Figure 8.8: SEM micrographs of V_2O_5 thin films deposited under 0.2 and 0.1 mbar oxygen pressure and target-substrate distance for 29 and 34 mm. These parameters were determined from points C and D in the plasma propagation graph as given in Figure 8.1.

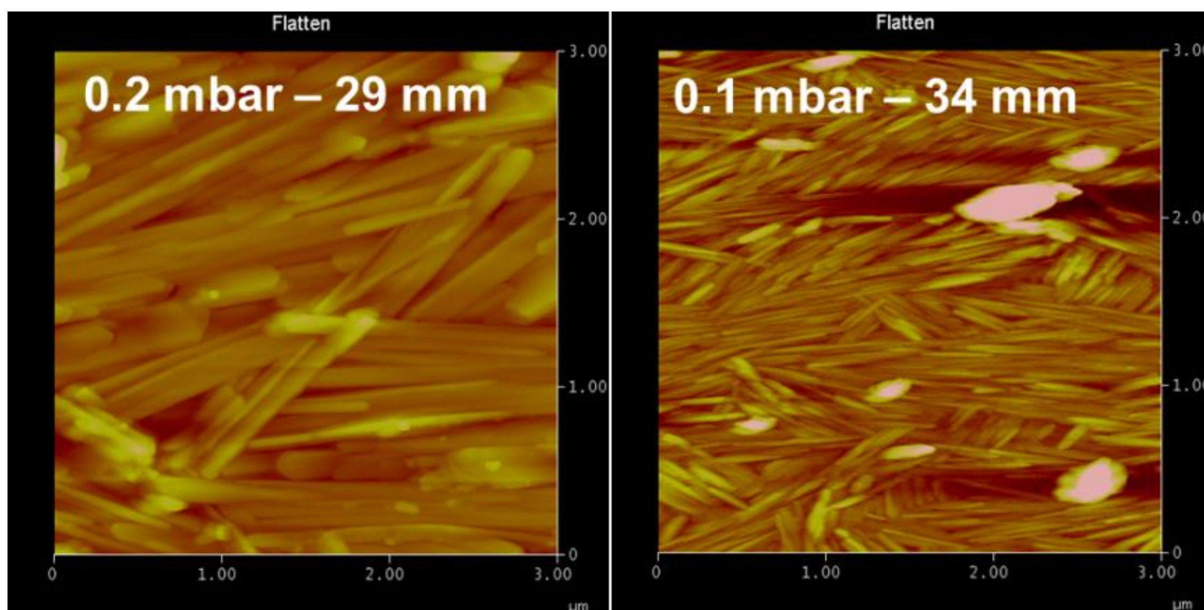

Figure 8.9: AFM images of V_2O_5 thin films deposited under 0.2 and 0.1 mbar oxygen pressure and target-substrate distance for 29 and 34 mm. These parameters were determined from points C and D in the plasma propagation graph as given in Figure 8.1.

We further optimized this β-V_2O_5 phase obtained at 0.2 mbar oxygen pressure by increasing the target-substrate distance to 37 mm as shown in Figure 8.10. By comparison, the XRD graph in Figure 8.10 indicates the increase of the β-V_2O_5 diffraction peak as the target-substrate distance increases. The XRD spectra indicate that the polycrystalline V_2O_5 thin film formed on the amorphous Corning glass substrate surface and showed a preferential orientation along the β-V_2O_5 (200) plane as shown in Figure 8.10. This is to compared to of the AFM morphology in Figure 8.11 which indicates that the nano-rods width decreases as the target-substrate distance increases. From these AFM results, we can see that the initially obtained V_2O_5 thin film transformed to β-V_2O_5 nano-rods after the increase of the target-to-substrate distance. It is clear that the initially obtained nano-rods are quite large in dimensions as shown

in Figure 8.11. This is understandable as the plasma plume propagation results which indicate that these target-substrate distances (0.2 mbar (23 mm) and 0.1 mbar (27 mm)) were close to the target surface and at these positions are the ones where the plume starts decaying, as shown in Figure 8.1. Furthermore, where plume kinetic energy was at highest peak, the plume split in two, resulted in the formation of the shock layer at the edge of the plume. These lead to an increase in the number of nano-particles arriving at the substrate surface. The high temperature of the substrate (500 °C) provides thermal energy for the ad-atom mobility process. These nano-particles aggregate with each other to form nucleation centers, because there is a sufficient thermal energy due to the substrate temperature. The aggregation becomes larger and larger because of the several nanoparticles collected on the substrate surface and this result in an increase of the nano-structure's dimension. These result in large nano-rods dimension depending on the oxygen pressure as shown in Figures 8.5 and 8.11. As for slim nano-rods as the target-substrate distance varied, this means that in term of the plasma plume propagation, the plume kinetic energy is decreasing and is no longer at highest peak and, at the same time, the substrate is bit far from target surface. This results in the decrease in the number of nano-particles arriving at the substrate surface and decrease of the nano-structure's dimension as shown in Figures 8.9 and 8.11. The obtained nano-rods formation can be interpreted as a surface energy driven process as Zou *et al.* [8.22] described in their obtained β-V_2O_5 nano-rods after post-deposition annealing it at 500 ºC in oxygen atmosphere. The β-V_2O_5 phase (200) is the highest energy low-index plane according to Sayle *et al.* [8.28] and then this direction should have the fastest growth rate [8.22] as we observed the fastest growth of the β-V_2O_5 phase as the target-substrate distance increases at 0.2 mbar oxygen pressure as shown in Figure 8.10.

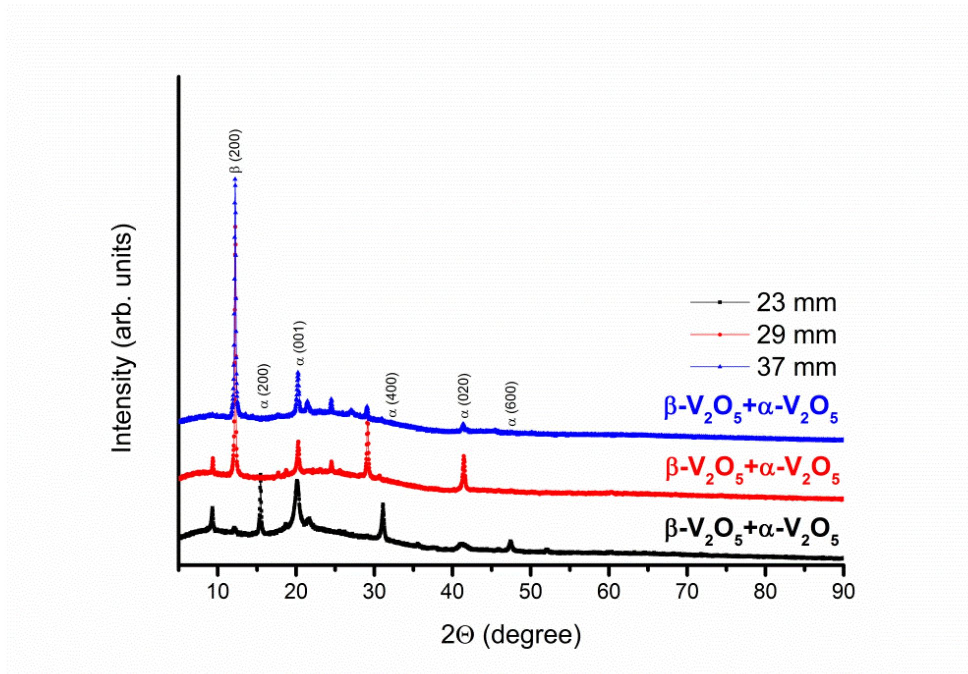

Figure 8.10: XRD spectra of V_2O_5 thin films deposited under 0.2 mbar oxygen pressure and target-substrate distance for 23, 29 and 37 mm.

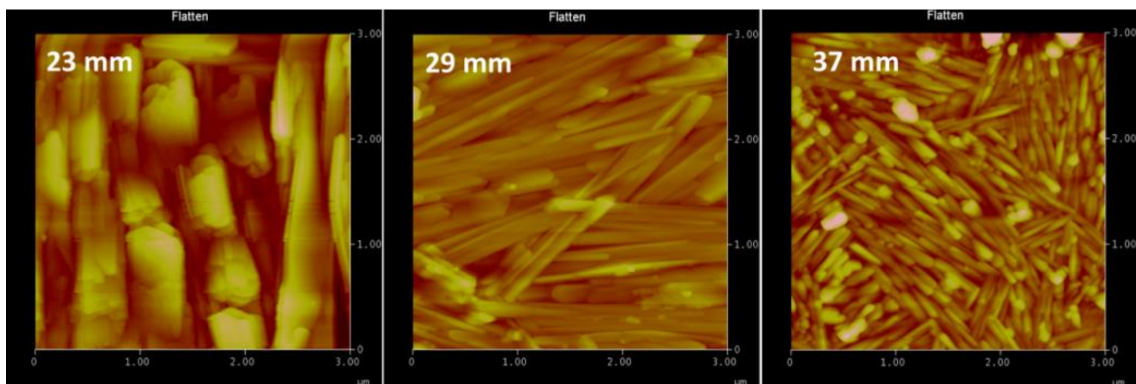

Figure 8.11: AFM images of V_2O_5 thin films deposited under 0.2 mbar oxygen pressure and target-substrate distance for 23, 29 and 37 mm.

8.3 Conclusions

A β-V_2O_5 phase was successfully deposited at 0.2 mbar oxygen pressure without post-annealing on Corning glass. These results indicate that the β-V_2O_5 will normally be deposited when the plume start slowing down and at below certain oxygen partial pressures. We found that by increasing the target-substrate distance, the nano-rods dimension can be reduced. Furthermore, the increase of the target-substrate distance optimized the β-V_2O_5 phase.

References

8.1 B.B. Lakshmi, C.J. Patrissi, C.R. Martin, "Sol-gel template synthesis of semiconductor oxide micro- and nanostrucutres", Chem. Mater. **9**, 2544, (**1997**).

8.2 R. Rella, P. Siciliano, A. Cricenti, R. Generosi, M. Girasole and M. Anderle, "A study of physical properties and gas-surface interaction of vanadium oxide thin films", Thin Solid Films **349**, 254 (**1999**).

8.3 Q.H. Wu, A. Thissen, W. Jaegermann, M. Liu, "Photoelectron spectroscopy study of oxygen vacancy on vanadium oxides surface", Appl. Surf. Sci. **236**, 437 (**2004**).

8.4 C.V. Ramana, R.J. Smith, O.M. Hussain, C.C. Chusuei and C.M. Julien, "Correlation between growth conditions, microstructure, and optical properties in pusled laser depositied V_2O_5 thin films", Chem. Mater. **17**, 1213 (**2005**).

8.5 F.N. Dultsev, L.L. Vasilieva, S.M. Maroshina, and L.D. Pokrovsky, "Structural and optical properties of vanadium pentoxide sol-gel films", Thin Solid Films **510**, 255 (**2006**).

8.6 G.J. Fang, Z.L. Liu, Y.Q. Wang, H.H. Liu, and K.L. Yao, "Orientated growth of V2O5 electrochromic thin films on transparent conductive glass by pulsed excimer laser ablation technique", J. Phys. D: Appl. Phys. **33**, 3018 (**2000**).

8.7 B.M. Weckhuysen, D.E. Keller, "Chemistry, spectroscopy and the role of supported vanadium oxides in heterogeneous", Catal. Today **78**, 25 (**2003**).

8.8 N. Fateh, G.A. Fontalvo, L. Cha, and T. Klunsner, G. Hlawacek, C. Teichert, C. Mitterer, "Synthesis-structure relations for reactive magnetron sputtered V_2O_5 films", Surf. Coat. Technol. **202**, 1551 (**2008**).

8.9 S.P. Lim, J.D. Long, S. Xu, K. Ostrikov, "Nanocrystalline vanadium oxide films synthesized by plasma-assisted reactive rf sputtering deposition", J Phys. D: Appl. Phys. **40**, 1085 (**2007**).

8.10 Q. Su, W. Lan, Y.Y. Wang, X.Q. Liu, "Structural characterization of β-V_2O_5 films prepared by DC reactive magnetron sputtering", Appl. Surf. Sci. **255**, 4177 (**2009**).

8.11 V.P. Filonenko, M. Sundberg, P.-E. Wernerb, I.P. Zibrov, "Structure of a high-pressure phase of vanadium pentoxide, β-V_2O_5", Acta Crystallogr. B **60**, 375 (**2004**).

8.12 N.T.H. Bay , P.M. Tien, S. Badilescu, Y. Djaoued, G. Bader, F.E. Girouard, V. Troung, L. Nguyen, "Optical and electrochemical properties of vanadium pentoxide gel thin films", J. Appl. Phys. **80,** 7041 **(1996).**

8.13 M.G. Krishna, Y. Debauge and A.K. Bhattacharya, "X-ray photoelectron spectroscopy and spectral transmittance study of stoichiometry in sputterd vanadium oxide films", Thin Solid Films **312**, 116 (**1998**).

8.14 R.M. Bowman and J.M. Gregg, "VO_2 thin films: growth and effect of applied strain on their resistance", J. Mater. Sci., Mater. Elctron. **9**, 187 (**1998**).

8.15 G.J. Fang, Z.L. Liu, Y.Q. Wang, H.H. Liu, K.L. Yao, "Orientated growth of V_2O_5 electrochromic thin films on transparent conductive glass by pulsed excimer laser ablation technique", J. Phys. D: Appl. Phys. **33**, 3018 (**2000**).

8.16 A. Talledo, C.G. Granqvist, "Electrochromic vanadium-pentoxide-based films: Structural, electrochemical, and optical properties", J. Appl. Phys. **77** (9), 4655 (**1995**).

8.17 K.V. Madhuri, K.S. Rao, B.S. Naidu, O.M. Hussain, R. Pinto, " Characterization of laser-ablated V2O5 thin films", J. Mater. Sci.:Mater. Ele. **13**, 425 (**2002**).

8.18 G. Li, S. Pang, L. Jiang, Z. Guo, Z. Zhang, "Environmentally friendly chemical route to vanadium oxide single-crystalline nanobelts as a cathode material for lithium-ion batteries", J. Phys. Chem. B **110**, 9383 (**2006**).

8.19 Y. Iida, Y. Kanno, "Characterization of Ag-doped V_2O_5 thin films fabricated by pulsed laser deposition for photochromic devices", Japanese J. Appl. Phys. **47** (1), 667 (**2008**).

8.20 N. Pinna, M. Willinger, K. Weiss, J. Urban and R. Schlolgl, "Local structure of nanoscopic materials: V_2O_5 nanorods and nanowires", Nano Lett. **3**, 1131 (**2003**).

8.21 A. Talledo, H. Valdivia, C. Benndorf, "Invesigation of oxide (V2O5) thin films as electrodes for rechargeable microbatteries using Li", J Vac. Sci. Technol. A **21**, 1494 (**2003**).

8.22 C.W. Zou, X.D. Yan, R.Q. Chen, Z.Y. Wu, A. Alyamani, W. Gao, "Effect of annealing on the microstructure and optical properties of ZnO/V_2O_5 composite", Appl. Phys. Lett. **98**, 111904, (**2011**).

8.23 C.W. Zou, X.D. Yan, D.A. Patterson, E.A.C. Emmaelsson, J.M. Bian, W. Gao, "Temperature sensitive crystallization of V_2O_5: from amorphous film to β-V_2O_5 nanorods", Cryst. Eng. Comm. **12**, 691, (**2010**).

8.24 H.S. Kwok, H.S. Kim, D.H. Kim, W.P. Shen, X.W. Sun, R.F. Xiao, "Correlation between plasma dynamics and thin film properties in pulsed laser deposition", Appl. Sur. Sci. **109-110**, 595 (**1997**).

8.25 H.S. Kim, D.H. Kim, H.S. Kwok, "Correlation between target-substrate distance and oxygen pressure in pulsed laser deposition of YBa2Cu3O7", Appl. Phys. Lett. **61**, 2234 (**1992**).

8.26 R. Castro-Rodriguez, D.R. Coronado, A. Iribarren, B.E. Watts, F. Leccabue, J.L. Pena, " Correlation between target-substrae distance and oxygen pressure in pulsed laser deposition of complex oxide thin films", Appl. Phys. A **81**, 1503 (**2005**).

8.27 S. Lafane, T. Kerdja, S. Abdelli-Messaci, Y. Khereddine, M. Kechouane, O. Nemraoui, "Correlation of plume dynamics and oxygen pressure with VO_2 stoichiometry during pulsed laser deposition", Appl. Phys. A **112**, 159 (2013).

8.28 D.C. Sayle, D.H. Gay, A.L. Rohl, C.R. Catlow, J.H. Harding, P. Nortier, "Computer modelling of V2O5: surface structures, crystal morphology and ethane sorption", J. Mater. Chem. **6**, 663 (**1996**).

Chapter 9

Effect of Laser Wavelengths in PLD Technique on the Structural, Optical Properties of the VO_2 Thin Films

A single crystal VO_2 (M1) exhibits a change in electrical resistivity in the order of 10^5 over a temperature change of 0.1 °C at 68 °C [9.1, 9.2, 9.3]. This material is useful for potential applications as switching device [9.4], thermal sensing [9.5], because of its dramatic changes in electrical resistivity and infrared transmission which occur across the phase transition. The properties of VO_2 thin films comparing with the single crystalline VO_2 can be largely affected by several factors such as strain [9.6], defects density [9.7], and the existence of the multivalent vanadium ions (V^{2+}, V^{3+}, V^{4+}, V^{5+}) [9.8]. These discrepancies make it difficult to deposit high quality VO_2 thin films with sharp transition width, narrow thermal hysteresis, large electrical and optical property change. Additionally the magnitude of resistivity change and the size of the hysteresis width are very sensitive to the stoichiometry and the crystalline structure of the VO_2 thin film. There have been several research works performed in an attempt to reduce the transition temperature by using dopants [9.9], deposition by ion-assisted reactive evaporation followed by thermal annealing [9.10], and relaxing tensile stress by ion bombardment [9.11]. While these techniques successfully reduced the transition temperature, the desired electrical and optical properties are somewhat degraded as well to the contrary [9.12].

It has been shown that single crystals substrate is effective to obtain VO_2 thin films with a large electrical change during phase transition and a narrow hysteresis width because MIT domain wall propagation of highly oriented VO_2 is faster. Highly oriented VO_2 films

have been obtained on sapphire and TiO_2 single crystals [9.12-9.14]. The results show that the conductivity exhibits more than four orders of magnitude for the highly (100) texture of VO_2 thin films and only three orders of magnitude for the highly (010) texture of sample with a hysteresis behavior upon heating and cooling through the transition [9.14]. These are few reports [9.15-9.17] concerning the synthesis of a-axis oriented VO_2 thin films on glass substrates. Zhang *et al.* [9.15] have grown a-axis oriented VO_2 polycrystals on glass substrates by radio-frequency reactive sputtering technique using V_2O_5 target. They successfully deposited a highly oriented (100) VO_2 thin film nano-structures, after the recrystallization process of the thin film took place after annealing the sample at 450 °C. Their sample demonstrated a MIT temperature at 58 °C and 50 °C with the hysteresis loop width of 8 °C. Ngom *et al.* [9.16] deposited VO_2 thin films exhibited a predominantly (100) orientation on the soda-lime glass at 600 °C substrate temperature followed by a recrystallization process in temperature range of 5 °C to 25 °C. Diallo *et al.* [9.17] deposited VO_2 thin films on soda lime glass substrate by PLD and vanadium (V) metal target. They found that at 550 °C substrate temperature, a change in VO_2 (100) preferential orientation could be achieved. Their sample demonstrated a MIT temperature at 79 °C and 68 °C with the hysteresis loop width of 11 °C and large crystalline size of 350 nm.

In this chapter, we report the influence of the laser wavelengths in PLD technique on the structural, optical properties of the optimized VO_2 thin films. We are reporting on the synthesis of a-axis oriented and nano-particles VO_2 (M1) using PLD on Corning glass without post-deposition annealing and doping.

9.1 Experimental Set-up

The Nd: YAG laser beam as well as its harmonics (λ = 1064, 532, 355 and 266 nm, τ = 8 ns) was focused onto the rotating V metal target with an incident angle of 45° using a cylindrical lens. The pulsed energy was fixed at 70 mJ with 2 mm diameter of the laser spot size for all the laser wavelengths (532, 355 and 266 nm). The vacuum chamber was evacuated to a base pressure of 10^{-5} mbar and thereafter oxygen was introduced. V_xO_y thin films were deposited on 450 °C Corning glass at a pulse repetition rate of 10 Hz for 20 minutes under the same oxygen pressure, 0.05 mbar and target-substrate distance was set to 49 mm.

The properties of the produced V_xO_y thin films were characterized by using X-Ray Diffraction (XRD), Scanning Electron Microscopy (SEM), Atomic Force Microscopy (AFM), and Ultraviolent-visible near Infrared (UV-Vis-NIR) spectrophotomer coupled to a heating stage. PANalytical X'Pert PRO is the XRD diffractometer that was used and the X-ray source was a Cu-tube with a beam size of 0.38 mm. The operating voltage and current were 45 kV and 40 mA, respectively. The XRD patterns of the V_xO_y thin films were measured from 2θ = 0° to 90°. JEOL-JAM 7500F scanning electron microscope (SEM) was used in this study and Digital Instruments Nanoscope, Veeco; MMAFMLN-AM atomic force microscope (AFM) was used in this study. Perkin Elmer LAMDA 750S UV/VIS spectrophotometer coupled with the heating stage is the UV-Vis-NIR was used in this study to investigate the thermochromics properties of the VO_2 thin films. Wavelength dependence transmittance was measured in the range of 300 - 3000 nm at temperature ranging from 30 °C to 100 °C corresponding to semiconductor and metallic states of VO_2 material.

9.2 Results and Discussion

A. Structural Analysis

The XRD patterns of the V_xO_y thin films deposited on 450 °C temperature of Corning glass substrate at different laser deposition wavelengths using V target are given in Figure 9.1. The prominent XRD peaks in Figure 9.1 are occurring around 2θ = 18.3º, 2θ = 27.7º, and 2θ = 37.08º corresponding respectively to (100), (011), and (200) diffraction planes, along with several weak diffraction peaks which confirms the monoclinic VO_2 thin films (JCPDS No. 43-0251).

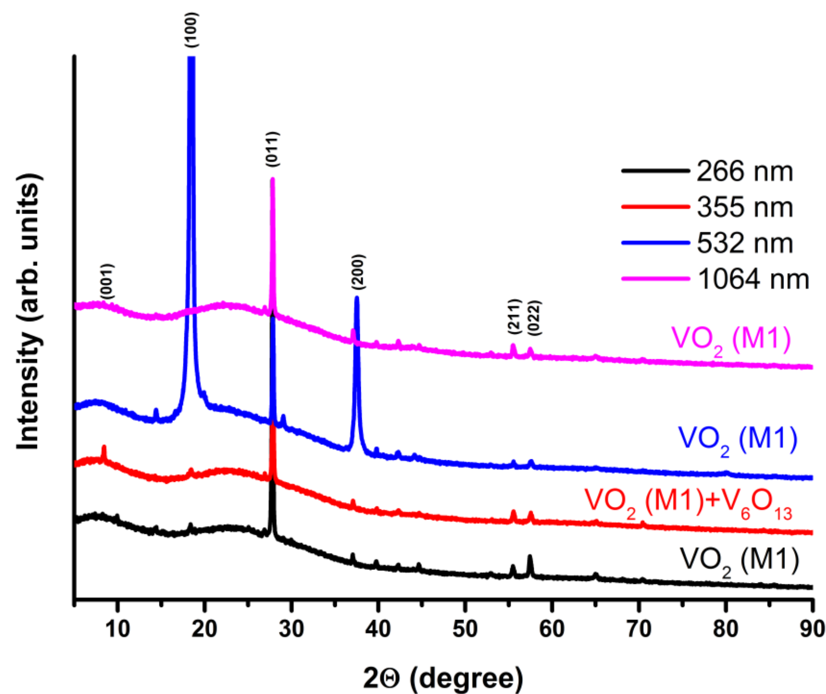

Figure 9.1: XRD spectra of VO_2 (M1) thin films deposited using several laser wavelengths (1064, 532, 355 and 266 nm) under 0.05 mbar oxygen pressure and target-substrate distance for 49 mm on 450 °C Corning glass.

A pure monoclinic rutile-type VO_2 (M1), single crystalline nature obtained on the thin films prepared using V target for laser wavelengths of 266, 355 and 1064 nm as indicated by XRD patterns in Figure 9.1. Furthermore a weak diffraction peak occurring around 2θ = 18.3°(100) was observed in both thin films prepared using V target for laser wavelengths of 266 and 355 nm as shown in Figure 9.1. This is the first study to observe this diffraction peak. The crystalline grains are preferentially oriented along the VO_2 (011) diffraction as shown in Figure 9.1. This is the normal preferentially oriented VO_2 (011) usually obtained when non-single crystals substrates are used [9.18-9.20]. Liu *et al.* [9.18] made similar findings when they successfully obtained VO_2 (M1) on fused quartz substrates by ablating a metallic V target at 200 mTorr of Ar/O_2 in PLD. Whereas for thin film deposited at 532 nm laser wavelength using V target, the XRD patterns indicates monoclinic rutile-type VO_2 (M1) polycrystalline nature of the film as given in Figure 9.1. The crystalline grain is preferentially oriented along the VO_2 (100) as given in Figure 9.1.

As mentioned in the introduction, few reports have presented similar findings after the annealing and recrystallization process [9.15-9.17]. Zhang *et al.* [9.15] obtained a highly (100) oriented VO_2 on glass substrates using radio-frequency reactive sputtering technique and V_2O_5 target after recrystallization process at 450 ºC. Ngom *et al.* [9.16-9.17] deposited VO_2 thin films exhibiting a predominantly (100) orientation on the soda-lime glass at a substrate temperature of 600 °C followed by a recrystallization process in temperature range of 5 °C to 25 °C. More often this preferential orientation is found when single crystals substrates are used such as sapphire and TiO_2 [9.12-9.13, 9.21-9.22]. Pei-ran *et al.* [9.21] successfully deposited highly (020) (040) oriented VO_2 thin films with a good crystalline structure and excellent electrical properties by

making use of the 532 nm laser wavelength in pulsed laser ablation technique. The VO_2 thin films were grown on (0001) sapphire substrate that was pre-treated in air and also annealed at 1450 °C for 12 hours before the deposition. The target-substrate distance was about 5.5 cm and temperature substrate during the deposition was at 400 °C. The V metal target was used and the pressures of the oxygen were changed from 1 – 8 Pa. In this study, Corning glass was used as a substrate and a highly oriented VO_2 (M1) in the (100) plane was obtained without post-deposition annealing. Garry *et al.* [9.22] successfully obtained highly oriented VO_2 thin film in the (100) (200) (300) (400) planes on R-plane sapphire (012) substrate by PLD using V metal target. The presence of VO_2 (100) diffraction peak was observed for the first time on sapphire substrate. Usually (020) and (040) diffraction peaks of VO_2 thin films are observed in the single crystals such as sapphire and TiO_2. The presence of VO_2 (100) and (300) diffraction peaks in their VO_2 film is not clearly understood. They suggested more investigations on this particular point. To the best of our knowledge no study yet observed these diffraction peaks on sapphire substrate. We observed similar diffraction peaks from VO_2 (100) and (200) in all our VO_2 thin films (532, 355 and 266 nm) as given in Figure 9.1. Muraoka *et al.* [9.13] obtained VO_2 (M1) preferential orientation of (002) grown on TiO_2 (001) by PLD using V_2O_3 pellet.

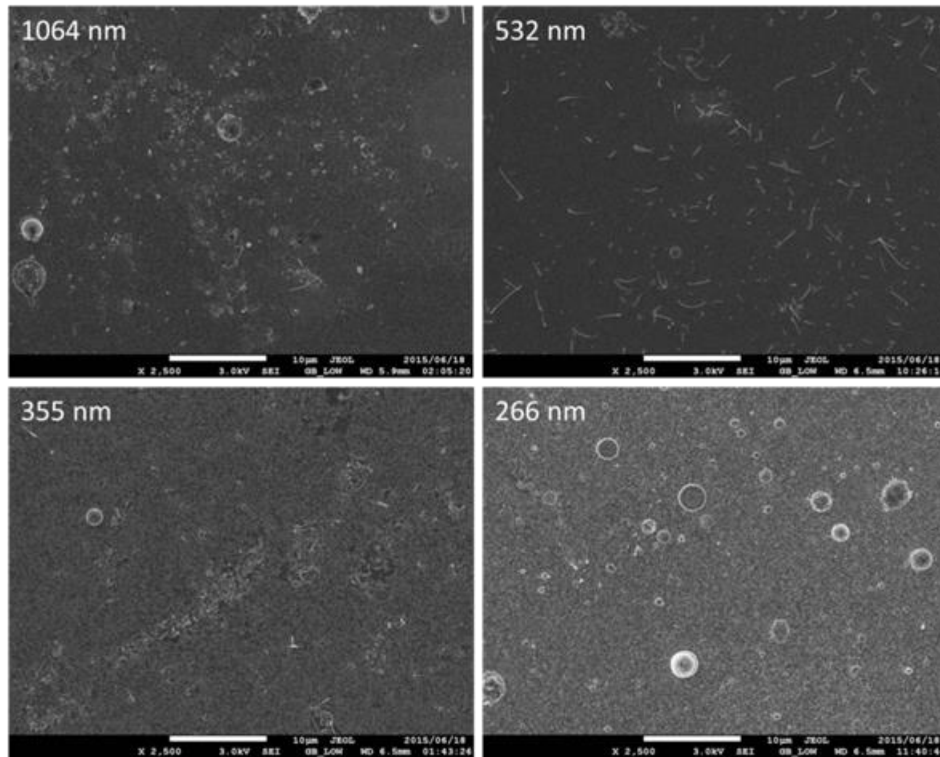

Figure 9.2: SEM micrographs of VO_2 (M1) thin films deposited using several laser wavelengths (1064, 532, 355 and 266 nm) under 0.05 mbar oxygen pressure and target-substrate distance for 49 mm on 450 °C Corning glass.

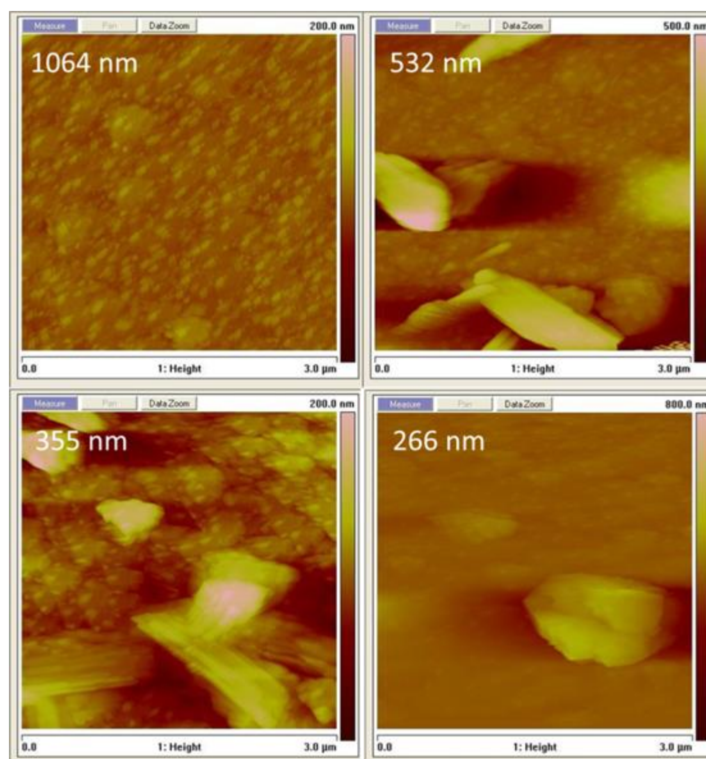

Figure 9.3: AFM images of VO_2 (M1) thin films deposited using several laser wavelengths (1064, 532, 355 and 266 nm) under 0.05 mbar oxygen pressure and target-substrate distance for 49 mm on 450 °C Corning glass.

The corresponding SEM micrographs for thin films prepared reveals nano-particles and nano-spheres for these VO_2 thin films (1064, 355 and 266 nm) as given in Figure 9.2, respectively. Whereas VO_2 thin film prepared at 532 nm (using V target) reveals nano-particles and nano-fibers as given in Figure 9.2. More details of the nano-structures are revealed in AFM images as given in Figure 9.3. The 3 x 3 µm AFM images for thin films shows that the thin films are not all uniform with root mean square (rms-) roughness of~5.92 nm (1064 nm), ~63.4 nm (532 nm), ~28.2 nm (355 nm) and ~36.7 nm for 266 nm as given in Figure 9.3. The well-known Debye's formula [9.23] was used to estimate the grain sizes of all the VO_2 thin films using the XRD peak of 27.81° (011) as indicated in Table 9.1.

B. Optical Switching Properties

The thermochromics properties of the VO_2 thin films were studied by wavelength dependence transmittance measurement in the range of 300-3000 nm at temperature ranging from 30 °C to 100 °C corresponding to MIT of VO_2 film. Transmittance as a function of a temperature measured at 2500 nm, a wavelength at which most of the samples show largest contrast in transmittance on switching. The MIT temperature was determined in this study as the minimum of the derivative of the temperature dependence of transmittance [9.24].

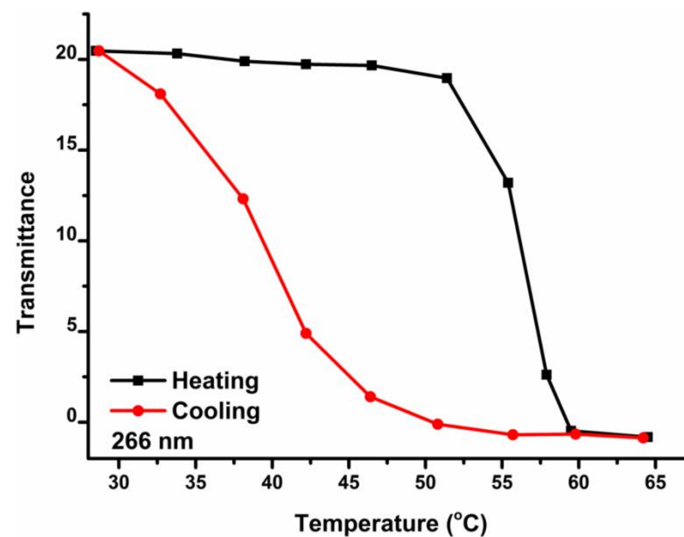

Figure 9.4: Change of the transmittance of a thin film under temperature cycling prepared at 266 nm laser wavelength under 0.05 mbar oxygen pressure and target-substrate distance for 49 mm on 450 °C Corning glass.

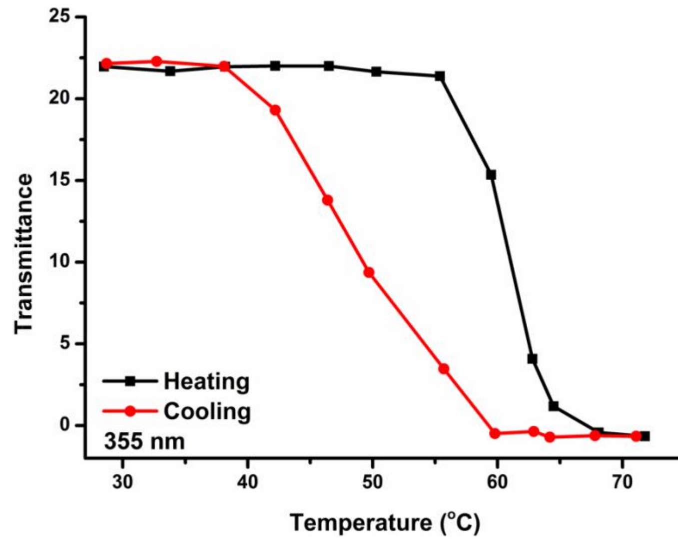

Figure 9.5: Change of the transmittance of a thin film under temperature cycling prepared at 355 nm laser wavelength under 0.05 mbar oxygen pressure and target-substrate distance for 49 mm on 450 °C Corning glass.

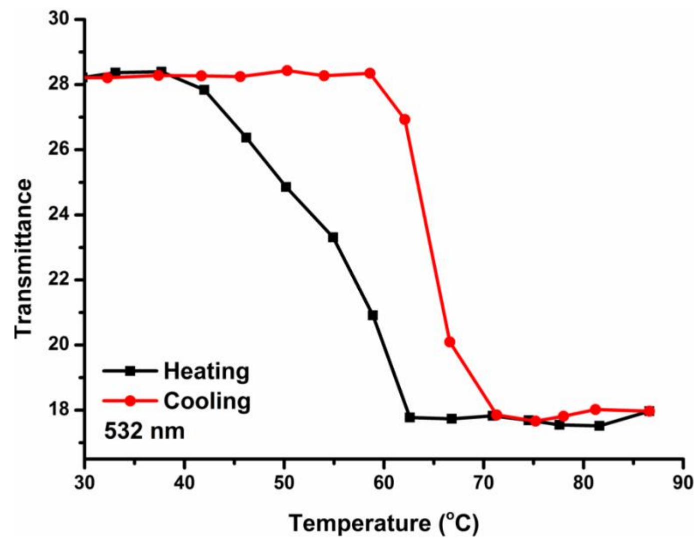

Figure 9.6: Change of the transmittance of a thin film under temperature cycling prepared at 532 nm laser wavelength under 0.05 mbar oxygen pressure and target-substrate distance for 49 mm on 450 °C Corning glass.

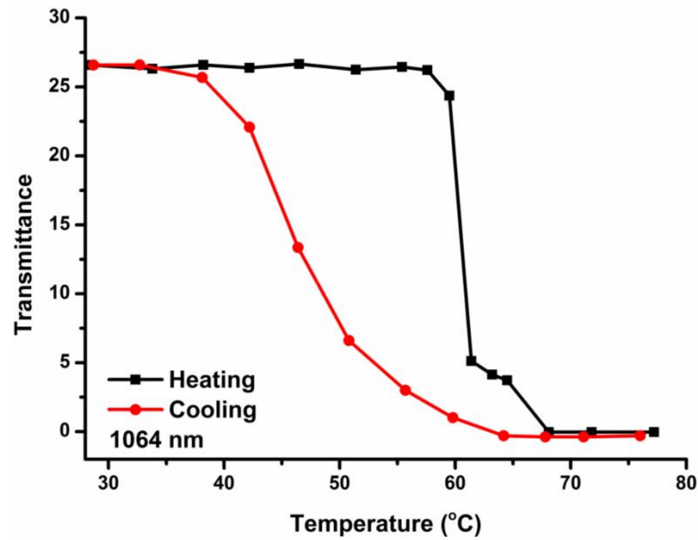

Figure 9.7: Change of the resistance and transmittance of a thin film under temperature cycling prepared at 1064 nm laser wavelength under 0.05 mbar oxygen pressure and target-substrate distance for 49 mm on 450 °C Corning glass.

Table 9.1: Switching and structural parameters

Laser wavelength (nm)	MIT temperature (°C)	Hysteresis width (°C)	Grain size (nm)	Roughness (nm)
1064	60.4	14	86.73	5.92
532	62.2	9.2	84.67	63.4
355	60.8	11.8	87.87	28.2
266	57.6	19.7	90.35	36.7

Figures 9.4 to 9.7 indicates the thermal hysteresis loops of the optical transmittance at fixed wavelength of 2500 nm for VO_2 thin films deposited at different laser wavelengths.

We observed qualitatively different hysteresis shapes for the VO_2 thin films deposited at different laser wavelengths as indicated in Figure 9.4 to Figure 9.7. The optical transmittance for VO_2 thin film deposited at 266 nm laser wavelength exhibit within the error bar, a transition located at ~57.6 °C with the hysteresis width of ~19.7 °C and also grain size of ~90.35 nm as given in Figure 9.4 and Table 9.1, respectively. For VO_2 thin film obtained at 355 nm laser wavelength indicates within the bar error a transition located ~60.8 °C with the hysteresis width of ~11.8 °C and also grain size of ~87.87 nm as shown in Figure 9.5 and Table 9.1, respectively, whereas the VO_2 thin film has a highly preferentially a-axis orientation obtained at 532 nm laser wavelength show within the bar error a transition located ~62.2 °C with the hysteresis width of ~9.2 °C and also grain size of ~84.67 nm as given in Figure 9.6 and Table 9.1, respectively. This hysteresis width is close to Zhang *et al.* [9.15] highly preferentially a-axis oriented VO_2 thin film. Their VO_2 thin film exhibit a hysteresis width of ~ 8 °C of MIT temperatures of 58 °C heating and 50 °C cooling after recrystallization process of the thin film took place after annealing it at 450 °C. In contract, Ngom *et al.* [9.16] found hysteresis width of ~4.8 °C of MIT temperatures of ~69.5 °C for their highly preferentially a-axis oriented VO_2 thin film after recrystallization process in temperature range of 5 °C to 25 °C. Moreover Diallo *et al.* [9.17] obtained hysteresis width of ~11 °C of MIT temperatures of 79 °C heating and 68 °C cooling for their highly preferentially a-axis oriented VO_2 thin film. The MIT temperature of the VO_2 thin film prepared at 532 nm is close to Pei-ran *et al.* [9.21] VO_2 thin films grown on sapphire substrate. Their VO_2 thin films demonstrated a reversible MIT temperature located at 62, 64 and 67 °C with the hysteresis widths from less than 1 to 3 K. We found that the MIT is in the same order for VO_2 thin films obtained at 355 and 532 nm laser wavelengths as given in Table 9.1 and these films

obtained 87.87 and 84.67 nm crystalline grain size, respectively as given in Figure 9.4. Whereas the VO_2 thin film obtained at 266 nm laser wavelength have lowest MIT and high grain size of the two thin films. Our results indicate that as the laser wavelengths increases, the hysteresis width decreases as given Table 9.1. Additionally, as the laser wavelengths increases, the a-axis diffraction peak increases as given in Figure 9.1. The smallest hysteresis width was observed in the highly a-axis orientation VO_2 thin film as given in Table 9.1.

9.3 Conclusions

A pure monoclinic rutile-type VO_2 (M1) phase was successfully deposited at 0.05 mbar of 49 mm using V target at laser wavelengths of 266, 355, 532 and 1064 nm without post-deposition annealing on Corning glass. A highly a-axis oriented VO_2 thin film was obtained at 532 nm laser wavelength without post-annealing on Corning glass. This film demonstrates a reversible MIT at ~62.2 °C with the smallest hysteresis width of ~9.2 °C and also corresponding to the smallest grain size of ~84.67 nm. These results are in agreement with the characteristic of VO_2 thin films and are as good as or better than VO_2 thin films made by other methods. We have shown that by make used of 532 nm laser wavelength in PLD, a highly a-axis oriented VO_2 thin film may grow on Corning glass.

References

9.1 F.J. Morin, "Oxides which show a metal-to-insulator transition at the Neel temperature", Phys. Rev. Lett. **3**, 34 (**1959**).

9.2 J. Nag, R.F. Haglund Jr, "Synthesis of vanadium dioxide thin films and nanopartilces", J. Phys.: Condens. Matter **20**, 26401 (**2008**).

9.3 H.K. Kim, H. You, R.P. Chiarello, H.L.M. Chang, T.J. Zhang, D.J. Lam, "Finite-size effect on the first-order metal-insulator transition in VO_2 films grown by metal-organic chemical-vapor deposition", Phys. Rev. B **47**, 12900 (1993).

9.4 C.H. Griffiths, H.K. Eastwood, "Influence of stoichiometry on the metal-semiconductor transition in vanadium dioxide", J. Appl. Phys. **45**, 2201 (**1974**).

9.5 A. Rua, F.E. Fernandez, N. Sepulveda, "Bending in VO_2-coated microcantilevers suitable for thermally activated", J. Appl. Phys. **107**, 074506 (**2010**).

9.6 J.Y. Suh, R. Lopez, L.C. Fieldman, R.F. Haglund, "Semiconductor to metal phase transition in the nucleation and growth of VO_2 nanoparticles and thin films", J. Appl. Phys. **96**, 1209 (**2004**).

9.7 D. Brassard, S. Fourmax, M. Jean-Jacques, J.C. Kieffer, M.A.E. Khakani, "Grain size effect on the semiconductor-metal phase transition characteristics of magnetron-sputtered VO_2 thin films", Appl. Phys. Lett. **87**, 051910 (**2005**).

9.8 L.L. Fan, Y.F. Wu, C. Si, C.W. Zou, Z.M. Qi, L.B. Li, G.Q. Pan, Z.Y. Wu, "Oxygen pressure dependent VO_2 crystal film preparation and the interfacial epitaxial growth study",Thin Solids Films **520**, 6124 (**2012**).

9.9 P. Jin, K. Yoshimura, S. Tamura, "Dependence of microsctructure and thermochromism on substrate temperature for sputter-deposited VO_2 epitaxial films", J. Vac. Sci. Technol. A **15**, 1113 (**1997**).

9.10 M. Fukura, S. Zambutsu, S. Miyazawa, "Preparation of VO_2 thin film and its direct bit recording characteristics" Appl. Opt. **22**, 265 (**1983**).

9.11 I. Balgerg, B. Abeles, Y. Arie, "Phase transition in reactively co-sputtered films of VO_2/TiO_2", Thin Solid Films **24**, 307 (**1974**).

9.12 D.H. Kim, H.S. Kwok, “Pulsed laser deposition of VO_2 thin films”, Appl. Phys. Lett. **65**, 3188 (**1994**)..

9.13 Y. Muraoka, Z. Hiroi, “Metal-insulator transition of VO_2 thin films grown on TiO_2 (001) substrates”, Appl. Phys. Lett. **80** (4), 583 (**2002**).

9.14 G. Garry, O. Durand, A. Lordereau, “Structural and optical properties of pulsed laser deposited VO_2 thin films on R- and C-sapphire planes”, Thin Solid Films **453**, 427 (**2004**).

9.15 Y. Zhang, R. Wang, Z. Qiu, X. Wu, Y. Li, “Growth of a-axis oriented vanadium dioxide polycrystals on glass substrates”, Mater. Lett. **131**, 42 (**2014**).

9.16 B.D. Ngom, M. Chaker, A. Diallo, I.G. Madiba, S. Khamlich, N. Manyala, O. Nemraoui, R. Madjoe, A.C. Beye, M. Maaza, “Competitive growth texture of pulsed laser deposited vanadium dioxide nanostructures on a glass substrate”, Acta Mater. **65**, 32 (**2014**).

9.17 A. Diallo, N.M. Ndiaye, B.D. Ngom, S. Khamlich, K. Talla, S. Ndiaye, O. Nemraoui, R. Madjoe, A.C. Beye, M. Maaza, “Effect of substrate temperature on the structure and the metal insulator transition in pulsed laser deposited VO2/films on soda lime glass”, J. Opt. **44** (1), 36 (**2015**).

9.18 H. Liu, O. Vasquez, V.R. Santiago, L. Diaz, A.J. Rua, F.E. Fernandez, “Novel pulsed-laser-deposition-VO_2 thin films for ultrafast applications”, J. Electron. Mater. **34**, 491 (**2005**).

9.19 F.B. Dejene, R.O. Ocaya, “Electrical, optical and structural properties of pure and gold-coated VO_2 thin films quartz substrate”, Current Appl. Phys. **10**, 508 (**2010**).

9.20 J. Jian, W. Zhang, C. Jacob, A. Chen, H. Wang, J. Huang, H. Wang, “Roles of grain boundaries on the semiconductor to metal phase transition of VO_2 thin films”, Appl. Phys. Lett. **107**, 102015 (**2015**).

9.21 Z. Pei-ran, S. Yamamoto, A. Miyashita, H. Naramoto, "Pulsed laser deposition of VO_2 single crystal thin films on sapphire substrates", Chin. Phys. Lett. **15** (12), 904 (**1998**).

9.22 G. Garry, O. Durand, A. Lordereau, "Structural, electrical and optical properties of pulsed laser deposited VO_2 thin films on R- and C-sapphire planes", Thin Solids Films **453-454**, 427 (**2004**).

9.23 X. Cao, N. Wang, J.Y. Law, S.C.J. Loo, S. Magdassi, Y. Long, "Nanoporous thermochromics VO_2(M) thin films: controlled porosity, largely enhanced luminous transmittance and solar modulating ability", Langmuir **30**, 1710 (**2014**).

9.24 A.R. Begishev, G.B. Galiev, A.S. Ignat'ev, V.G. Mokerov, V.G. Poshin, "Effect of violation of crystalline periodicity on semiconductor-metal phase transition in vanadium dioxide" Sov. Phys. Solid State **20** (6), 951 (**1978**).

Chapter 10

Conclusions and Future Work

10.1 Conclusions

The introduction and problem statements were presented in Chapter 1, as well as the contents of the thesis. A literature review of VO_2 was discussed in Chapter 2, including its structural, optical and electrical properties. The importance of laser induced plasma in PLD for the growth of V_xO_y nano-particles were discussed in Chapter 3. Furthermore, the physics and theory of the laser-solid-plasma interactions were discussed in details as well in Chapter 3.

The expansion dynamics of a laser ablation plume produced during KrF excimer laser irradiation of a VO_2 target in vacuum and oxygen ambient (0.01 to 0.2 mbar) was investigated using an ICCD camera in Chapter 4. The results revealed that the point of transition from one expansion regime of the plume to the next one varies, depending on the ambient gas pressures. For example, in the case of low oxygen pressures (0.01 and 0.05 mbar), the expansion initially remains linear and then deviates with increasing time. Whereas at high oxygen pressures (0.1 and 0.2 mbar), the plasma plume expansion dynamics passes from free-like to shock-like and finally reaches a stopping time and distance. Moreover, the plasma plume expands at the same initial rate at various oxygen pressures in the early time-delays. The classical drag and point-blast-wave models were used to explain the plasma plume expansion. The classical drag model fitted well at later stage, whereas the point-blast-wave model fitted well at intermediate stage of the ICCD plume images. The ideal shock condition was determined

at high oxygen pressure (0.1 and 0.2 mbar). The classical drag fit was used to determine the plume stopping distance, initial velocity, and slowing coefficient. The plume stopping distances were found to be ranging from 3.6 to 4.8 cm. The initial velocities were found to be ranging from $10.5x10^6$ to $8.4x10^6$ cm/s. The slowing coefficients were found to be ranging from 2.93 to 1.76 μs^{-1}.

The investigation of the optical emission of ablation plasma plume of VO_2 and V targets were studied in Chapter 5. This was carried out at vacuum and at a range of gas pressure (0.01 and 0.2 mbar), using spectrometer, digital oscilloscope, photomultiplier and ICCD camera. These were the mainly three atomic species (V I, V II and VO) were investigated. In case of VO_2 target, a linear increase was observed on the emission intensity close to the target surface until the emission intensity reaches the maximum for all the species. While, in case of V target, a maximum intensity was observed close to the target for all the species. The classical drag and point-blast-wave models were used to describe the plasma plume species expansion for both targets. The classical drag model fitted well at later stage and point-blast-wave fitted well at intermediate stage of the species expansion for both targets. The ideal shock condition was determined at high oxygen pressure (0.1 and 0.2 mbar) for all the species and both targets. The plume stopping distance, initial velocity, slowing coefficient were determined and for all the species and both targets. The plume stopping distance of VO_2 target species were found to be ranging from 0.26 to 0.5 cm. While the plume stopping distance of V target species were found to be ranging from 0.24 to 0.21 cm. The initial velocity of VO_2 target species were found to be ranging from $3.14x10^6$ to $0.63x10^6$ cm/s. While the initial velocity of V target species were found to be ranging from $0.52x10^6$ to $0.39x10^6$ cm/s. The slowing

coefficient of VO_2 target species were found to be ranging from 2.48 to 4.81 μs^{-1}. While the slowing coefficient of V target species were found to be ranging from 2.18 to 1.84 μs^{-1}.

The investigation of the relationship between the plasma plume dynamics and deposited V_xO_y compound thin films that were studied in Chapter 6. The V_xO_y thin films were deposited using the same conditions/parameters of the oxygen pressure and fluencies used for the plasma plume and species study. Thin films deposited with these plasma and plasma species conditions/parameters revealed the presence of V_xO_y nano-rods, nano-plates, and nano-fibers. The V_2O_3 phase was produced at low oxygen pressures, while VO_2 (M1) and VO_2 (B) nano-rods phases were deposited at 0.05 mbar oxygen pressure. The plume expansion and V_xO_y thin films' analysis show that oxides are mainly formed during the interaction of the plume with the background gas. In particular, high oxides thin films are efficiently produced when a shock-wave like propagation stage is achieved. A transition temperature of around 61 °C was measured for sample deposited at an oxygen pressure of 0.05 mbar oxygen pressure and target-substrate distance of 50 mm. This chapter showed that VO_2 (M1) film growth only under particular conditions and we are able to precisely control them as revealed by comprehensive structural and optical characterisation of the film grown, and through study of plume dynamics which behave as in other studies of other materials.

Chapter 7 demonstrated that it is possible to improve the VO_2 composition by investigating the link between the V-O plume and the VO_2 stoichiometry in a PLD

process without the need of post-deposition annealing. A pure monoclinic rutile-type VO_2 (M1) phase was successfully deposited at 0.05 mbar of 30 mm and 0.01 mbar of 38 mm without post-deposition annealing on Corning glass. These VO_2 (M1) films demonstrate a reversible MIT temperature at ~52 °C and ~57.3 °C, without any doping. Whereas the VO_2 (M1) deposited at 0.01 mbar of 36 mm demonstrates a reversible MIT temperature at ~43 °C without any doping. Our results indicate that the VO_2 will normally be deposited when the plume start slowing down (slow shock) and at below certain oxygen partial pressures and there are 0.01 to 0.05 mbar. We found that by increasing the target-substrate distance from 36 to 38 mm, the grain size of the VO_2 (M1) nano-particles can be increased. Furthermore, the increases of the hysteresis width and transition temperature as function of the grain size were also observed. This is in agreement with several results reported in the literature. We have shown that by investigating the plasma plume propagation of the various species (V I, V II and VO) presents good control of the stoichiometry and grain size of the deposited nano-particle thin films is possible. There is a good agreement between the deposited V_xO_y phases and structure with the plasma plume propagation.

Chapter 8 showed that it is possible to synthesized and improve the β-V_2O_5 composition by using the link between the V-O plume and the V_2O_5 stoichiometry in PLD without the need of post-deposition annealing. A β-V_2O_5 phase was successfully deposited at 0.2 mbar oxygen pressure without post-annealing on Corning glass. This results indicate that the β-V_2O_5 will normally be deposited at shock-wave, when the plume starts slowing down, at below certain oxygen partial pressures and there are 0.1 to 0.2 mbar. We found that by increasing the target-substrate distance from 23 to 37 mm, the nano-

rods dimension can be reduced. Furthermore, the increase of the target-substrate distance to 37 mm resulted to the β-V_2O_5 phase optimized.

Chapter 9 reported on the synthesis of a-axis oriented and nano-particles VO_2 (M1) using PLD on Corning glass without post-deposition annealing and doping. A pure monoclinic rutile-type VO_2 (M1) phase was successfully deposited at 0.05 mbar of 49 mm using V target at laser wavelengths of 266, 355 and 1064 nm without post-deposition annealing on Corning glass. Additionally, a highly a-axis oriented VO_2 thin film was obtained at 532 nm laser wavelength without post-deposition annealing on Corning glass. This film demonstrates a reversible MIT at ~62.2 °C with the smallest hysteresis width of ~9.2 °C and also corresponding to the smallest grain size of ~84.67 nm. These results are in agreement with the characteristic of VO_2 thin films and are as good as or better than VO_2 thin films made by other methods. We have shown that by make used of 532 nm laser wavelength in PLD, a highly a-axis oriented VO_2 thin film may grow on Corning glass.

This PhD study provided an improved knowledge of the plume characteristics that may open up the route to search for the more suitable experimental conditions for the growth of any complex oxide material, depending on its specific aspects.

10.2 Future Work

There are several applications for VO_2 as mentioned earlier in Chapter 2. We are interest in using VO_2 (M1) as thermochromics smart windows, because VO_2 (M1) can

respond to environmental temperatures, making reversible structural changes from an infrared-transparent semiconducting state to an infrared-translucent metallic state and partially blocking light while remaining transparent [10.1]. In order to successfully use VO_2 (M1) as a smart window, one must develop a transition temperature of VO_2 (M1) close to room temperature, the VO_2 film need be as transparency as possible and typical maximum visible transmittance values of ~ 60% [10.2].

We demonstrated in Chapter 7 that is possible to improve the VO_2 stoichiometric and to reduce the transition temperature to close to room temperature (~43 °C) with a narrow hysteresis width without doping and post-deposition annealing. This demonstration is important for the future work for increasing the maximum visible transmittance and film transparency. Plasma plume expansion and plume species knowledge will be useful in this future work.

We obtained a highly a-axis oriented polycrystalline VO_2 (M1) in Chapter 9 with narrow hysteresis width of ~9.2 °C on Corning glass using 532 nm laser wavelength without doping and post-deposition annealing. This is a new technique to obtain a highly oriented VO_2 (M1). Generally single crystals substrate is effective to obtain highly oriented VO_2 thin films with a large resistivity during phase transition and a narrow hysteresis width because MIT domain wall propagation of highly oriented VO_2 is faster. There are several investigations need to be done in the future including: optimization of the highly a-axis oriented VO_2, reducing the hysteresis width to ~1 °C, reducing the transition temperature to close room temperature and synthesis of highly a-axis

oriented single crystal VO_2 (M1). Additionally, to investigate the 532 nm laser wavelength interaction with VO_2 target, making use of the plasma plume knowledge in Chapters 4 and 5. In Chapter 8, we demonstrated that is possible to obtain the β-V_2O_5 stoichiometric on Corning glass without post-deposition annealing using plasma dynamics, paving the way for β-V_2O_5 gas sensing investigation.

References

10.1 Y. Gao, H. Lou, Z. Zhang, L. Kang, Z. Chen, J. Du, M. Kanehira, C. Cao, "Nanoceramic VO_2 thermochromic smart glass: A review on progress in solution processing", Nano Energy **1**, 221 (**2012**).

10.2 M.A. Sobhan, R.T. Kivaisi, B. Stjerna, C.G. Granqvist, "Thermochromism of sputter deposited $W_xV_{1-x}O_2$ films", Solar Energy Mater. and Solar Cells **44**, 451 (**1996**).